STRUCTURAL AND ELECTRONIC PROPERTIES OF PENTACENE AT ORGANIC-INORGANIC INTERFACES

by

Soonjoo Seo

A dissertation submitted in partial fulfillment of
the requirements for the degree of

Doctor of Philosophy
(Materials Science)

at the

UNIVERSITY OF WISCONSIN-MADISON

2010

Abstract

Organic/inorganic interfaces play a crucial role in organic electronic devices such as organic field effect transistors (OFETs), organic light emitting diodes (OLEDs) and organic photovoltaics (OPVs). The properties of organic thin-film transistors depend on the transport of charges induced at the semiconductor/gate insulator interface. Structural defects near this interface influence the charge carrier mobility of organic thin film transistors. Our understanding of these effects can be improved by developing a molecular-scale structural description of the relevant organic/inorganic interfaces.

We used scanning tunneling microscopy (STM) to probe the molecular-scale structure of vacancies, grain boundaries and stacking faults in pentacene thin films on styrene-passivated Si (001). We provide direct evidence for large structural distortions of crystalline lattices around vacancies in pentacene thin films. The position of molecules relative to each type of vacancy can be identified in STM images in which the crystallographic orientations of the (001) and ($00\bar{1}$) surfaces of pentacene are distinguishable. One nearest neighbor of each vacancy is displaced far more than other molecules.

There are three distinctive types of extended defects found in pentacene thin films on styrene/Si (001). High-angle tilt grain boundaries are formed at the junction between two pentacene islands and tilt grain boundaries are formed between molecular layers. The tilt grain boundaries consist of segments faceted along the low-energy planar orientation. One molecular plane is missing at a stacking fault. Two rows of molecules near a stacking fault have an

apparent height of 60 pm higher than the neighboring molecules. Stacking faults are associated with trap states in pentacene thin films.

Scanning tunneling spectroscopy (STS) measurements show that the molecular layers we used for structural studies also modify the electronic properties of pentacene thin films. Negative differential resistance was observed in pentacene thin films on Si (001) modified with nitrobenzene and styrene.

Acknowledgements

This thesis would not have been completed without help of many individuals. I am so grateful for their help, advice, and friendship of people who have shared with me over the past years here at University of Wisconsin.

First of all, I would like to thank my adviser Professor Paul Evans, for his guidance of my adventure into the research, and for the enlightening discussions. I have learned to recognize scientific questions, think through the issues, and create solutions. With his help I have achieved an understanding that I have never expected.

Thanks to all of the Evans group members who have been my teachers, collaborators, and friends throughout the years. Rebecca Sichel, a special friend of mine, gives me an honest opinion or answer, and encourages me with scientific and social conversations. Dr. Jiyoung Cho, a pleasant and optimistic person to talk with, helped me see the other side of issues and kept me going. Joesef Spalenka, Ryan Smith and Pice Chen are the group members who I have had the pleasure of working with. I would also thank Dr. Byoungnam Park and Joona Kang for being great friends to me. It has been a wonderful experience to share all the joy and fun together.

I owe a large thanks to Dr. Guowen Peng who is a talented person in simulations and calculations. He is unique in his comprehension and implementation of the theory that complements my experiments. I am thankful to Professor Manos Mavrikakis for his advice and valuable input into the research project. I also thank Rose Ruther for the fruitful collaborations.

It has been a pleasure to have Chris Kailhofer around. He has been a great friend and I appreciate his expertise in the arts of machining.

My life has been tremendously enriched by Diana Rhoads who taught me so much more about life beyond research. She provides me to-the-point advice and shares her experience, wisdom and philosophy.

I would have never accomplished all that I have in life without the support of my family, Mom, Dad, Soonae, and everyone else who took the time to send me an email, make a phone call, or to drop in and check on me. Nothing cheers me up as much as a quick phone call to talk to one of you or to hear the chaos of life.

Most importantly, I would like to express my deepest gratitude to Ikjoon Choi for being always there for me and empowering me.

Our work is supported by the Petroleum Research Fund of the American Chemical Society and by the National Science Foundation through the University of Wisconsin Materials Research Science and Engineering Center.

Table of Contents

Chapter 1

Introduction

1.1 Organic/inorganic interface

Organic/inorganic interfaces are important in determining the properties of organic electronic devices such as organic field-effect transistors (OFETs), organic light emitting diodes (OLEDs) and organic solar cells [1-3]. Improving the performance of these devices has the potential to result in more efficient sources of lighting, printable electronics, and highly scalable solar energy harvesting. This thesis discusses the fundamental materials science questions of the structure and electronic properties of organic/inorganic interfaces, which are ubiquitous in these devices.

The properties of organic thin-film transistors depend on the transport of charges induced at the gate insulator/semiconductor interface. Charge transport is influenced by the crystal structure and morphology of the first few molecular layers next to the gate insulator [4, 5]. Park *et al.* found that the growth and geometric arrangements of single molecular layer islands affect the electrical properties of pentacene thin films [6]. Structural defects including grain boundaries and statistical quantities describing the overall structure, such as the grain size, are already known to influence the charge carrier mobility of organic thin film transistors [7]. Our understanding of these effects can be improved by developing a molecular-scale structural description of the relevant organic/inorganic interfaces.

Defects in organic crystals, including grain boundaries, have been widely studied because of their relevance to charge transport of organic electronic devices [8-12]. Grain boundaries at the junctions of islands disrupt charge transport at the highest misorientation angle between grains [12]. High angle grain boundaries also cause a decrease in the magnitude of photocurrent in bicrystals [13]. At a smaller scale, electronic states calculations and spectroscopy experiments show that molecular vacancies trap charge carriers [14-16].

Probing the molecular-scale structure of defects is important in making the link between charge transport models on a microscopic scale and the real-space structure of defects. Testing charge transport models requires molecular resolution imaging because the structures described in the models are based on the arrangement of molecules near the defects [17, 18].

The first part of this thesis describes the real-space imaging of defects in pentacene thin films grown on Si (001) modified with organic molecules. Our experiments use scanning tunneling microscopy (STM), a technique with spatial resolution allowing individual molecules to be imaged. In the second part of the thesis, we apply the techniques associated with surface modification to develop electronic interfaces using an organic layer and study the transport properties of these interfaces. These experiments use the capabilities of the STM to probe the electronic properties of interfaces using scanning tunneling spectroscopy (STS). Our experiments are conducted in ultrahigh vacuum (UHV) in order to minimize surface contamination.

1.2 Pentacene

We created interfaces using pentacene ($C_{22}H_{14}$), a stable small-molecule with a long, planar molecular shape that facilitates crystalline packing (Fig. 1(a)). Pentacene has been widely used to create organic electronic devices including field-effect transistors (FETs) [19, 20]. The pentacene molecule consists of five benzene rings. In bulk, pentacene forms a triclinic crystal with lattice constants a=7.90 Å, b=6.06 Å and c=16.01 Å [21, 22]. Pentacene is easy to work with in ultrahigh vacuum (UHV) because *in situ* thin film deposition and the surface characterization can be done under UHV conditions.

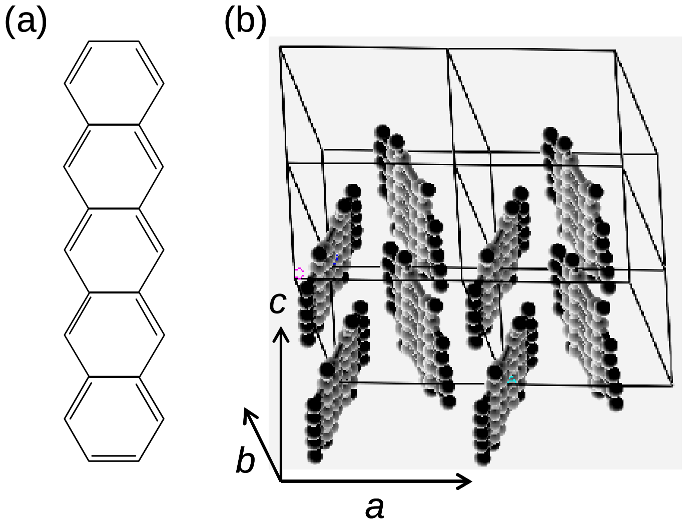

Figure 1. (a) Molecular structure and (b) triclinic bulk structure of pentacene.

The orientation of pentacene molecules at pentacene/inorganic interfaces depends on the molecular interactions between pentacene and the substrate. On metals and reactive semiconductor surfaces pentacene forms a structure in which molecules lie flat on the surface, as illustrated in Fig. 2(a) [10, 23, 24]. The second and the subsequent molecular layers do not have the same local environment and forms a more bulk-like structure.

1.3 Surface modification

We chose to use Si substrates because *in situ* preparation of Si surfaces is straightforward and because Si exhibits a smooth and atomically flat surface over lateral scales of tens to hundreds of nanometers. Clean Si surfaces are highly reactive and inappropriate for organic device applications. By modifying the substrate to reduce the interaction with organic molecules, organic crystals in thin films can be formed with many similarities to pentacene films on SiO_2 [25, 26]. The step-by-step procedure for the modification of Si (001) using styrene and deposition of pentacene on the modified surface is schematically shown in Fig. 3. The clean Si (001) surfaces were imaged using STM before the organic molecules were deposited.

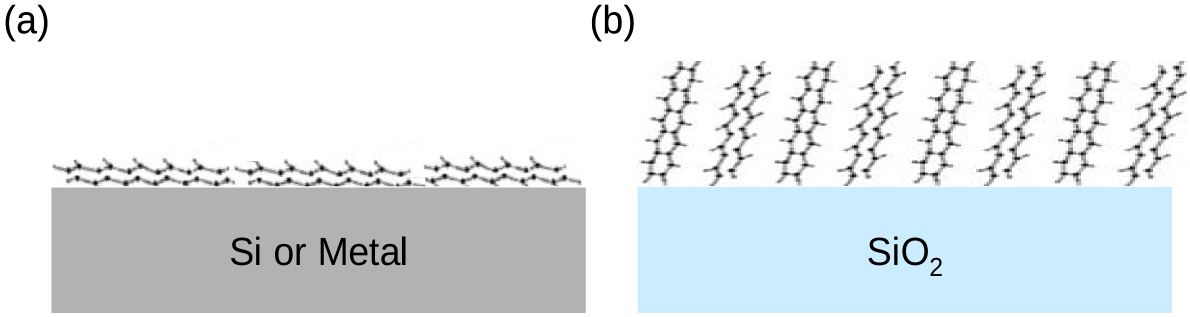

Figure 2. (a) Pentacene molecules on clean Si or on metal lie flat in the first molecular layer. (b) Pentacene molecules stand up on SiO_2.

As shown in the STM image in Fig. 3(b), we found that styrene molecules do not form ordered rows on Si (001). Somewhat surprisingly, however, modifying the Si (001) surface with styrene provides a smooth and conductive substrate for STM studies. The large faceted islands of pentacene in Fig. 3(c) indicate that pentacene grown on Si (001) modified with styrene forms a crystalline structure with large grains. Pentacene on styrene/Si (001) can be used to understand the structure of defects at pentacene/SiO_2 interfaces. The molecular-scale structures of defects such as vacancies, grain boundaries and stacking faults in pentacene thin films on styrene/Si (001) are described in Chapter 4 and Chapter 5.

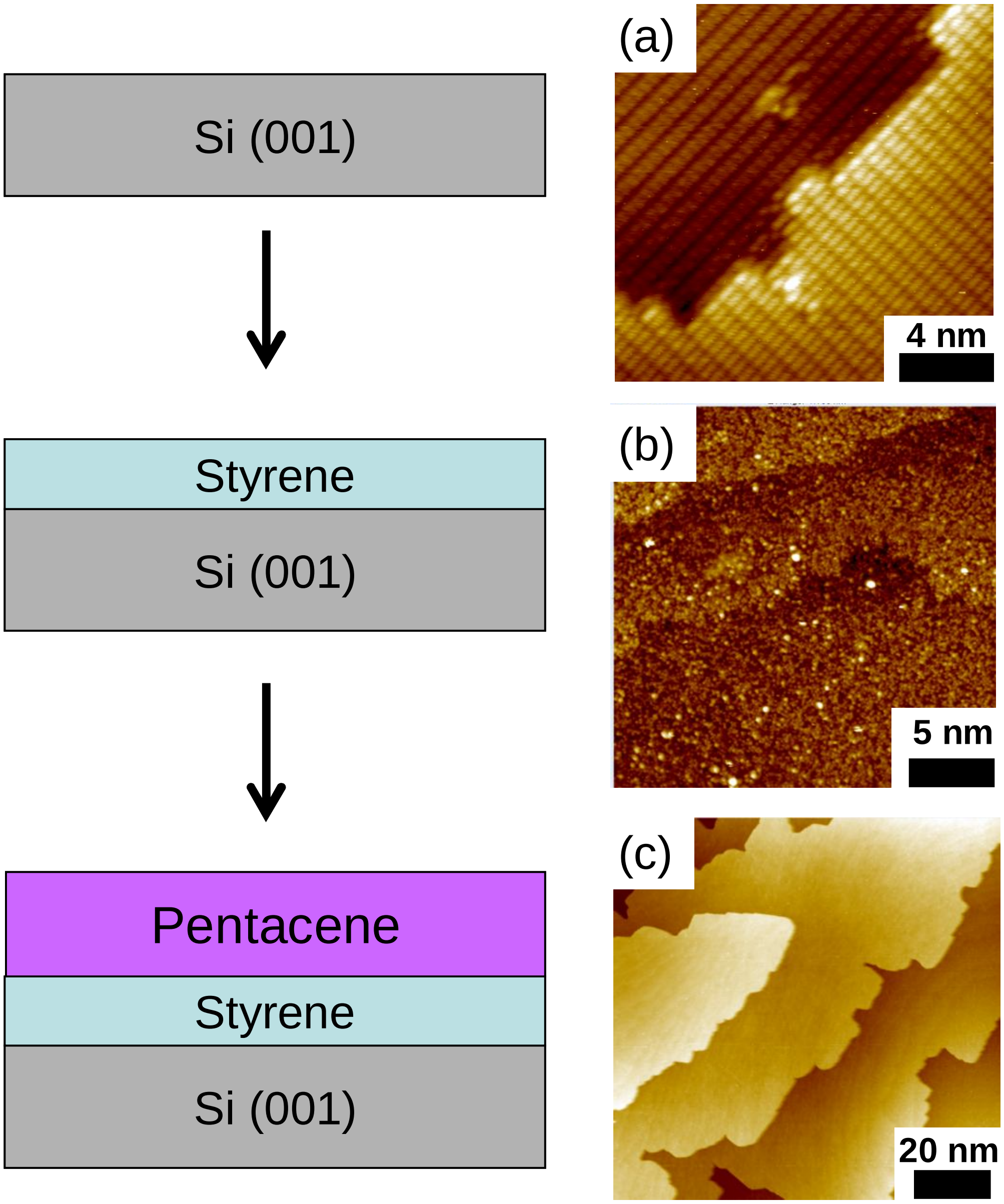

Figure 3. Schematic and the corresponding STM images of the procedure for modifying Si (001) with styrene and depositing pentacene on the modified Si (001) surface. (a) Bare Si (001). (b) Styrene on Si (001). (c) Pentacene on styrene/Si (001).

1.4 The effects of molecular interlayers on the electronic properties of pentacene

We found in STS experiments that the molecular layers we used for structural studies also modified the electronic properties of pentacene thin films. Tunneling spectra were measured on pentacene grown on Si (001) modified with nitrobenzene and styrene. We observed negative differential resistance (NDR) in both structures. The tunneling spectra results are described in Chapter 6.

1.5 References

[1] H. E. Katz and Z. Bao, J. Phys. Chem. **104**, 671 (2000).

[2] A. P. Kulkarni, C. J. Tonzola, A. Babel, and S. A. Jenekhe, Chem. Mater. **16**, 4556 (2004).

[3] C. Walduf, C. J. Brabec, P. Schilinsky, J. Hauch, and C. J. Brabec, Thin Solid Films **451**, 503 (2004).

[4] E. L. Granstrom and C. D. Frisbie, J. Phys. Chem. B **103**, 8842 (1999).

[5] G. Horowitz, Adv. Mater. **10**, 365 (1998).

[6] B.-N. Park, S. Seo, and P. G. Evans, J. Phys. D: Appl. Phys. **40**, 3506 (2007).

[7] A. Di Carlo, F. Piacenza, A. Bolognesi, B. Stadlober, and H. Maresch, Appl. Phys. Lett. **86**, 263501 (2005).

[8] A. Bolognesi, M. Berliocchi, M. Manenti, A. Di Carlo, P. Lugli, K. Lmimouni, and C. Dufour, IEEE Trans. Electron Devices **51**, 1997 (2004).

[9] Y. Y. Lin, D. J. Gundlach, S. F. Nelson, and T. N. Jackson, IEEE Trans. Electron Devices **44**, 1325 (1997).

[10] C. D. Dimitrakopoulos, I. Kymissis, S. Purushothaman, D. A. Neumayer, P. R. Duncombe, and R. B. Laibowitz, Adv. Mater. **11**, 1372 (1999).

[11] K. Puntambekar, J. P. Dong, G. Haugstad, and C. D. Frisbie, Adv. Func. Mater. **16**, 879 (2006).

[12] A. B. Chwang and C. D. Frisbie, J. Appl. Phys. **90**, 1342 (2001).

[13] J. Liao and D. C. Martin, Macromolecules **29**, 568 (1996).

[14] D. Tsiaousis and R. W. Munn, J. Chem. Phys. **117**, 1833 (2002).

[15] E. A. Silinsh, I. J. Muzikante, A. J. Rampans, and L. F. Taure, Chem. Phys. Lett. **105**, 617 (1984).

[16] I. Eisenstein and R. W. Munn, Chem. Phys. **77**, 47 (1983).

[17] R. A. Street, J. E. Northrup, and A. Salleo, Phys. Rev. B **71**, 165202 (2005).

[18] S. Verlaak and P. Heremans, Phys. Rev. B **75**, 115127 (2007).

[19] B. Stadlober, M. Zirkl, M. Beutl, G. Leising, S. Bauer-Gogonea, and S. Bauer, Appl. Phys. Lett. **86**, 242902 (2005).

[20] F. De Angelis, S. Cipolloni, L. Mariucci, and G. Fortunato, Appl. Phys. Lett. **86**, 203505 (2005).

[21] R. B. Campbell and J. Monteath Robertson, Acta Cryst. **15**, 289 (1962).

[22] J. E. Northrup, M. L. Tiago, and S. G. Louie, Phys. Rev. B **66**, 121404 (R) (2002).

[23] M. Eremchenko, R. Temirov, D. Bauer, J. A. Schaefer, and F. S. Tautz, Phys. Rev. B **72**, 115430 (2005).

[24] L. Gavioli, M. Fanetti, M. Sancrotti, and M. G. Betti, Phys. Rev. B **72**, 035458 (2005).

[25] R. Ruiz, D. Choudhary, B. Nickel, T. Toccoli, K.-C. Chang, A. C. Mayer, P. Clancy, J. M. Blakely, R. L. Headrick, S. Iannotta, and G. G. Malliaras, Chem. Mater. **16**, 4497 (2004).

[26] S. Fritz, S. M. Martin, C. D. Frisbie, M. D. Ward, and M. F. Toney, J. Am. Chem. Soc. **126**, 4084 (2004).

Chapter 2

Ultrahigh Vacuum Scanning Tunneling Microscopy

2.1 Introduction

Structural and electronic characterization was performed using STM and atomic force microscopy (AFM) in an ultrahigh vacuum (UHV) chamber. These techniques allowed us to use the same vacuum chamber for scanning probe microscopy and *in situ* sample preparation.

The advantage of performing surface studies in UHV is that the sample and the scanning probe tip remain free of contamination longer than they would under ambient conditions. In addition, alternate electrical conduction paths through the electrical breakdown of water are eliminated in UHV, which ensures that the current is flowing from the tip due to tunneling.

2.2 The UHV chamber

The UHV system consists of a variable temperature STM and AFM built by Omicron Nanotechnology integrated into a separate UHV vacuum chamber consisting of facilities for pumping and sample preparation, as shown in Fig. 1. The vacuum is maintained by an ion pump and a titanium sublimation pump (TSP). Separate components add sample transfer and deposition capabilities. A small separate preparation chamber and load lock chamber are also labeled in Fig. 1. The UHV system is equipped with a motorized translational arm, two linear manipulators and an XYZ manipulator that can move the sample in three different directions. A sample heating stage is attached to the XYZ manipulator.

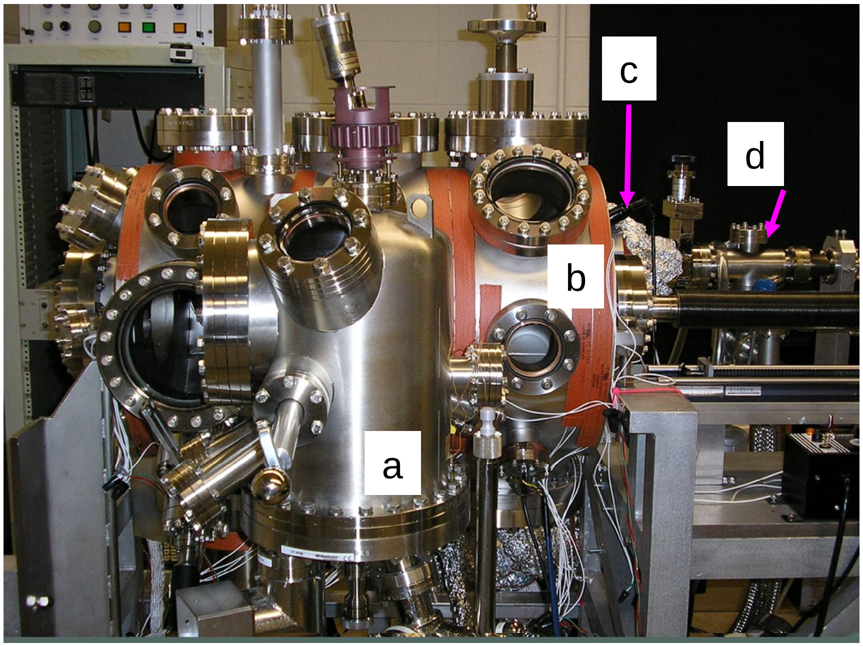

Figure 1. (a) UHV STM and AFM, (b) deposition chamber, (c) preparation chamber, and (d) load lock.

The STM chamber in Fig. 2 is attached to the main chamber. The wobble stick (Fig. 2(a)) can reach the manipulator to transfer a sample or a tip. A carousel installed between the deposition chamber and the STM chamber contains 12 slots to store samples and tips.

The STM tip scans relative to the sample. Figure 2(b) shows the STM head with the sample facing down and the tip pointing up. The tip can be mounted on special holders designed to be picked up by the wobble stick and the sample transfer system. By replacing the tungsten STM tip with a cantilever, the microscope can be easily switched between STM and AFM modes.

The deposition system has the capability to modify the sample surface by evaporating organic molecules onto the substrate. The evaporator has a heater attached to the bottom of the crucible to heat the organic source. The source temperature was measured using a type K thermocouple attached to the stainless steel crucible.

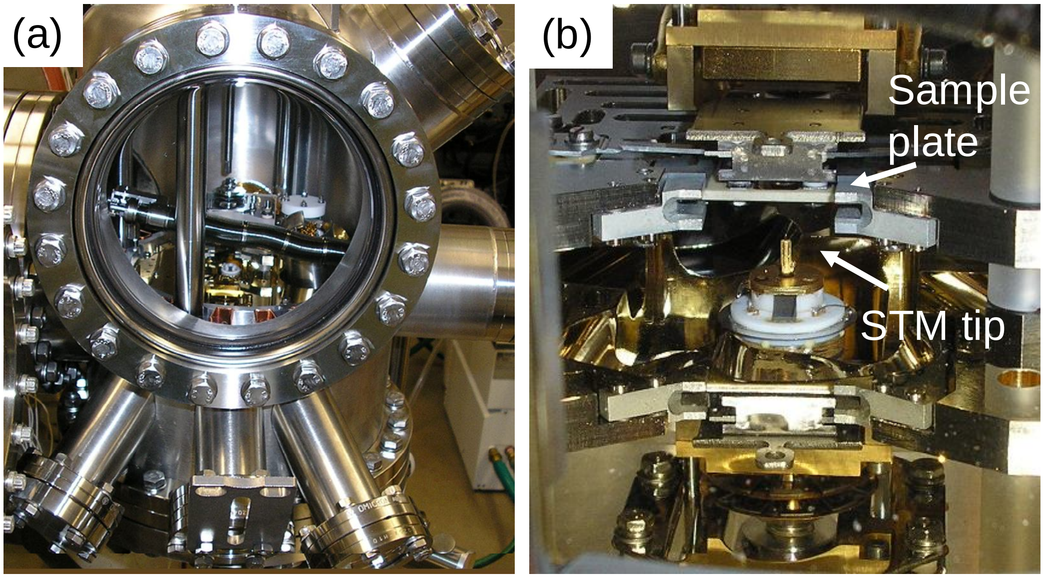

Figure 2. (a) Front view of the STM. (b) STM head in the microscope.

A sample is introduced into the preparation chamber through a load lock, Fig. 1(d). The load lock allows us to switch new samples and tips without venting the UHV chamber. This saves time and protects the chamber from contamination. When a new sample or a tip is inserted, the load lock is pumped by the sorption pump down to 10^{-3} Torr and then switched to the turbo pump until the sample is transferred to the preparation chamber.

The preparation chamber is used as a transition path for the sample to be moved from the load lock at 10^{-6} Torr to the UHV chamber at 10^{-10} Torr. The preparation chamber can be independently pumped by the turbo pump. The pressure of the preparation chamber goes down to 10^{-8} Torr without baking. After a sample is introduced into the UHV chamber, the gate valve is closed right away. The pressure in the UHV chamber drops to 2×10^{-10} Torr within 10 minutes after the valve is closed. The sample is then moved to the heating stage for degassing. High-temperature surface preparation is done at the same heating stage before it is transferred to the microscope for characterization.

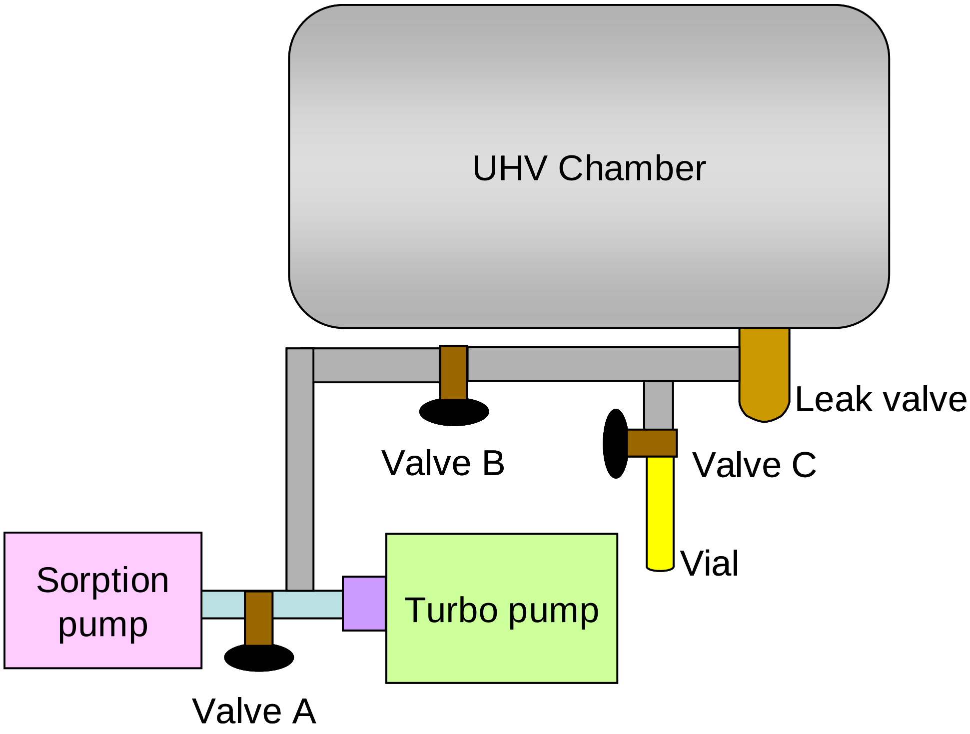

Figure 3. Schematic of the setup for leaking molecules into the chamber.

Small organic molecules can be leaked into the deposition chamber using a leak valve. The gas introduction system divides the volume behind the leak valve into several independent volumes that could be pumped independently. The volume between the vial and the leak valve was pumped with a sorption pump and the turbo pump for 2 to 3 hours before leaking molecules into the main chamber. This setup is depicted in Fig. 3.

The microscope had the capability of cooling samples using a continuous-flow liquid He cryostat. The molecules can be resolved by minimizing the molecular motion at low temperatures because thermal effects such as surface diffusion are suppressed. Figure 4 shows the setup for experiments at low temperatures using the cryostat. The port for flow of liquid helium is part of the bolt-on microscope chamber. Thermal coupling between the cryostat and the sample is accomplished by a copper braid and clamping mechanism. Cooling can be achieved using liquid nitrogen or liquid helium. Liquid helium allows sample temperatures down to 25 K.

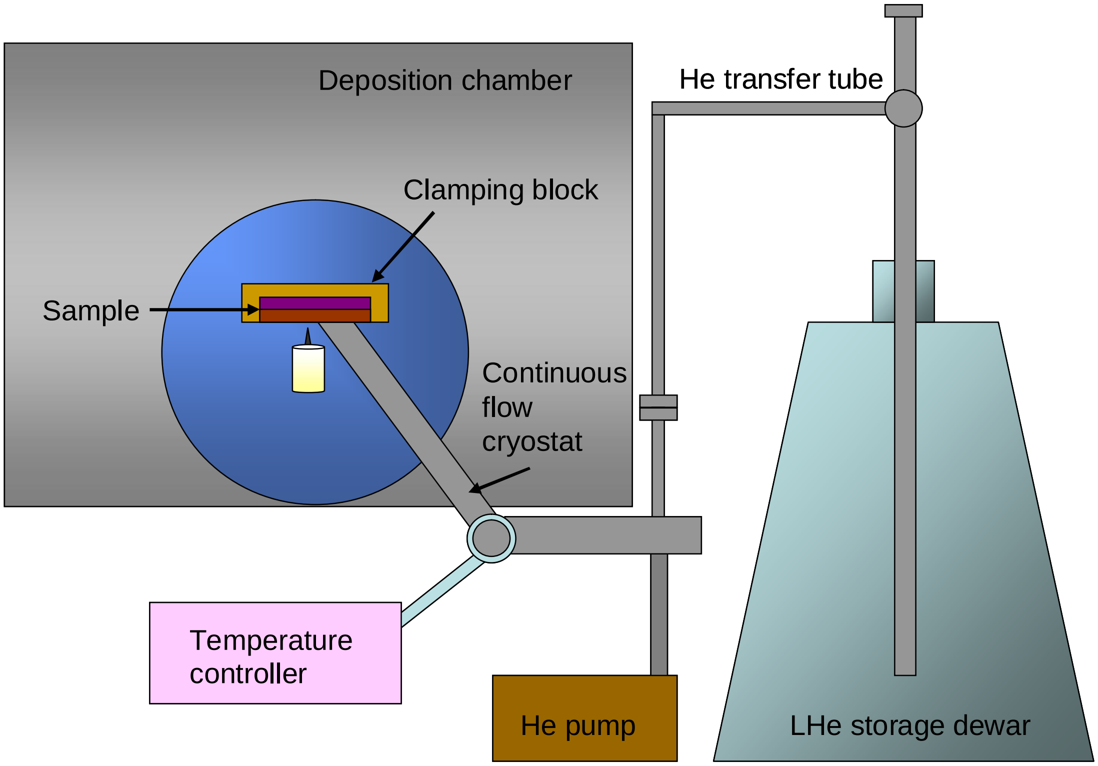

Figure 4. Schematic diagram for LHe cooling.

2.3 Scanning tunneling microscopy

STM is a microscopy technique based on the tunneling of electrons between the tip and the sample. The magnitude of the tunneling current depends exponentially on the separation between the tip and the sample. A model based on tunneling between two metal electrodes helps to quantify what is observed in STM experiments. The separation between the tip and the sample, z, is expressed by a barrier width in the model.

The solution of Schrödinger equation within a square potential barrier has the form [1]:

$$\Psi \propto e^{\pm \kappa z}, \tag{1}$$

where the decay constant κ is defined as

$$\kappa = \frac{2\pi}{h}[2m\phi]^{1/2} \text{ and} \tag{2}$$

$$\phi = \frac{(\phi_s - eV_b + \phi_t)}{2}. \tag{3}$$

ϕ_s and ϕ_t are the potential barriers whose heights are equal to the work functions of the sample and the tip, respectively. h is the Planck's constant, m is the electron mass, and V_b is the bias voltage applied between the tip and the sample. Based on Wentzel-Kramers-Brillouin (WKB) approximation, the tunneling current depends exponentially on κ and the position z [2, 3]:

$$I \propto e^{-2\kappa z}. \tag{4}$$

The tunneling current in STM is given by

$$I = \int_{-\infty}^{\infty} [f(E - eV) - f(E)]\rho_s(z,E)\rho_t(z,E - eV)T(z,E,eV)dE, \tag{5}$$

where E is the energy measured with respect to Fermi energy, E_F of the sample and $T(z, E, eV)$ is the transmission probability. $f(E-eV)$ and $f(E)$ are Fermi-Dirac distributions for the tip and the sample, respectively [4, 5]. The tunneling current may be rewritten as

$$I = \int_0^{eV} \rho_s(z,E)\rho_t(z,E-eV)T(z,E,eV)dE\,, \tag{6}$$

where ρ_s and ρ_t are the local density of states of the sample and the tip.

Energy-dependent information of the electronic properties of surfaces may be obtained from measuring differential conductance. Assuming that the density of states of the tip is constant, the tunneling current suggested by Tersoff and Hamann can be generalized as [6, 7]

$$I \propto \int_0^{eV} \rho_s(E)T(E)dE\,. \tag{7}$$

The differential conductance is then expressed by

$$dI/dV \approx \rho_s(eV)T(eV)\,. \tag{8}$$

Equation (8) shows that dI/dV reflects the local density of states (LDOS) of the sample which contributes to tunneling. The exponential dependences of voltage and tip-sample separation that result from the transmission probability can be removed by normalizing differential conductance by I/V. The normalized differential conductance is

$$\frac{dI/dV}{I/V} = \frac{\rho_s(eV)T(eV)}{(1/eV)\int_0^{eV} \rho_s(E)T(E)}\,. \tag{9}$$

By cancelling the transmission factors, we obtain

$$\frac{dI/dV}{I/V} = \frac{\rho_s(eV)}{(1/eV)\int_0^{eV} \rho_s(E)}\,. \tag{10}$$

Equation (10) indicates that the normalized differential conductance is proportional to the normalized local surface density of states of the sample.

The STM tip is brought into close proximity to the surface of the sample in the process acquiring images and measurements of current as a function of voltage [8]. STM images are acquired by rastering the tip across the sample surface while varying the height of the tip to maintain a constant current. Under the assumption that the surface density of states and the conductivity are uniform, a map of the height of the surface is obtained.

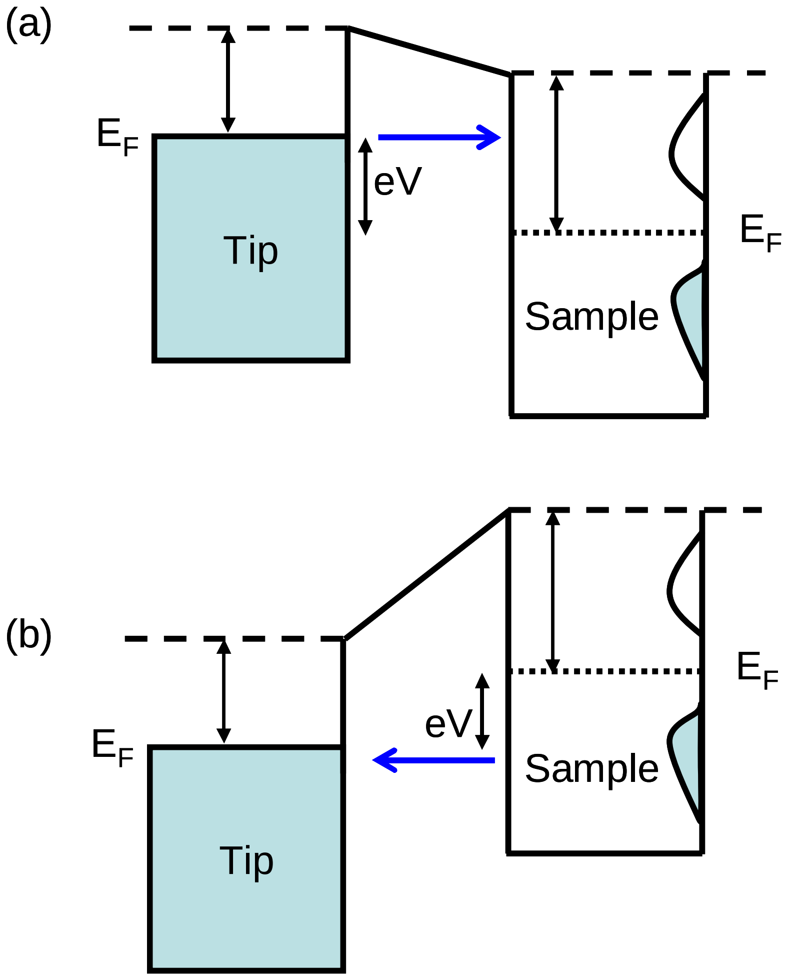

Figure 5. Energy level diagram of tip-vacuum- sample tunnel junction (a) with a positive sample bias relative to the tip and (b) with a negative sample bias relative to the tip.

Figure 5 shows the energy level diagram for a tip-vacuum-sample tunnel junction. When there is no bias voltage applied between the tip and the sample, the Fermi level is uniform. When a positive voltage is applied to the sample (Fig. 5(a)), electrons tunnel from the tip to the empty states of the sample. When a negative voltage is applied to the sample (Fig. 5(b)), electrons tunnel from the filled states of the sample to the tip.

2.4 Scanning tunneling spectroscopy

Current as a function of voltage (*I-V*) spectra are obtained using scanning tunneling spectroscopy (STS). The STM tip is placed over a specific position on the sample. For STS measurements, the tip height feedback is temporarily disabled so that *I-V* spectra can be measured at a fixed tip-sample separation. Feedback is established again after the measurement. The voltage is ramped from a negative initial value to a positive value during the measurement. The total time required to acquire an *I-V* measurement ranged between 200 and 500 ms.

The differential conductance, *dI/dV*, was measured using a lock-in amplifier. A small voltage signal at a given frequency is added to the bias voltage. The voltage signal going to the lock-in amplifier is the tunneling current multiplied by the preamplifier gain, 10^9 V/A.

2.5 Sample preparation

2.5.1 Si (111) and Si (001)

Proper preparation of sample surfaces is crucial because surface conditions play an important role in STM and STS. The chemical preparation of silicon samples was slightly different for (111) and (001) surfaces. Si (111) samples (0.005 Ω cm resistivity, doped with arsenic) were degreased in trichloroethylene at 75 °C for 5 minutes and rinsed in room temperature acetone and methanol. The surfaces were cleaned in $H_2O:NH_4OH:H_2O_2$ (4:1:1) and in $HCl:NH_4OH$ (3:1) at 80 °C for 5 minutes to remove organic and metal contaminants, respectively. The samples were oxidized in a Shiraki solution [8] and etched in 25% HF [8]. The oxidizing and etching processes were done twice. After a third oxidation in $HCl:H_2O:H_2O_2$ (3:1:1) at 100 °C for 10 minutes, the sample was introduced into the UHV chamber and degassed at 600 °C overnight. Clean Si (111) surfaces exhibiting the (7×7) reconstruction were prepared by heating to 1250 °C for 5 s, quenching at 900 °C, and then cooling slowly at a rate of $1\ °C\ s^{-1}$.

STM images of the clean Si (111) surface before the growth of pentacene were similar to the images reported in the literature [9]. The STM image in Fig. 6 shows the (7×7) unit cell of Si (111) including faulted and unfaulted triangles. This is the typical topography observed in a filled-state image of the (7×7) reconstructed surface of Si (111). These reproducible surfaces were the starting point for our STM studies of pentacene thin films.

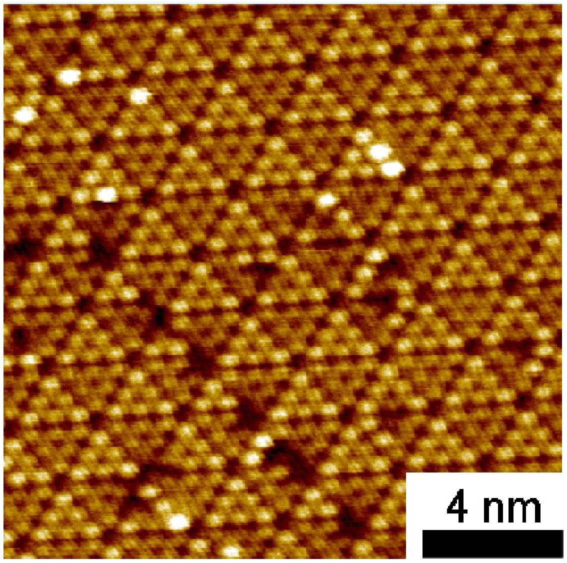

Figure 6. Filled-state image acquired with -1.7 V and 500 pA for *n*-type Si (111) prepared in UHV.

The Si (001) samples (0.07 – 0.1 Ω cm resistivity, doped with phosphorous) were cleaned using three cycles of the Interuniversity Microelectronics Center (IMEC) process [10]. In each cycle, samples were cleaned in a mixture of H_2SO_4 and H_2O_2 (H_2SO_4:H_2O_2 = 4:1) at 90 °C for 2 minutes and dipped in 1% HF solution for 2 minutes to remove the oxide. In the final step, the samples are taken out of a mixture of H_2SO_2 and H_2O_2 solution and have a thin layer of oxide. As with the Si (111) samples, the Si (001) samples were then loaded into the ultrahigh vacuum chamber and degassed overnight at 600 ºC. Surfaces exhibiting the (2×1) reconstruction were prepared by heating the sample to 1250 °C for 5 s, cooling rapidly to 1000 °C, and then cooling slowly at a rate of 1 °C s^{-1}.

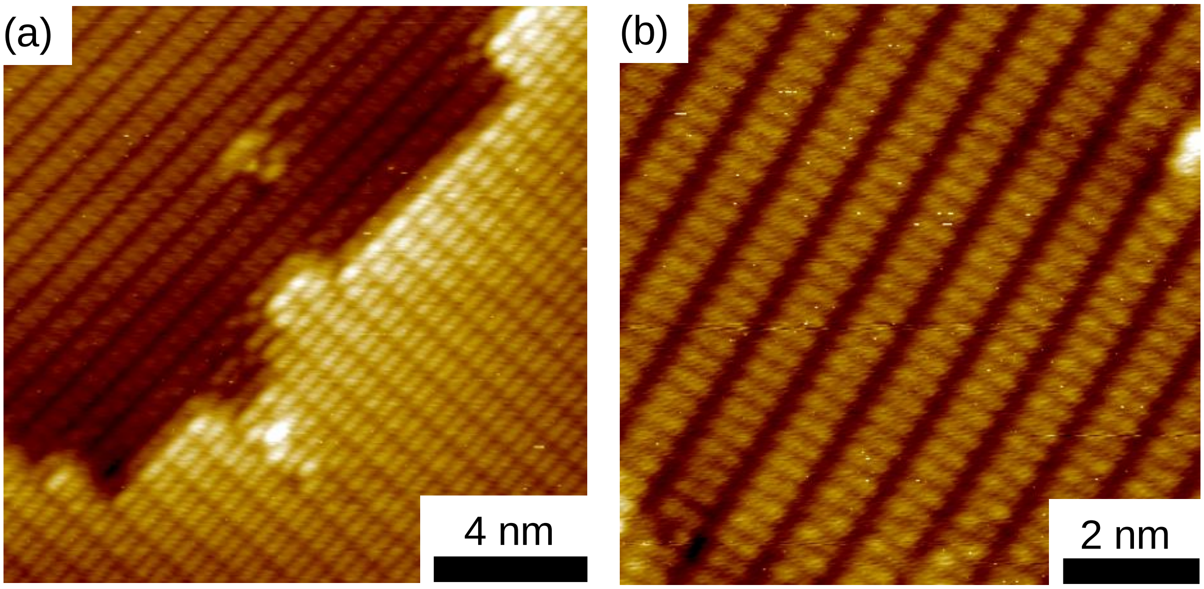

Figure 7. STM images of clean Si (001) showing (a) dimer rows rotated by 90° in each atomic layer and (b) a larger view of dimer rows in which two Si atoms are paired into each dimer.

Clean Si (001) surfaces were imaged using STM. On the Si (001) surface, each atom has two dangling bonds with a nearest neighbor separated by a_0 = 3.85 Å. The Si (001) surface is composed of orthogonal (1×2) and (2×1) terraces separated by monatomic steps. Two neighboring surface atoms will dimerize to form (2×1) reconstruction to lower the surface energy (Fig. 7(b)). (1×2) and (2×1) domains alternate in each atomic layer with dimer rows rotated by 90° as shown in Fig. 7(a). The dimer rows are separated by $2a_0$ = 7.7 Å, due to the (2×1) periodicity.

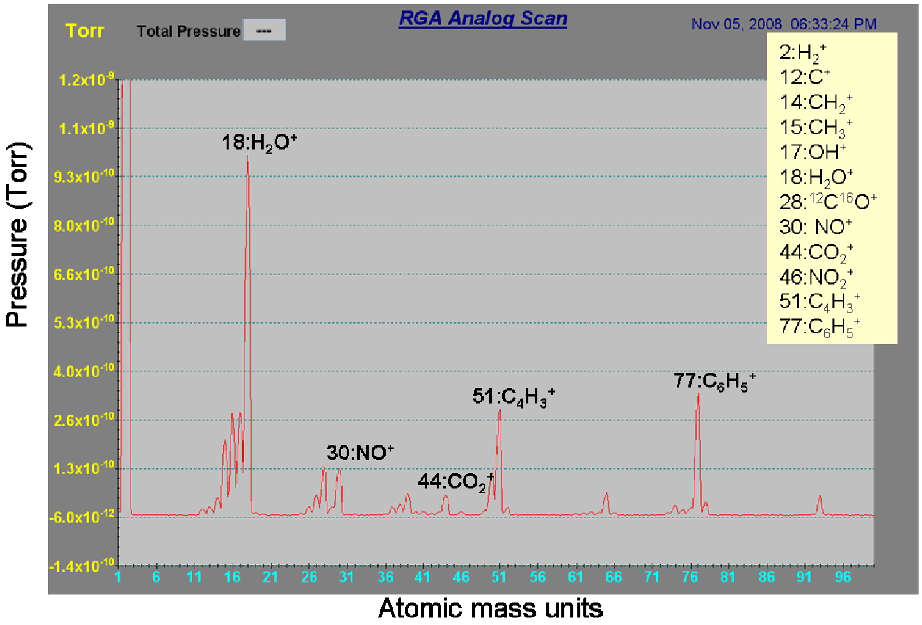

Figure 8. RGA spectrum acquired in the UHV chamber while nitrobenzene is leaking into the chamber at 1 × 10^{-8} Torr.

2.5.2 Deposition of small organic molecules

In order to minimize the introduction of contamination into the UHV chamber with the organic molecules, the organic source was purified by several freeze-pump-thaw cycles prior to dosing onto bare Si surfaces and leaked into the chamber. The typical dose for the organic molecules was 30 Langmuir, which corresponds to an exposure of 300 s at 1.0×10^{-7} Torr. High-purity cyclopentene (99%), styrene (99.9%) and nitrobenzene (99.7%) were purchased from Sigma Aldrich. Cyclopentene and styrene were often used as received without freeze-pump-thaw cycles because the fraction of foreign species in the liquid was low enough that experiments were not ruined by contamination.

Nitrobenzene was purified by six freeze-pump-thaw cycles first and then we used a residual gas analyzer (RGA) to examine how much water is leaked into the UHV chamber with nitrobenzene at 1×10^{-8} Torr. The RGA spectrum in Fig. 8 was collected in the presence of nitrobenzene molecules. The water peak at atomic mass of 18 reaches 1×10^{-9} Torr even after the purification procedure.

To remove the contamination evident in Fig. 8, we developed a further purification procedure for the nitrobenzene source. Nitrobenzene liquid was heated to 25 °C, 35 °C, 60 °C, and 90 °C for 10 minutes each. The gas valve isolating the vial from the turbo pump opened at each temperature to suck up any vapor other than nitrobenzene. Figure 9(a) was taken immediately after the vial was heated to 90 °C. Liquid condensed on the side wall of the vial during the heating process.

After this heating process, the nitrobenzene source was purified by a further set of three freeze-pump-thaw cycles. The vial containing nitrobenzene cooled to room temperature is shown in Fig. 9(b). The RGA spectrum in Fig. 10 was acquired in the UHV chamber while nitrobenzene is leaking into the chamber after the additional purification steps. Fig. 10 shows that the amount of water is remarkably decreased by purifying the nitrobenzene source. The results showed that the liquid condensed on the side wall of the vial is nitrobenzene.

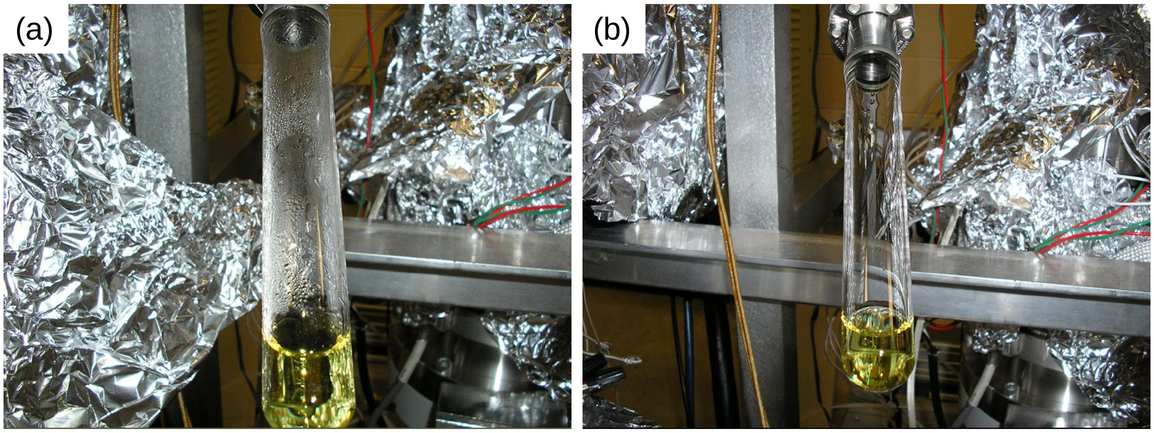

Figure 9. Pictures of a vial containing nitrobenzene (a) at 90 °C and (b) cooled to room temperature.

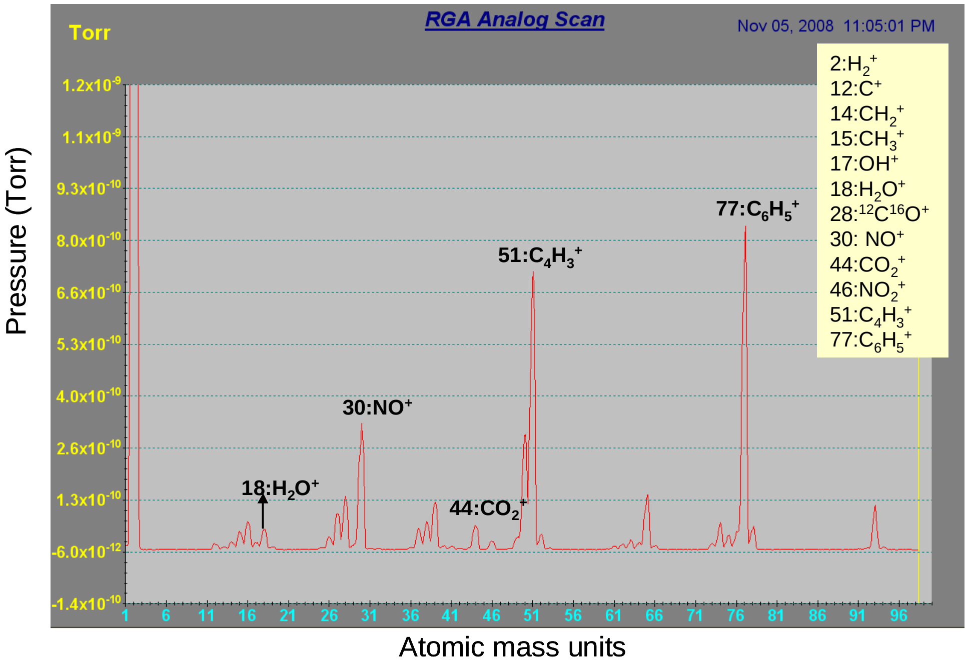

Figure 10. RGA spectrum acquired in the UHV chamber while nitrobenzene is leaking into the chamber at 1 × 10^{-8} Torr after additional purification steps.

2.5.3 Deposition of pentacene

Pentacene was deposited onto the substrate using thermal evaporation. The solid pentacene source was heated to 240 - 250 °C during the deposition. The substrate was kept at room temperature during the pentacene growth. The deposition time ranges between 15 minutes and 20 minutes and the deposition rates were 0.04 - 0.16 molecular layers per minute.

2.6 References

[1] J. A. Stroscio and W. J. Kaiser, *Scanning Tunneling Microscopy* (Academic Press, Boston, 1956).

[2] J. G. Simmons, J. Appl. Phys. **34**, 1793 (1963).

[3] D. J. Griffith, *Introduction to Quantum Mechanics* (Prentice-Hall, Englewood Cliffs, NJ, 1995).

[4] J. A. Appelbaum and W. F. Brinkman, Phys. Rev. **186**, 464 (1969).

[5] T. E. Feuchtwan, P. H. Culter, and N. M. Miskovsky, Phys. Rev. Lett. **99**, 167 (1983).

[6] J. Tersoff and D. R. Hamann, Phys. Rev. Lett. **50**, 1998 (1983).

[7] A. Selloni, P. Carnevali, E. Tosatti, and C. D. Chen, Phys. Rev. B **31**, 2602 (1985).

[8] A. Ishizaka and Y. Shiraki, J. Electrochem. Soc. **133**, 666 (1986).

[9] R. J. Hamers, R. M. Tromp, and J. E. Demuth, Phys. Rev. Lett. **56**, 1972 (1986).

[10] M. Meuris, P. W. Mertens, A. Opdebeeck, H. F. Schmidt, M. Depas, G. Vereecke, M. M. Heyns, and A. Philipossian, Solid State Technol. **38**, 109 (1995).

Chapter 3

Designing Smooth Interfaces

*The content in section 3.6 has been published as *Applied Physics Letters* **92**, 153313 (2008).

3.1 Introduction

The most appropriate substrates for characterization using STM are flat as well as chemically and structurally uniform. It is challenging to find a substrate which is both sufficiently conductive for STM and chemically non-reactive with organic molecules. Clean Si surfaces are flat, but highly reactive and thus inappropriate for studies of growth of organic thin films. This problem can be overcome by modifying Si to reduce the interaction between the substrate and the subsequent organic thin film. Organic crystals in thin films on modified Si are formed with many similarities to pentacene thin films on SiO_2 [1, 2]. Pentacene on organically modified Si thus grows with a crystallographic structure analogous to the structure found in thin film transistors.

STM imaging conditions including bias voltage, tunneling current and scan speed are critically important in obtaining STM images of pentacene. In the previous reports available in the literature, the lying-flat orientation of pentacene molecules have been imaged with -2 V and 200 pA on clean Si (001) and with -1.5 V and 100 pA on a silver thin film on Si (111) [3, 4]. Pentacene molecules on these Ag (111) surfaces were imaged with bias voltages between -3.1 V and 2.4 V and tunneling currents between 70 pA and 120 pA. We have found that imaging conditions similar to these can be used to study pentacene thin films on modified Si surfaces. The best STM images were acquired at -1.9 V and 300 pA for pentacene on clean Si (111) and at

-3.0 V and 300 pA for pentacene on Si (001) modified with cyclopentene, styrene, and nitrobenzene. A complementary set of images at larger scales were acquired using atomic force microscopy (AFM).

3.2 Pentacene on Si (111)

3.2.1 Modification of Si (111)

The first attempt to modify the substrate was made by depositing pentacene on clean Si (111). When pentacene is directly deposited onto clean Si, a strong chemical interaction between the first molecular layer of pentacene and the atomically clean Si (111) surface leads to a flat-lying orientation of pentacene molecules on the surface [5]. The same result has been found on pentacene grown on Si (001) [3]. With further pentacene deposition, crystalline islands form on top of the initial pentacene layer [1, 6]. In the ordered layer of pentacene, the long axes of pentacene molecules are perpendicular to the surface as shown in Fig. 1. Previous studies have

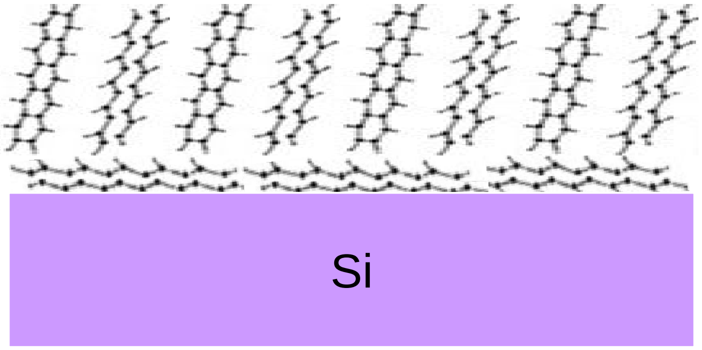

Figure 1. Pentacene molecules in the initial layer lie flat on clean Si and are oriented almost vertically in the subsequent layer.

reported that pentacene deposited on modified Si with organic molecules favor a crystal structure which adopts a vertical orientation of molecules on the surface [7].

3.2.2 Pentacene on Si (111)

We used non-contact AFM to examine the morphology of a pentacene thin film on clean Si (111). The non-contact AFM image in Fig. 2 (a) shows two-dimensional pentacene islands formed on a clean Si (111) surface. The cross section taken along the line in the box of the STM image in Fig. 2(b) shows the height of a pentacene island is 1.6 nm. This is the height of one layer of upright pentacene molecules, indicating that pentacene molecules are oriented vertically with respect to the surface normal on top of the disordered pentacene layer on Si (111).

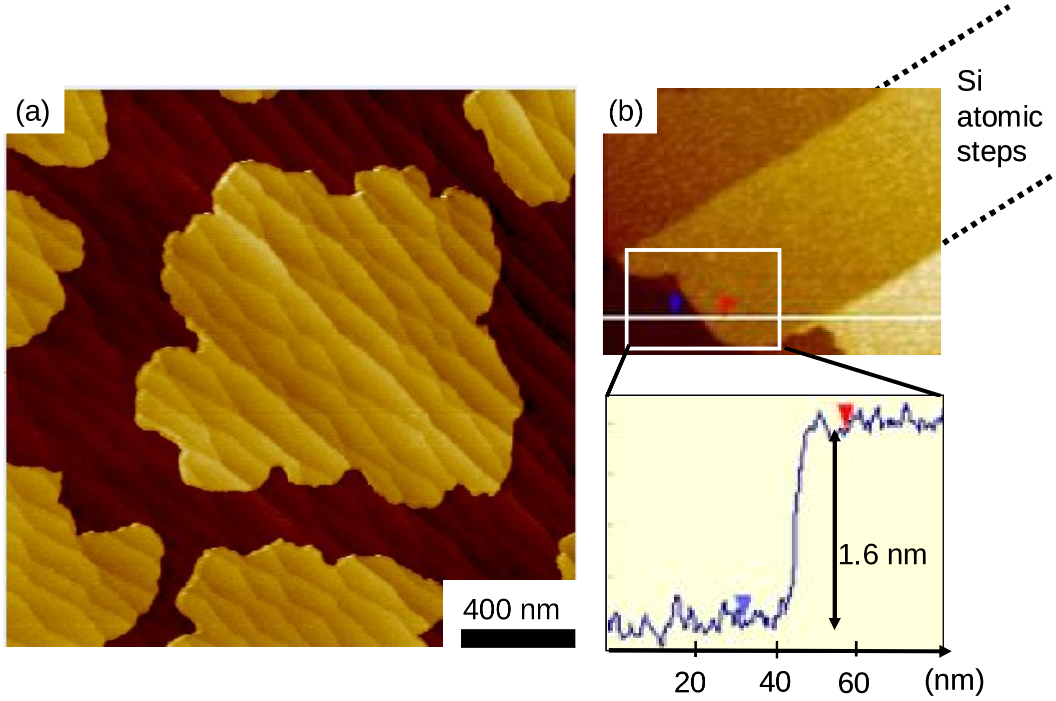

Figure 2. (a) Non-contact AFM image of pentacene islands grown on a disordered layer of pentacene on Si (111). (b) STM image of a pentacene island on Si (111) and the cross section of the area in the box. The dotted lines indicate the locations of Si (111) atomic steps.

Consistent with the predictions in ref. [7], the STM results show that pentacene deposited on pentacene-modified Si (111) forms a structure similar to pentacene on insulator. At a scan scale larger than 200 nm in Fig. 2(b), the pentacene layer is smooth enough to see the underlying Si atomic steps through the pentacene islands. Each of these Si steps is 3.1 Å high. At a molecular scale, we found that the height of the upright pentacene molecules is not uniform.

Pentacene molecules were imaged in a small part of a pentacene island using STM. It is important to achieve molecular resolution to study the structure of defects and electronic properties that will be described in the remaining chapters. One approach to image molecules is to conduct STM experiments at low temperatures to minimize the motion of pentacene molecules.

The STM image acquired at 57 K in Fig. 3 shows individual pentacene molecules on a disordered pentacene layer on Si (111). The molecular basis vectors of the pentacene unit cell (Fig. 3(b)) are marked as arrows in the STM image. The schematic representation in Fig. 3(c) corresponds to the pentacene molecules within the unit cell. The shorter and the longer basis vectors of the pentacene unit cell were labeled as *a* and *b*. The lattice parameters measured from the STM image are 7.4 Å along the longer axis and 5.6 Å along the shorter axis. The literature values determined using x-ray diffraction for the first molecular layer of pentacene on SiO_2 are 7.6 Å along the longer axis and 5.9 Å along the shorter axis of the unit cell [8]. The corresponding lattice constants reported for bulk pentacene are 7.9 Å and 6.1 Å [9]. Our measurements are close to those in the thin film phase, which indicates that pentacene islands formed in the first upright layer at the pentacene/Si (111) interface is structurally similar to pentacene grown next to SiO_2.

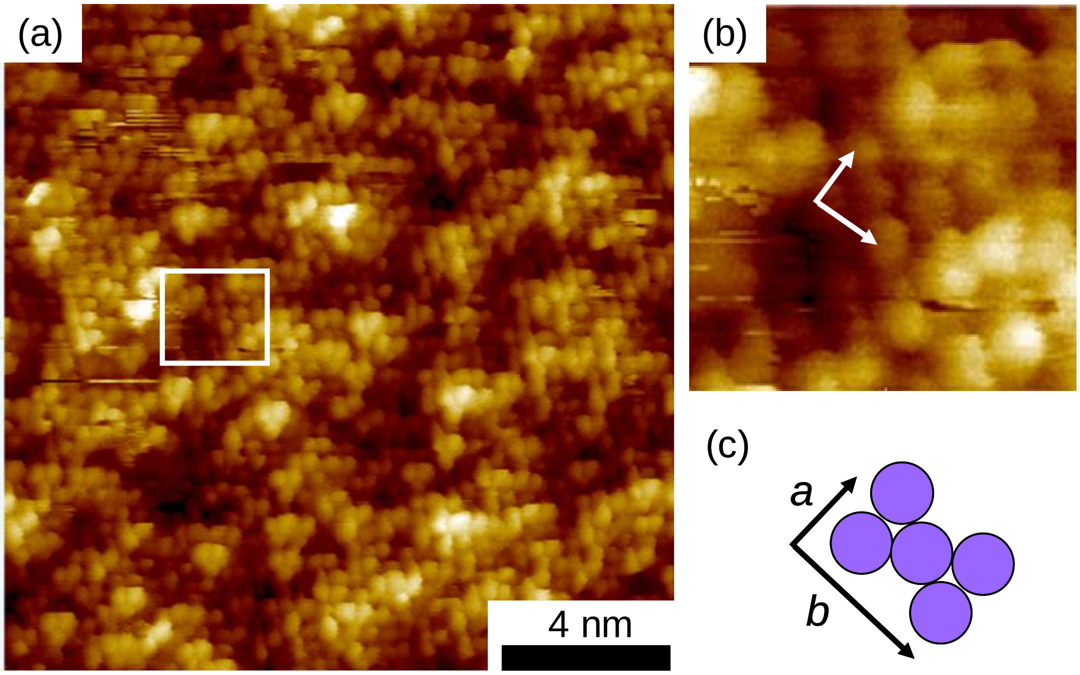

Figure 3. (a) Low-temperature STM image of the first layer of upright pentacene molecules on Si (111) acquired with a tunneling current of 0.23 nA and a bias voltage of -1.9 V at 57 K. (b) Enlarged view of the area in the box in (a). (c) Schematic of pentacene molecules in the unit cell. The arrows indicate the shorter and the longer axes of the pentacene unit cell.

In order to quantitatively describe the variation in height of pentacene molecules exhibited in the STM image, the roughness of the pentacene layer was measured. The roughness was determined by taking an average of 20 measurements of the root-mean-square (rms) variation in height across an STM image with dimensions of 20 nm × 20 nm. The rms roughness of the pentacene molecular layer in Fig. 3(a) is 127 pm. The largest height difference between molecules is 770 pm.

The height variation of pentacene molecules arises from the disordered layer of pentacene initially deposited on clean Si (111). The first molecular layer chemically attached to Si atoms distorts the pentacene molecules and makes the molecule non-planar [5]. Pentacene molecules in the disordered layer lose their original shape because some of the π-bonds within the molecule are broken when the molecular π-orbitals chemically interact with Si atoms. Therefore, the disordered pentacene layer is not as flat as the clean Si (111) surface. The nucleation of the upright pentacene layer occurs on this deformed molecular layer of pentacene on Si (111), which produces roughness in the upright molecular layer of pentacene. Similar conclusions have been drawn for pentacene molecules deposited on Si (001) [7].

Contamination of the pentacene/Si (111) interface by reactive molecules presents a second source of roughness in the pentacene crystal. These are evident after additional exposure of the sample to the residual gas. Pentacene molecules do not effectively passivate the reactive Si (111) surface, possibly due to the large deformed shape in the initially disordered layer. Consequently, reactive sites of Si remain unattached and these are a source for further contamination.

3.3 Modification of Si with small molecules

A more effective way of saturating reactive sites of a Si surface is to use small organic molecules. When Si is terminated with organic molecules such as cyclohexene, pentacene can nucleate and grow in a surface on which the diffusion length of pentacene molecules is greatly increased by the cyclohexene layer on Si (001) [10]. In the next three sections, we described our methods to design chemically stable Si/organic interfaces using cyclopentene, styrene and nitrobenzene.

3.3.1 Si (001) modified with cyclopentene

The attachment of small organic molecules to Si (001) surfaces has been a model system for understanding the interaction of organic molecules with silicon surfaces [11]. Figure 4(a) depicts a molecular model of cyclopentene (C_5H_8) on Si (001), drawn using a simulation tool, Materials Studio (version 5.0) [12]. A cyclopentene molecule and a Si=Si dimer form two Si-C bonds, creating a four-member ring that links the molecule to the Si surface [11]. This reaction produces an organic monolayer in which the rotational order of the underlying Si dimers is translated into the organic film [13]. We used STM to image the cyclopentene layer on Si (001) and to examine if cyclopentene molecules completely passivate the Si (001) surface.

Bare Si (001) surfaces were imaged using STM before the deposition of cyclopentene (Fig. 4 (b)). An STM image of the Si (001) surface after exposure to cyclopentene shows the ordered rows of molecules in Fig. 4(c). The underlying Si atomic steps are seen over the cyclopentene layer. The orientation of cyclopentene molecular rows is rotated by 90° across the Si atomic steps, which indicate the cyclopentene molecules are ordered into the underlying Si dimer rows.

The number of cyclopentene molecules was counted to measure the fraction of cyclopentene molecules attached to the Si dimers. Each cyclopentene molecule appears as a protrusion with respect to the Si (001) surface in Fig. 5. The cross section along the line in the STM image shows that the height of the molecules relative to the substrate is close to 5 Å. This is relatively close to the size of one cyclopentene molecule, which indicates that cyclopentene forms a nearly complete monolayer on Si (001). The spacing between molecules along the row away from vacant sites in Fig. 5(b) is 7.4 Å. This is twice the spacing between two neighboring

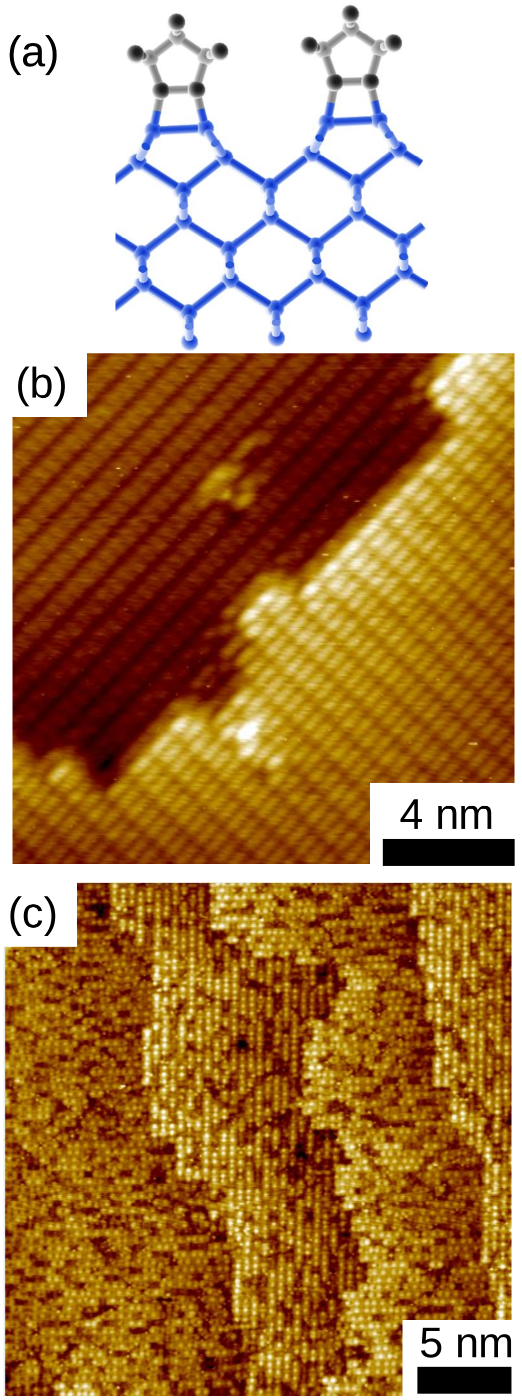

Figure 4. (a) Cyclopentene on Si (001). (b) STM image of clean Si (001). (c) STM image of cyclopentene deposited on Si (001) acquired with V = -1.8 V and 300 pA .

dimers in a dimer row, which indicates that cyclopentene molecules are not attached to every dimer. Thus, the fraction of the Si dimers that are not passivated with molecules in addition to the vacant sites is significantly large. The vacant sites within an area of 5 nm × 5 nm occupy 26% of the Si (001) dimers.

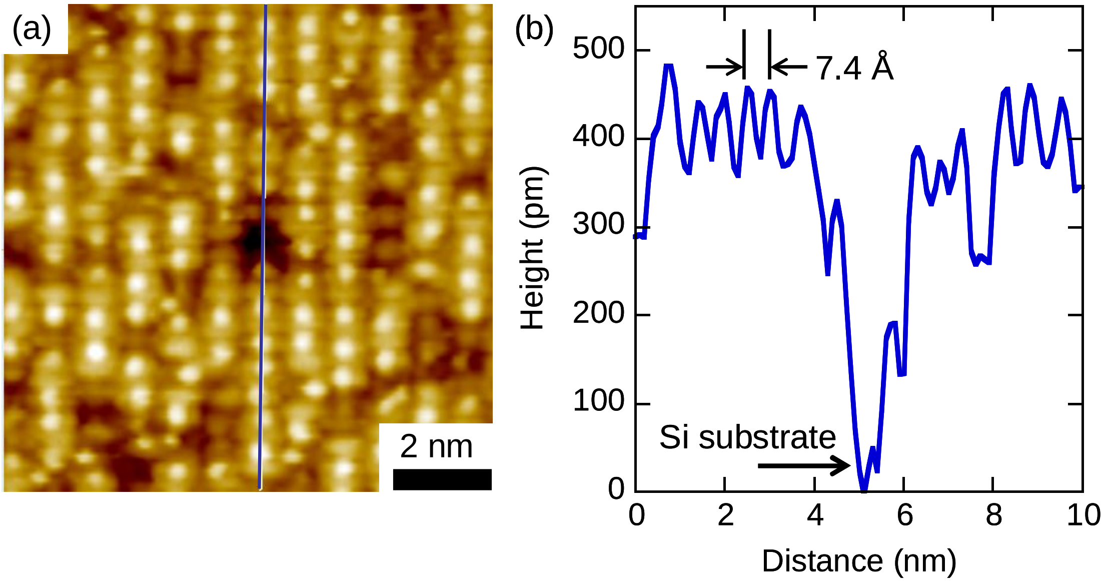

Figure 5. (a) STM image of cyclopentene on Si (001). The image size is 10 nm × 10 nm. (b) Cross section along the line in the STM image.

A comparison between the STM image and the cross section shows that the height difference between cyclopentene molecules ranges between 2 Å and 3Å. The maximum peak-to-valley distance measured in the STM image is 5 Å. As shown in Fig. 5, lower cyclopentene molecules are located next to the vacant sites. The histogram in Fig. 6(a) shows a broader distribution of the height difference of cyclopentene molecules in comparison to that of Si (001) in Fig. 6(b). The rms roughness of the Si (001) surface is 16 pm, while the rms roughness of the cyclopentene/Si (001) layer away from atomic steps is 82 pm. The presence of vacant sites in the cyclopentene layer on Si (001) results in an uneven surface.

The origin of the difficulty in completely passivating Si (001) with cyclopentene lies in the interference between adjacent cyclopentene molecules. A first-principle molecular dynamics

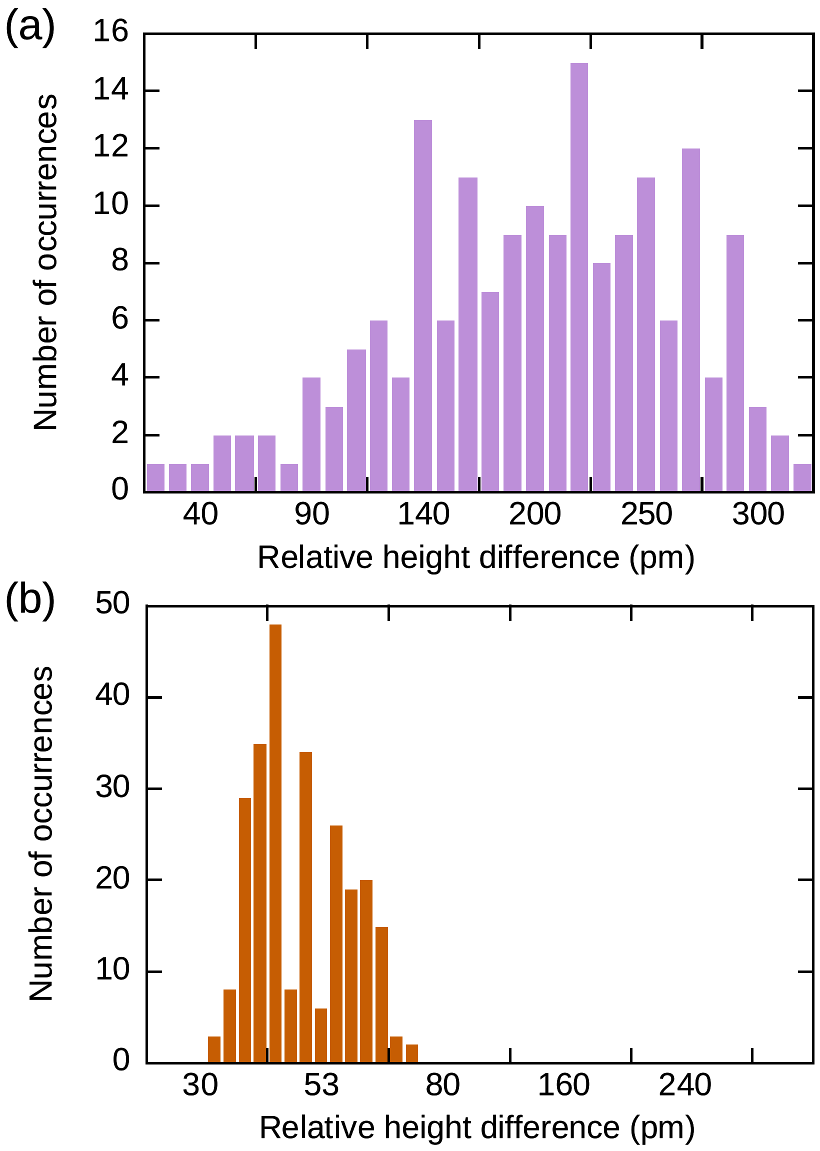

Figure 6. Histograms of relative height difference for (a) Si (001) and (b) cyclopentene on Si (001).

predicted that non-aromatic cyclic-hydrocarbons such as cyclopentene (C_5H_8), cyclohexene (C_6H_{10}) and 1,4-cyclohexadiene (C_6H_8) undergo molecular conformation of different shapes while interacting with Si (001) dimers [14]. This conformational shape keeps the molecules from attaching to every dimer.

3.3.2 Si (001) modified with styrene

One intriguing way to improve surface passivation of Si is the use of small aromatic molecules that can selectively attach to Si (001) dimers. The planar shape of aromatic molecules may result in a high packing density and thus minimize the fraction of the reactive sites on the Si surface. The simplest form among the aromatic molecules is benzene (C_6H_6). It has been experimentally found, however, that a layer of benzene occupies only 25% of the Si (001) dimers due to the multiple bonding structures at room temperature [15]. Therefore, benzene is not appropriate to create an interface at which organic molecules form a monolayer on Si (001).

Styrene ($C_6H_5CH{=}CH_2$) is an aromatic molecule with alternating single and double bonds. The ball-and-stick model in Fig. 7(a) depicts styrene molecules bonded to Si (001) dimers. The attachment of styrene to Si (001) has been studied using both calculations and experimental probes [16, 17]. Studies using STM and Fourier transform infrared spectroscopy (FTIR) show that styrene bonds to Si (001) preferentially through the vinyl group and 90% of the molecules appear in a single bonding geometry at low coverage after exposure of 0.01 L [17]. Whether or not styrene forms a monolayer on Si (001) at high coverage has not proved in ref [17]. No experimental study of high coverage of styrene on Si (001) has been found in the literature.

We imaged styrene molecules deposited on Si (001) using STM. Fig. 7(b) shows an STM image of styrene on Si (001) at high coverage. The STM image does not exhibit any ordered rows of molecules, indicating that the adsorbed molecules do not follow the periodicity of the Si (001) dimers. In comparison to cyclopentene which forms molecular rows along the rotational orientation of underlying Si=Si dimers, styrene molecules are not ordered.

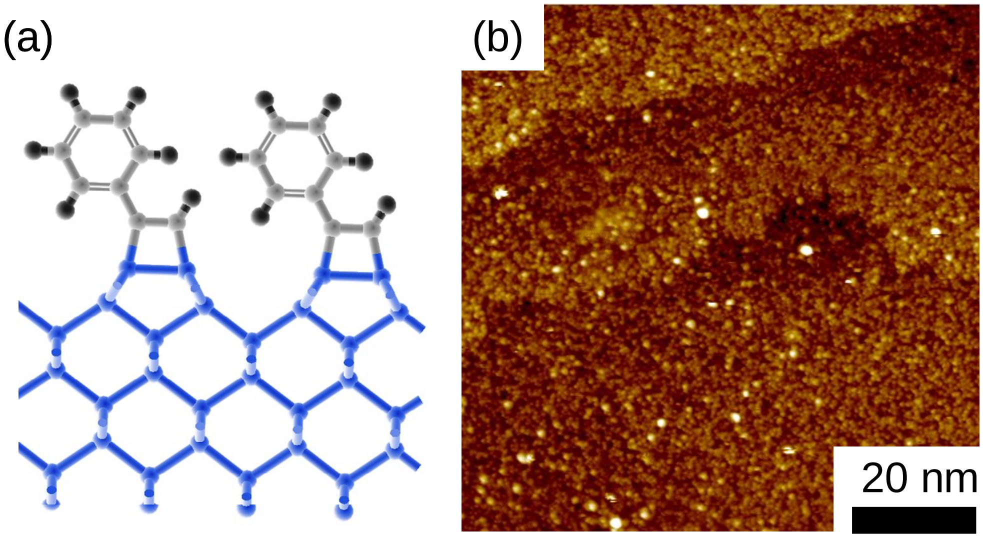

Figure 7. (a) Styrene molecules attached to Si (001) dimers. (b) STM image of styrene on Si (001) acquired with the tunneling conditions of -2.2 V and 200 pA at room temperature.

The lack of ordering in the styrene/Si (001) layer may result from an additional bonding site of styrene molecules on Si (001). Previous studies at low styrene coverages have shown that 90% of styrene molecules are attached on top of dimers of Si (001) and the rest of the molecules are found between dimer rows [17]. Although the molecules attached to the non-primary bonding site occupy 10% of dimers, they can disrupt the ordering of styrene on the Si surface at high coverage. In addition, molecules bonded on top of dimers do not always have the same orientations with respect to the dimer rows. The orientations of the aromatic rings are found on both the left and right-hand sides of a dimer row [17]. A periodic arrangement of the attached molecules may not occur in the styrene/Si (001) layer.

STM was performed on a smaller scan size (50 nm × 50 nm) to search for exposed dimers in Fig. 7(b). A close look of the STM image reveals that there are styrene molecules in the lower regions. In contrast to cyclopentene on Si (001), styrene molecules are closely packed on Si (001) and the sites without molecules are not observed.

3.3.3 Si (001) modified with nitrobenzene

Nitrobenzene is the second aromatic molecule that we found creates a chemically non-reactive interface with Si (001). Nitrobenzene consists of a phenyl ring and a nitro group with two oxygen atoms and one nitrogen atom. Nitrobenzene bonds to Si (001) by initially forming Si-O covalent bonds and transforms to an energetically more stable structure in which oxygen migrates to the backbonds of a Si dimer [18-20]. The predicted structure of nitrobenzene on Si (001) with Si-O bonds is shown in Fig. 8(a).

Nitrobenzene is structurally similar to styrene, which also contains a phenyl ring but includes a vinyl group instead of a nitro group. Auger electron spectroscopy (AES) and Fourier transform infrared spectroscopy studies showed that either nitrogen or oxygen in the nitro group ($-NO_2$) bonds to a Si dimer and the phenyl entity remains in contact [18]. Computational studies using density functional theory (DFT) have predicted that the phenyl group in a nitrobenzene molecule on Si (001) is perpendicular to the surface and remains in a single plane [18]. The experimental and the theoretical studies support the idea that nitrobenzene attached to Si dimers may form a monolayer with a better packing density than styrene on Si (001).

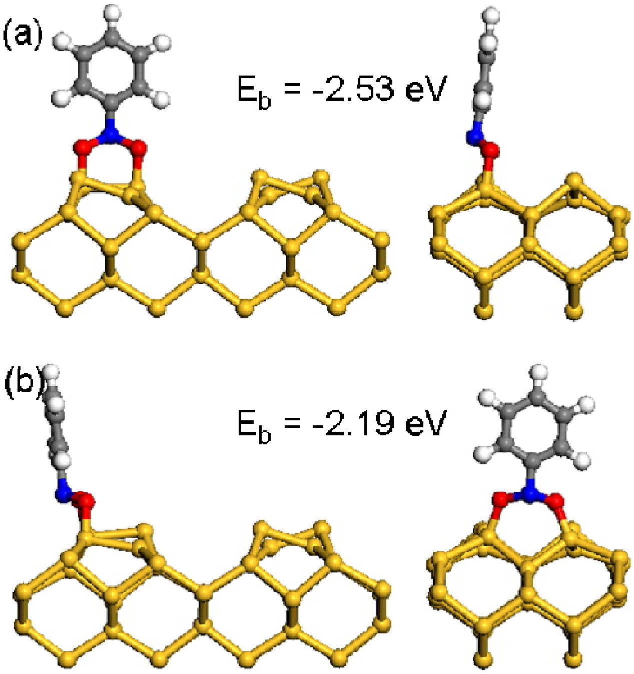

Figure 8. Ball-and-stick model of nitrobenzene on Si (001)-p (4×2). (a) Nitrobenzene molecule attached to one dimer. (b) Nitrobenzene molecule attached to two adjacent dimers. E_b represents binding energy.

3.3.3.1 DFT calculations

A combined study of DFT calculations and *ab initio* molecular dynamics simulations was performed by Dr. Guowen Peng in the research group of Professor Manos Mavrikakis in the Department of Chemical and Biological Engineering to understand how nitrobenzene attaches to Si (001) dimers at high coverage. The binding energy was calculated for three different structures in which nitrobenzene molecules were attached to the Si (001) surfaces in p(4×2), p(2×2), and p(2×1) surface unit cells. The binding energy is defined as the energy difference between the adsorbed system and the sum of the total energies of the clean Si surface and the gas phase of nitrobenzene. The Si (001) surface with the lattice constant of a_0 = 5.46 Å was modeled by a slab geometry with 10 Si atomic layers. The periodic slab is separated by a vacuum gap of 20 Å. The dangling bonds of Si atoms at the bottom of the slab were saturated with hydrogen atoms to mimic the bulk. Nitrobenzene molecules attached to the Si unit cells of p(4×2), p(2×2), and p(2×1) correspond to nitrobenzene coverages of ¼, ½ and 1 monolayer (ML). Here, 1 ML is defined as one nitrobenzene molecule per Si dimer. The calculated binding energies for ¼, ½ and 1 ML were -2.53 eV, -2.54 eV and -2.76 eV, respectively. The lowest binding energy for 1ML of nitrobenzene indicates that nitrobenzene molecules can adsorb on the Si (001) surface with coverage of as high as 1 ML.

The preferred bonding site for nitrobenzene on Si (001) was investigated using DFT calculations. Figure 8(b) shows the nitro group attached to two adjacent Si dimers at the coverage of ¼ ML. The binding energies for two structures in Fig. 8 are -2.53 eV and -2.19 eV, respectively. In comparison to the structure in which a nitrobenzene molecule attached to one dimer at the same coverage, one nitrobenzene molecule attached to two neighboring Si dimers is energetically less stable.

In order to study the possible bonding configurations of nitrobenzene on Si (001), *ab initio* molecular dynamics simulations were performed at coverage of 1 ML of nitrobenzene molecules. The initial bonding structure in Fig. 8 transforms to a more stable structure in which one or two oxygen atoms move into Si backbonds by breaking the weaker N-O bonds as shown in Fig. 9 [18, 19, 21]. In comparison to the binding energy of -2.5 eV in the initial bonding configuration, the binding energies of -6.38 eV and -6.71 eV in two structures in Fig. 9 are much smaller. The results show that it costs less energy to form Si-O bonds between the oxygen atoms and the backbonds of Si (001). Although the structure in Fig. 9(c) has a lower energy than the other two structures, all of the three bonding configurations may coexist.

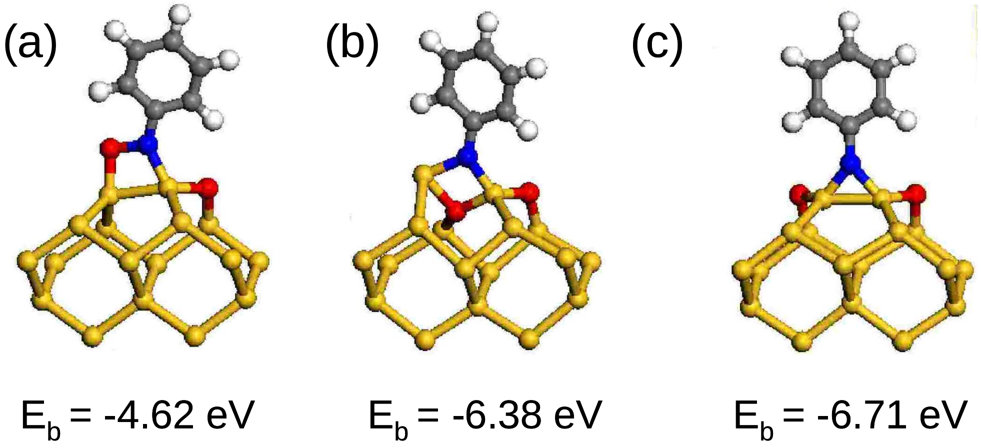

Figure 9. Three different bonding configurations of nitrobenzene on Si (001) with different binding energies.

3.3.3.2. X-ray photoemission spectroscopy (XPS) results

XPS measurements were performed by Rose Ruther, a graduate student in the research group of Professor Robert Hamers, to examine the surface coverage of nitrobenzene molecules on Si (001). The XPS spectra including electrons emitted from Si (2p), C (1s), O (1s) and N (1s) core levels in Fig. 10 were measured using a monochromatized Al K_α radiation (1486.6 eV).

The sample was oriented so that the detected photoelectrons were emitted at a takeoff angle of 45° from the surface plane. The nitrobenzene/Si (001) sample was prepared in UHV and 1.5 ML of pentacene was deposited on nitrobenzene on Si (001) before the sample was taken out of the vacuum chamber for the XPS measurements. The purpose of the ultra thin pentacene film is to minimize contamination while the sample is transported in the air. As a result, the pentacene layer produces a strong carbon peak in the survey spectrum in Fig. 10(a).

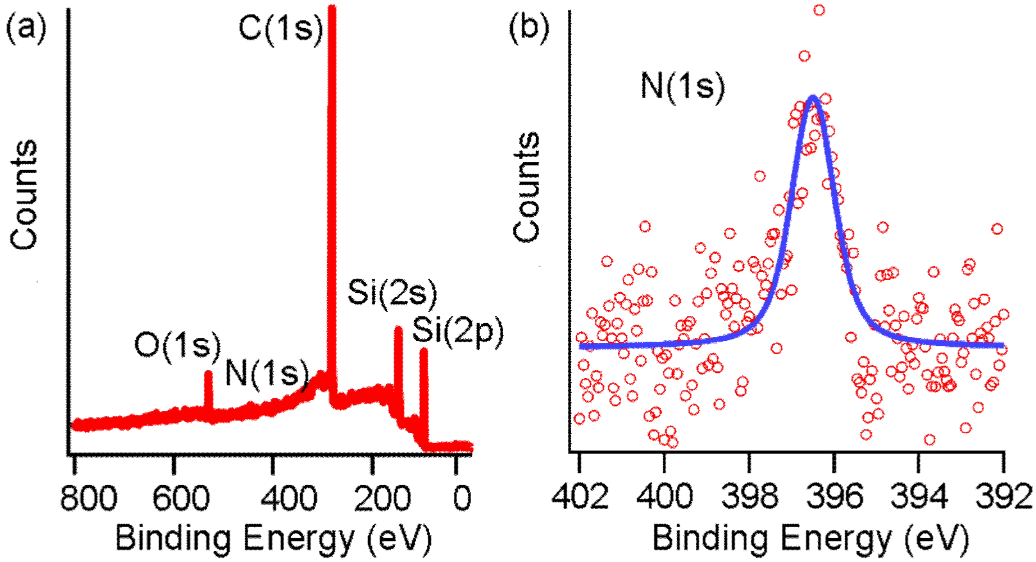

Figure 10. (a) XPS survey spectrum acquired for Si (001) after exposure to nitrobenzene. Pentacene was deposited as a protective layer. (b) High-resolution XPS spectrum of nitrobenzene on Si (001) showing N (1s) peak at the binding energy of 396.5 eV.

The XPS spectrum can be used to estimate the coverage of nitrobenzene by assuming that the only source of nitrogen photoemission is nitrobenzene molecules or fragments of nitrobenzene. The surface concentration of nitrogen atoms was calculated using the integrated intensity of peaks in the XPS spectra. A single peak of the N (1s) spectrum for the Si (001) surface exposed to nitrobenzene appears at 396.5 eV in Fig. 10(b). The probability P per incident photon of creating a detectable photoelectron from a sample is given by

$$P = N\sigma\lambda, \qquad (1)$$

where N is the number of atoms/cm^2 , σ is the photoelectric cross section, and λ is the electron escape depth [22]. The number of electrons that can escape from a solid decreases with depth as $e^{-t/\lambda}$ where t is a layer thickness [22]. The concentration of an element in a sample depends on the cross section, the escape depth, and the integrated intensity areas. The number of nitrogen atoms per unit area can be calculated according to

$$\sigma_N = \frac{A_N S_{Si}}{A_{Si} S_N} \rho_{Si} \lambda_{Si,Si} \sin(45°) \frac{e^{t/(\lambda_{N,pentacene} \sin(45°))}}{e^{t/(\lambda_{Si,pentacene} \sin(45°))}} \qquad (2)$$

where σ_N is the surface concentration of nitrogen atoms, ρ_{Si} is the number of Si atoms per unit volume of Si, and t is the thickness of the pentacene layer [23]. A_N and A_{si} are the integrated intensities of nitrogen and Si, and S_{si} and S_n are atomic sensitivity factors. For Si, we used $\lambda_{\text{Si, Si}}$ of 31.6 Å [24]. Laibinis *et al.* has reported that the electron escape depth of a self-assembled monolayer deposited on metal such as Au, Ag, and Cu could be fit by the empirical equation

$$\lambda = 9.0 + (0.022) \times E \qquad (3)$$

where E is the kinetic energy [25]. This yields that the escape depths for N and Si photoelectrons in the pentacene layer are 33 Å for $\lambda_{\text{N, pentacene}}$ and 40 Å for $\lambda_{\text{Si, pentacen}}$ [25].

In order to independently determine the thickness, t, we can use the XPS data taken at 45° and 75°.

$$\sigma_N = \frac{A_{O,45°} S_{Si}}{A_{Si,45°} S_N} \rho_{Si} \lambda_{Si,Si} \, sin(45°) \frac{e^{t/(\lambda_{O,pentacene} sin(45°))}}{e^{t/(\lambda_{Si,pentacene} sin(45°))}} \qquad (4)$$

$$\sigma_N = \frac{A_{O,75°} S_{Si}}{A_{Si,75°} S_N} \rho_{Si} \lambda_{Si,Si} \, sin(75°) \frac{e^{t/(\lambda_{O,pentacene} sin(75°))}}{e^{t/(\lambda_{Si,pentacene} sin(75°))}} \qquad (5)$$

By setting Equation (4) and (5) at both angles equal to each other and solving for the thickness, we obtain the thickness of $t = 2$ nm. The surface coverage is relatively insensitive to how thick the pentacene layer is. The surface concentration of nitrogen atoms derived using equation (2) is 4×10^{14} cm^{-2}, which is close to the number of Si (001) dimers, 3×10^{14} cm^{-2}. The XPS results show a high coverage of nitrogen atoms on Si (001).

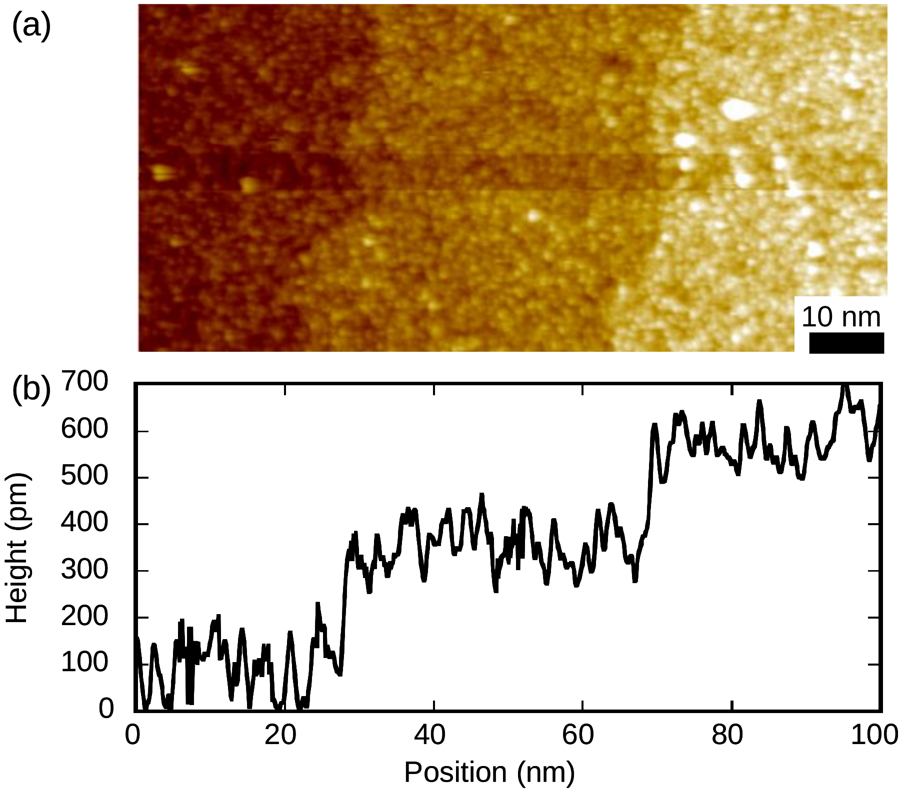

Figure 11. (a) STM image of nitrobenzene on Si (001) acquired with -1.9 V and 250 pA. (b) Cross section across the STM image showing the underlying Si (001) steps.

3.3.3.3. STM results

The Si (001) surface was imaged after exposure to nitrobenzene in order to examine the surface passivation of Si (001) with nitrobenzene molecules. The STM image in Fig. 11(a) shows that the Si (001) surface is almost entirely covered with nitrobenzene molecules. The STM image also shows the single-height atomic steps of Si (001) over the nitrobenzene layer. The mean step height measured from a series of 100-nm long cross sections of the STM image in Fig. 11(b) is close to the atomic step height of Si (001), which indicates that nitrobenzene forms a monolayer on Si (001).

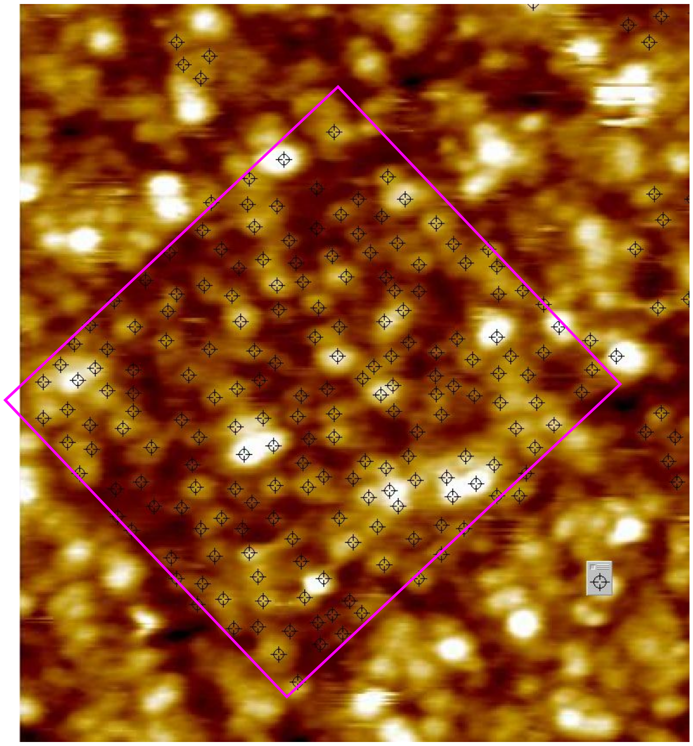

Figure 12. STM image of nitrobenzene on Si (001). The number of molecules in the marked area was counted to calculate the nitrobenzene coverage.

To measure the coverage of nitrobenzene molecules on Si (001), the number of nitrobenzene molecules was counted in STM images with different scan sizes and scan rates. Figure 12 shows one of the STM images used for the statistical study. Only the molecules that are clearly visible were counted in the rectangular area and compared with the number of dimers calculated in the same area. The number of molecules found in an area of 7.7 nm × 8.4 nm was 192. Since there are 221 dimers in the same area, the fraction of the occupied sites with nitrobenzene is 87% of the Si dimers. A summary of the fraction of nitrobenzene molecules occupying Si (001) dimers is shown in Table 1. The mean fraction of nitrobenzene molecules measured in two STM images is 86%. The high coverage of nitrobenzene molecules on Si (001) observed in the STM image is consistent with the XPS result.

Data number	**Area (nm^2)**	**Number of molecules**	**Number of dimers**	**Fraction (%)**
1	36	90	102	88
2	35	99	120	83
3	27	82	94	87
4	32	94	110	86
Mean				86

Table 1. The number of nitrobenzene molecules measured in STM images and the number of Si dimers calculated for the same area.

The STM image shows that the nitrobenzene layer lacks long-range order. The extensions of the nitrobenzene molecular rows are schematically drawn with bars in Fig. 13(a). The bars underneath the STM image in Fig. 13(b) depict the orientation of the dimer rows of Si (001). A comparison between the bare Si (001) surface and the nitrobenzene/Si (001) layer reveals that the in-plane orientations of the nitrobenzene molecular rows and the Si dimer rows are similar. The cross section along the line perpendicular to the molecular rows in Fig. 14 shows that the separation between the neighboring molecular rows is 8.6 Å, which is close to the separation between dimer rows, 7.6 Å. Nitrobenzene molecules form along the dimer rows of Si (001) in short-range order.

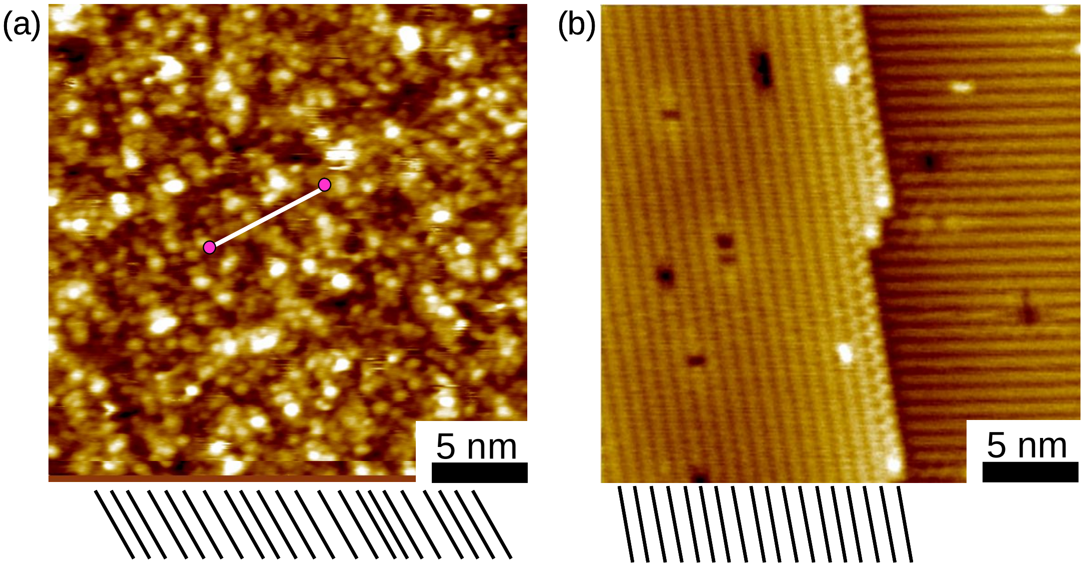

Figure 13. STM images of (a) nitrobenzene on Si (001) and (b) bare Si (001). The bars underneath the images represent that the directions of (a) the molecular rows and (b) the Si (001) dimer rows. The line in the STM image is drawn perpendicular to the dimer rows.

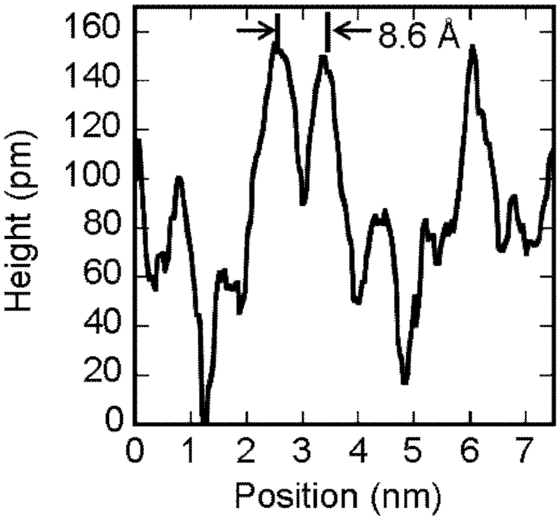

Figure 14. Cross section along the line in the STM image in Fig. 13(a). The separation between molecular rows is close to the separation between dimer rows.

The ordering of molecular rows of nitrobenzene can be interrupted by the existence of several orientations of nitrobenzene molecules. We hypothesize that the variation in height of nitrobenzene molecules may come from different tilting orientations of aromatic rings of molecules with respect to the substrate. DFT calculations predicted that the bonding configurations differ in that the orientation of the phenyl ring is different in each configuration. Different tilting orientations of phenyl rings, thus, lead to the variation in height of nitrobenzene molecules. To test this hypothesis, we measured the height difference between nitrobenzene molecules to examine the height distribution in the nitrobenzene/Si (001) layer. The relative height difference between nitrobenzene molecules ranges from 60 pm to 200 pm, which can be interpreted as diverse orientations of phenyl rings and thus can interrupt long-range order in the nitrobenzene/Si (001) layer.

3.4 Pentacene thin films on organically modified Si (001)

Pentacene was deposited on Si (001) modified with three organic molecules to investigate which substrate yields a smooth pentacene thin film.

3.4.1 Pentacene on cyclopentene/Si (001)

Pentacene was first grown on Si (001) modified with cyclopentene to investigate whether pentacene on cyclopentene/Si (001) is structurally similar to pentacene on an insulating surface. Fourier transform infrared spectroscopy (FTIR) results have shown that there is no bond formation between cyclopentene/Si (001) and pentacene and thus pentacene islands grown on cyclopentene/Si (001) forms a crystalline structure [7]. Structural studies showing the morphology of a pentacene thin film on cyclopentene/Si (001) have not been found in the literature.

We imaged pentacene islands formed in the cyclopentene/Si (001) layer to examine the surface topography. The sectional profile in Fig. 15(a) shows that the island height of pentacene grown on the cyclopentene/Si (001) is 1.6 nm, which indicates that the pentacene molecular layer on cyclopentene/Si (001) is composed of molecules with their long axes oriented along the surface normal.

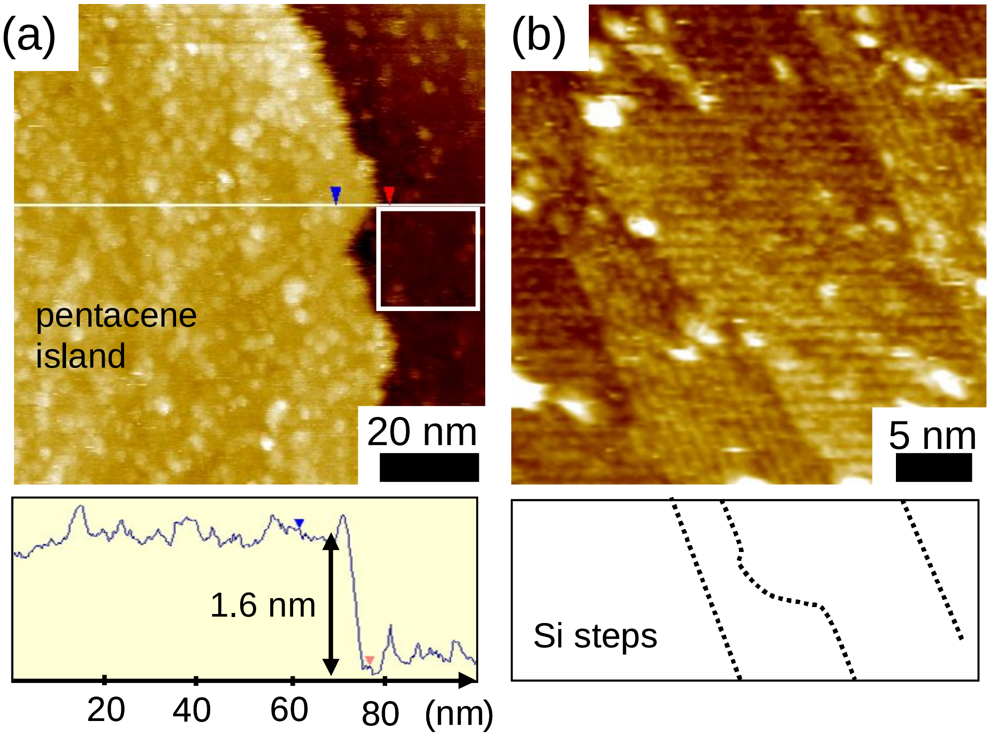

Figure 15. (a) STM image of submonolayer pentacene island grown on Si (001) modified with cyclopentene. (b) Larger view of the area in the box in (a). An ordered layer of cyclopentene on Si (001) can still be seen outside the pentacene island.

A larger view of the rectangular area outside the pentacene island shows ordered rows of cyclopentene molecules following the orientations of underlying Si dimers in Fig. 15(b). Pentacene islands of the upright orientation of molecules are formed in the first molecular, which is analogous to the thin film phase of pentacene on SiO_2. The results indicate that the structure of pentacene on cyclopentene/Si (001) can be used to study the interface between pentacene and SiO_2.

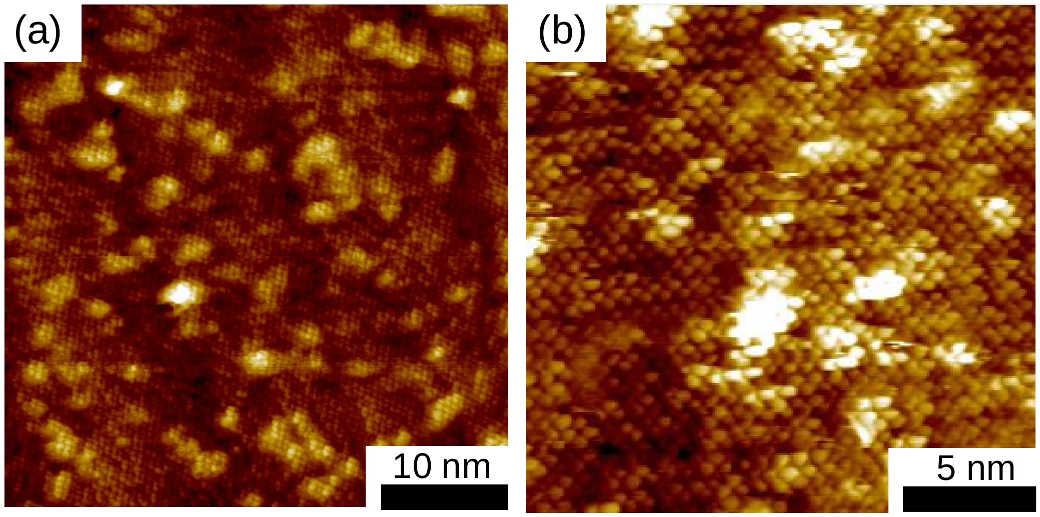

Figure 16. (a) Low temperature STM image of pentacene on Si (001) modified with cyclopentene acquired with V = -3 V and 300 pA at 57 K. (b) Larger view of the STM image in (a).

Molecular-scale images of a pentacene island on cyclopentene/Si (001) are shown in Fig. 16. In addition to the pentacene molecules, there are clusters of molecules that appear higher. These clusters are found uniformly across the surface. Because of the presence of higher molecules, the rms roughness of the surface in Fig. 16(b) increases to 130 pm from 66 pm measured in the area away from high molecules. These high molecules become more evident with prolonged exposure of sample in the chamber. Therefore, they may arise from contamination due to reactive molecules reaching the cyclopentene/Si (001) surface. A similar phenomenon was observed in pentacene on Si (111). We hypothesize that this is a result of chemically reactive sites exposed on the cyclopentene/Si (001) surface. To test this hypothesis, we chose an organic molecule that can improve surface passivation of Si (001), described in the next section.

3.4.2 Pentacene on styrene/Si (001)

In the previous section, we found that surface passivation of Si is crucial to create a chemically non-reactive surface for the growth of a pentacene thin film. Since styrene packs more densely on the Si (001) surface with a minimal fraction of sites with bare Si dimers, we hypothesize that styrene molecules effectively keep impinging pentacene molecules from unpassivated dimers.

STM was used to image submonolayer pentacene islands formed on styrene/Si (001). The STM image in Fig. 17(a) shows that there are low regions in which the presence of pentacene molecules is not apparent. A closer look of the STM image showed that there are pentacene molecules in the lower regions.

To cover the lower regions in the first molecular layer of pentacene, more pentacene was deposited. The second molecular layer of pentacene on styrene/Si (001) is shown in Fig. 17(b). The height variation in the second molecular layer is greatly reduced in comparison to the first molecular layer. The roughness of the pentacene molecular layers on styrene /Si (001) was determined by measuring a series of the rms distance along a section of 50 nm. The rms roughness measured in the second molecular layer was 49 pm, which is significantly smaller than the rms roughness of 83 pm in the first molecular layer. The defects in the second molecular layer of pentacene in Fig. 17(b) are further described in Chapter 4.

The morphology of the surface does not change with prolonged exposure of the sample to the residual gas, which contrasts to the pentacene thin film on cyclopentene/Si (001), which indicates that the pentacene molecular layer on styrene/Si (001) is chemically less reactive than pentacene on cyclopentene/Si (001) layer.

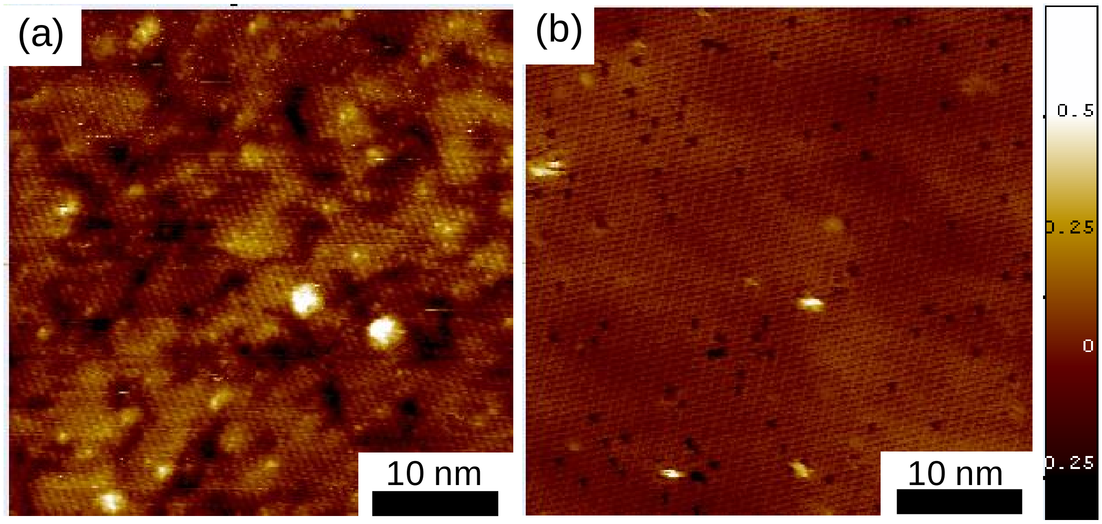

Figure 17. STM images of (a) the first molecular layer and (b) the second molecular layer of pentacene on styrene/Si (001). The scale bar shows the height in nm.

3.4.3 Pentacene on nitrobenzene/Si (001)

The surface of pentacene deposited on nitrobenzene/Si (001) was imaged using STM. The large-scale STM image (500 nm × 500 nm) in Fig. 18(a) and the molecular-scale image in Fig. 18(b) show that the morphology of pentacene on nitrobenzene/Si (001) and that of pentacene on styrene/Si (001) are similar. The difference between two structures is the presence of higher molecules which become evident with prolonged exposure of the pentacene on nitrobenzene/Si (001) sample to the residual gas of the chamber.

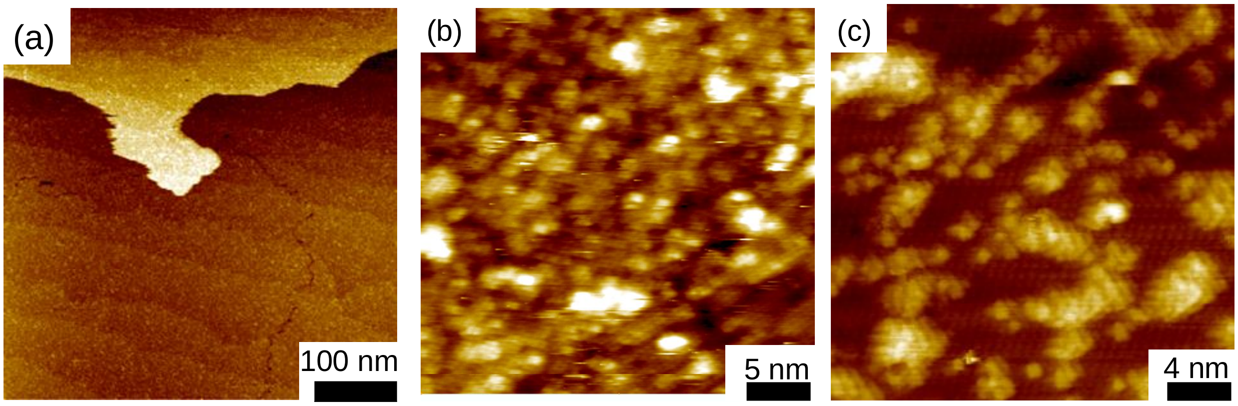

Figure 18. (a) STM image of pentacene on nitrobenzene/Si (001). (b) Pentacene thin film grown on the non-contaminated nitrobenzene/Si (001) surface. (c) Pentacene thin film grown on the contaminated nitrobenzene/Si (001) surface.

The origin of higher molecules may come from oxidation of the surface by the small amount of water in the UHV residual gas. The STM image in Fig. 18(c) shows the pentacene thin film grown on Si (001) modified with nitrobenzene containing water. Nitrobenzene used for this sample did not go through extra purification by annealing the nitrobenzene source as described in Chapter 2. The reactive molecules clustered in the pentacene molecular layer in Fig. 18(c) cover the larger surface area than those in Fig. 18(b).

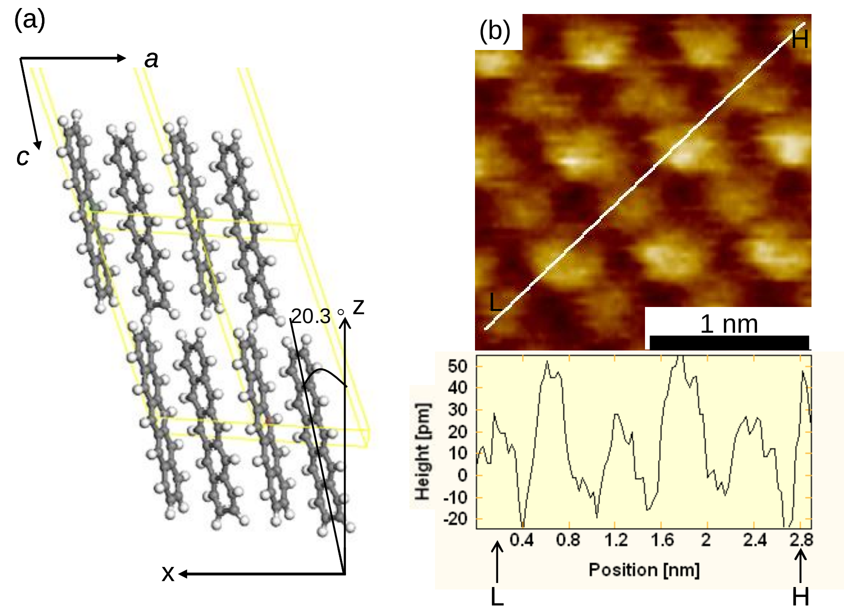

Figure 19. (a) Bulk structure of pentacene. (b) STM image of pentacene molecules in high and low rows and the corresponding cross section.

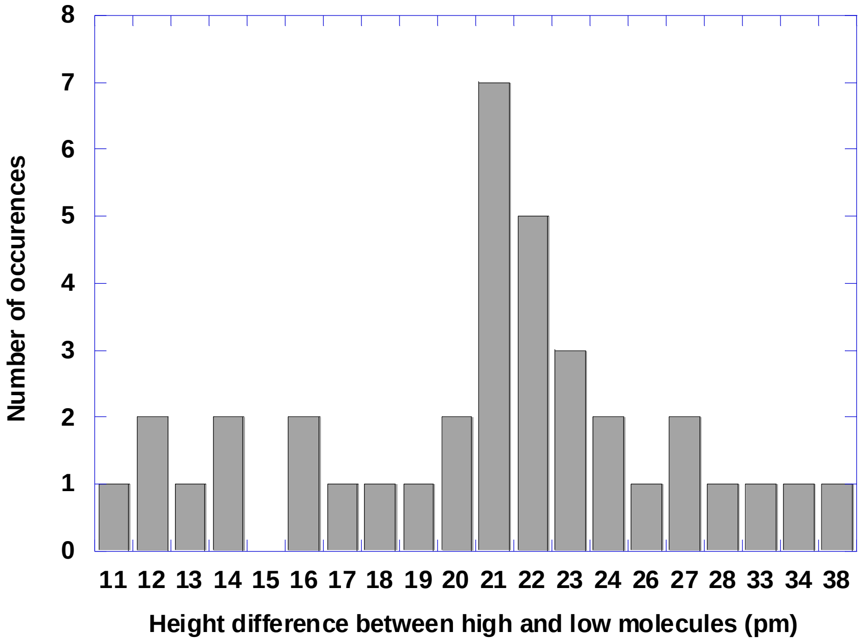

Figure 20. Histogram of height differences between high and low molecules.

3.5 Resolving pentacene molecules

The bulk structure of pentacene was compared to STM images to relate the molecular basis sites of the pentacene unit cell to the molecular features in the STM image. There are two inequivalent sites for pentacene molecules within the triclinic unit cell. These molecules are rotated with respect to the axes of the triclinic structure.

An important geometric detail is that two molecules within the pentacene unit cell are tilted by 22.1° and 20.3° with respect to the surface normal [26]. The height of two molecules is thus different along the *z* axis in Fig. 19(a). Since the length of a pentacene molecule is 1.6 nm, the heights of two inequivalent pentacene molecules are

$$1.6\ \ nm \times cos\,20.3^{\circ} = 1.50\ \ nm \text{ and} \tag{6}$$

$$1.6\ \ nm \times cos\,22.2^{\circ} = 1.48\ \ nm\,. \tag{7}$$

Therefore, the height difference of two molecules along the *z* axis is 20 pm, which indicates one molecule extends further along the surface normal and thus would appear higher in STM images.

The STM image in Fig. 19(b) shows alternating rows of molecules at different heights. The sectional profile in Fig. 19(b) shows that the height difference between high and low molecules measured from the STM image is 20 pm. Figure 20 shows a histogram of the height difference between two neighboring high and low molecules as a function of the number of occurrences measured for many other images. The average of 44 measurements of the height difference between adjacent rows of high and low molecules was 21 pm. This is very close to the calculated value, 20 pm. The comparison between the bulk model and the STM image shows that high and low molecules in the STM image correspond to the two inequivalent molecular sites in the unit cell.

3.6 Crystallographic orientations of pentacene islands

The (001) and (00$\bar{1}$) surfaces in the bulk unit cell of pentacene are related by the inversion center of the P$\bar{1}$ symmetry of the pentacene crystal. A right-handed structure at one surface becomes left-handed when it is inverted. The distinction between the (001) and (00$\bar{1}$) planes is important because we can use it to identify the position of a molecule relative to the position of a defect. In experiments, we often observe (001) planes of pentacene. STM was used to image different faces of a pentacene crystal. Pentacene thin films consist of islands of molecular layers where either the (001) or (00$\bar{1}$) plane is exposed.

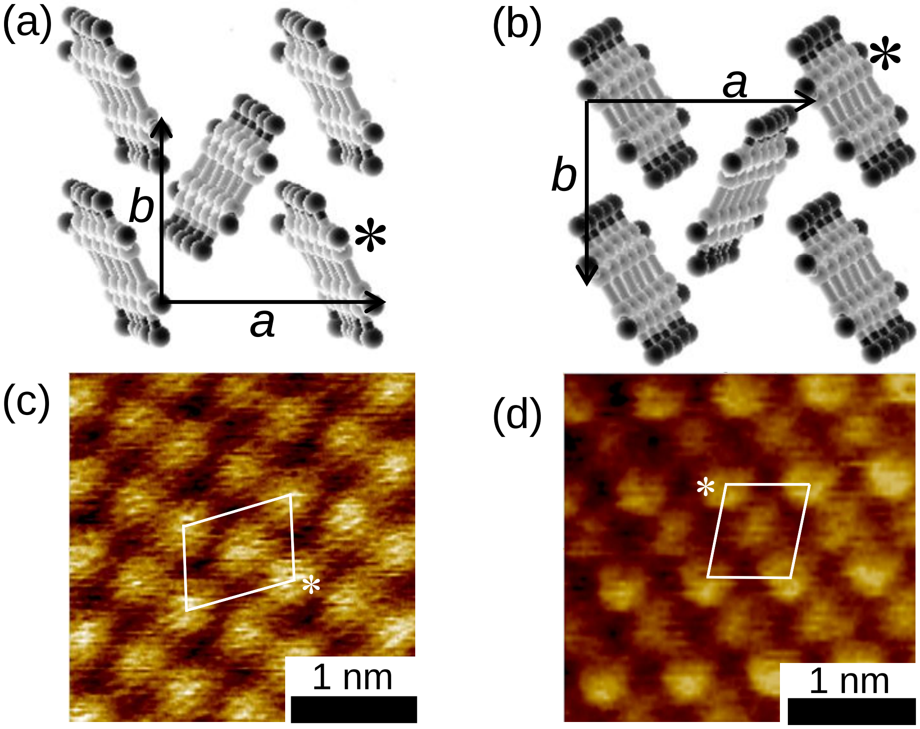

Figure 21. Bulk models of the pentacene unit cell for (a) the (001) surface and for (b) the (00$\bar{1}$) surface. STM images of (c) the (001) and (d) the (00$\bar{1}$) surfaces.

Molecular models based on the bulk structure of pentacene are shown in Fig. 21 for the (001) and $(00\bar{1})$ surfaces [9]. In the (001) plane, the center molecule is closest to one of the neighbors in the projection of the exposed end of each molecule. This closest neighbor is marked with a star in Fig. 21(a). In order to reach its neighbor in the longer side of the unit cell, *a*, the molecule marked with a start needs to move in a clockwise direction in the (001) plane. Similarly, in the $(00\bar{1})$ plane, the molecule closest to the center molecule is marked with a star. From this molecule, its neighbor in a clockwise direction lies along the shorter side of the unit cell, *b*.

Structures associated with the (001) and $(00\bar{1})$ faces that can be distinguished in STM images. The pentacene unit cell is drawn in the STM images which exhibits the lower molecule in the center of the unit cell in Fig. 21(c) and (d). One of the high molecules adjacent to the low center molecule is marked with a star. In Fig. 21(c), the nearest neighbor at the longer edge can be reached when the molecule marked with a star moves in a clockwise direction, indicating that the STM image shows the (001) surface. In Fig. 21(b), the next nearest neighbor from molecule marked with a star in a clockwise direction lies along the shorter side of the unit cell, *b*, which represent the $(00\bar{1})$ surface.

The distinction between thin films exhibiting the (001) and $(00\bar{1})$ surfaces has not been made in the literature. To date, theoretical studies have been conducted only on the (001) surface [27, 28], but experiments are highly likely to produce a mixture of the two orientations. It has been suspected that pentacene crystals are oriented so that the (001) surface is parallel to the substrate because the (001) surface exhibits the lowest surface energy [28]. The surface energy for the $(00\bar{1})$ is not known, but it seems likely that both surfaces will have very similar energies due to their similar structures. Our STM results show pentacene crystals of both the (001) and $(00\bar{1})$ surfaces.

3.7 Conclusion

In comparison to the ordered rows of cyclopentene on Si (001), no ordered lattice was shown in the styrene on Si (001) layer. However, styrene on Si (001) provides a sufficiently smooth and conductive substrate for STM studies. Pentacene thin films grown on modified silicon with pentacene, cyclopentene, styrene and nitrobenzene are structurally similar to those grown on insulating substrates and thus pentacene on modified Si can be used as a conducting analogue to pentacene on SiO_2 for interface studies. The second molecular layer of pentacene on styrene/Si (001) forms smooth islands to probe individual structural defects. STM can be used to distinguish the (001) and $(00\bar{1})$ planes of a pentacene crystal.

3.8 References

[1] F.-J. Meyer zu Heringdorf, M. C. Reuter, and R. M. Tromp, Nature **412**, 517 (2001).

[2] A. Tersigni, J. Shi, D. T. Jian, and X. R. Qin, Phys. Rev. B **74**, 205326 (2006).

[3] G. Hughes, J. Roche, D. Carty, T. Cafolla, and K. E. Smith, J. Vac. Sci. Technol. B **20**, 1620 (2002).

[4] Ph. Guaino, A. A. Cafolla, O. McDonald, D. Carty, G. Sheerin, and G. Hughes, J. Phys.: Condens. Matter **15**, S2693 (2003).

[5] G. Hughes, D. Carty, and A. A. Cafolla, Surf. Sci. **582**, 90 (2005).

[6] T. Schwieger, X. Liu, D. Olligs, M. Knupfer, and Th. Schmidt, J. Appl. Phys. **96**, 5596 (2004).

[7] K. P. Weidkamp, C. A. Hacker, M. P. Swartz, X. Cao, R. M. Tromp, and R. J. Hamers, J. Phys. Chem. **107**, 11142 (2003).

[8] S. Fritz, S. M. Martin, C. D. Frisbie, M. D. Ward, and M. F. Toney, J. Am. Chem. Soc. **126**, 4084 (2004).

[9] R. B. Campbell, J. Monteath Robertson, and J. Trotter, Acta. Cryst. **14**, 705 (1961).

[10] F.-J. Meyer zu Heringdorf, M. C. Reuter, and R. M. Tromp, Appl. Phys. A **78**, 787 (2004).

[11] R. J. Hamers, J. S. Hovis, S. Lee, H. Liu, and J. Shan, J. Phys. Chem. B **101**, 1489 (1997).

[12] Accelrys Software Inc.

[13] H. Liu and R. J. Hamers, J. Am. Chem. Soc. **119**, 7593 (1997).

[14] K. Akagi, S. Tsuneyuki, Y. Yamashita, K. Hamaguchi, and J. Yoshinobu, Appl. Surf. Sci. **234**, 162 (2004).

[15] G. P. Lopinski, T. M. Fortier, D. J. Moffatt, and R. A. Wolkow, J. Vac. Sci. Technol. A **16**, 1037 (1998).

[16] A. Calzorari, A. Ruini, E. Molinari, and M. J. Caldas, Phys. Rev. B **73**, 125420 (2006).

[17] M. P. Schwartz, M. D. Ellison, S. K. Coulter, J. S. Hovis, and R. J. Hamers, J. Am. Chem. Soc. **122**, 8529 (2000).

[18] S. Bocharov and A. V. Teplyakov, Surf. Sci. **573**, 403 (2004).

[19] L. P. Mendez De Leo and A. V. Teplyakov, J. Phys. Chem. B **110**, 6899 (2006).

[20] J. A. Barriocanal and D. J. Doren, J. Vac. Sci. Technol. A **18**, 1959 (2000).

[21] J. Eng, I. A. Hubner, J. Barriocanal, R. L. Opila, and D. J. Doren, J. Appl. Phys. **95**, 1963 (2004).

[22] L. C. Feldman and J. W. Mayer, *Fundamentals of Surface and Thin Film Analysis* (Elsevier Science Publishing Co., Inc., New York, 1930).

[23] H. Kim, P. E. Colavita, P. Paoprasert, P. Gopalan, T. F. Kuech, and R. J. Hamers, Surf. Sci. **602**, 2382 (2008).

[24] S. Tanuma, C. J. Powell, and D. R. Penn, Surf. Interface Anal. **11**, 577 (1988).

[25] P. E. Laibinis, C. D. Bain, and G. M. Whitesides, J. Phys. Chem. **95**, 7017 (2002).

[26] R. B. Campbell and J. Monteath Robertson, Acta Cryst. **15**, 289 (1962).

[27] C. D. Dimitrakopoulos, A. R. Brown, and A. Pomp, J. Appl. Phys. **80**, 2501 (1996).

[28] J. E. Northrup, M. L. Tiago, and S. G. Louie, Phys. Rev. B **66**, 121404 (R) (2002).

Chapter 4

Vacancies in Pentacene Thin Films

* The content of this chapter has been published as *Applied Physics Letters* **92**, 153313 (2008).

4.1 Introduction

Vacancies in organic crystals modify the electronic states associated with the molecules surrounding each vacancy [1]. Spectroscopic measurements and calculations have shown that molecular vacancies trap or scatter charge carriers [1-3]. The distortion of the crystalline lattice near vacancies is important in two respects. First, the positions of molecules are important in determining the energy required to form the vacancy and the thermodynamic stability of this defect [4]. Calculations of the enthalpy of vacancy formation predict that the environment with relaxed molecules surrounding a vacancy is energetically more stable than that in a perfect crystal [4]. The deformed lattice near a vacancy results in a change in the electronic states of molecules in the defect region [5, 6]. This distortion of crystalline lattice can thus effectively produce traps for holes or electrons.

The structure of vacancies in organic crystals has been studied using theoretical models and calculations [4, 7, 8]. Small displacements of molecules near vacancies from their ideal crystal sites occur in naphthalene and anthracene [4, 8]. Craig *et al.* calculated the center-of-mass displacements of relaxed molecules around a vacancy in naphthalene [4]. Their results show that none of the naphthalene molecules are displaced by more than 10 pm from their perfect crystal sites [4]. Similarly, the maximum displacement of anthracene molecules surrounding a vacancy was calculated to be 13 pm [8]. The displacements of molecules due to relaxation near a vacancy in naphthalene and anthracene are so small that structural distortions near vacancies have been ignored in the electronic states calculations [1]. Calculations of the electronic states near vacancies in pentacene have also used unrelaxed crystals of pentacene because the crystal structure is similar to those of naphthalene and anthracene [1, 7].

Electron diffuse scattering studies have found structural evidence for distortion of the crystalline lattice near vacancies [9]. A quantitative description of structural distortion around a vacancy in pentacene, however, was not derived in their work. The displacements of molecules have not been measured experimentally.

A challenge involved in characterizing the structure of a vacancy is to image individual vacancies. Images with molecular resolution are required to identify vacancies. We have used STM to perform the molecular-scale structural studies of defects in pentacene thin films. We provide evidence for large structural distortions in the vicinity of vacancies in crystalline pentacene islands on a modified silicon substrate. Probing the real-space structure of vacancies using STM allows us to measure the concentration of vacancies and quantitatively describe the structure of the surrounding molecules of a vacancy.

4.2 Vacancies in pentacene thin films

We have studied structural defects in pentacene islands grown on styrene/Si (001). Several STM scans were performed in each molecular layer with scan sizes ranging from the micrometer scale to the nanometer scale. For scan sizes smaller than 40 nm × 40 nm, the same area was scanned repeatedly until the effect of tip drift is minimized.

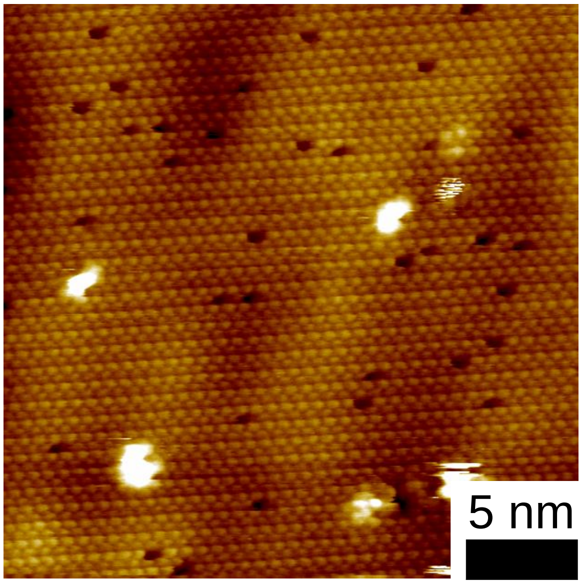

Figure 1. STM image of vacancies in the third molecular layer of pentacene on styrene/Si (001).

The STM image of the third molecular layer of pentacene in Fig. 1 shows individual molecules and vacancies. Vacancies appear as low areas in the rows of molecules. One molecule is missing in a single vacancy. Vacancies are observed in both high and low rows of molecules. We found that vacancies exist in all of the molecular layers of a five-molecular layer thick pentacene thin film.

Pentacene thin films on styrene/Si (001) are imaged most clearly with a bias voltage of -3 V and a tunneling current of 300 pA. There is no change in STM images for voltages ranging from -3.5 V to -2.2 V and tunneling currents from 200 pA to 100 pA, indicating that the structural features observed in STM images do not change with different tunneling conditions.

4.3 Concentration of vacancies

The total concentration of vacancies was calculated using thermodynamic and kinetic predictions. The equilibrium concentration of vacancies in organic crystals can be calculated using the thermodynamic parameters such as the energy and the entropy of vacancy formation [7, 9]. Previous studies have predicted, however, that in molecular crystals, the kinetics of crystal growth is the major factor that determines the non-equilibrium concentration of vacancies in bulk [10]. The concentration of vacancies in pentacene on styrene/Si (001) was measured to determine whether kinetics or thermodynamics govern the concentration of vacancies in a pentacene thin film.

4.3.1 Thermodynamic concentration of vacancies in pentacene

The equilibrium concentration of vacancies can be calculated as a function of temperature if the vacancy formation energy is known. The equilibrium concentration of vacancies in bulk pentacene is given by [7]

$$n_v / N_0 = exp(S_v / k_B) exp(-E_v / kT), \tag{1}$$

where n_v is the concentration of vacancies, N_0 is the number of molecules per unit volume, k_B is the Boltzmann constant and T is the temperature. S_v and E_v are the entropy of vacancy formation and the energy of vacancy formation, respectively.

In calculations using a many-molecule supercell, E_v can be found by comparing the total energies of systems with and without a vacancy.

$$E_v = E_{defect} - \frac{n-1}{n} E_{perfect} \tag{2}$$

E_{defect} is the energy of a supercell with one vacancy and n-1 molecules and $E_{perfect}$ is the energy of the perfect crystal with n molecules [9].

The estimates of S_v and E_v obtained from the simulation for pentacene at 300 K are 0.0037 eV/K and 1.7 eV, respectively [9]. Plugging the values of S_v and E_v into equation (1), we obtain the equilibrium concentration of vacancy of 10^{11}cm^{-3} in bulk pentacene. The fractional concentration of vacancies, n_v/N_0, is 10^{-10}. The low concentration of thermally activated vacancies is expected because E_v is much larger than $k_B T$.

4.3.2 Kinetically controlled concentration of vacancies

The concentration of vacancies in thermal equilibrium calculated from equation (1) is true only if a crystal grows slowly. In a crystal growing at the melting temperature at a rate exceeding 10^{-7}m/s, the concentration of vacancies are controlled by kinetics [10].

The non-equilibrium concentration of vacancies formed at a growing (001) surface controlled by kinetics is given by

$$n_v / N_0 = D \exp(-U / k_B T) \tag{3}$$

where the pre-exponential term D is a factor measuring the probability that an approaching molecule reaches a lattice site at which it may be built into the lattice above a vacant site [10]. The statistical factor, D of a molecule approaching the surface is 1/30. T is the temperature at which the crystal is formed.

The lattice energy, U is defined as the intermolecular potential of two molecules separated by one lattice spacing in the (001) plane [10]. For anthracene, the lattice energies in the (001), (010) and (100) planes are 4.8 kJ/mol, 17.9 kJ/mol, and 19.7 kJ/mol, respectively. The concentration of vacancies calculated from the mean lattice energy of three different planes is 4.8×10^{-3} at 300 K [10]. The higher non-equilibrium concentration than the thermodynamic concentration of vacancies is not surprising because the value of exp ($-U/k_B T$) is much smaller than exp ($-E_v/k_B T$) since the vacancy formation energy E_v is 1.7 eV in equilibrium, but the energy U in non-equilibrium is 10^{-2} eV/mol.

4.3.3 Concentration of vacancies in pentacene thin films

The number of single vacancies was counted in the second, the third, and the fourth molecular layers of a pentacene thin film. In the second molecular layer, there are 85 single vacancies within an area of 40 nm × 40 nm. Since there are two molecules in the unit cell, 5120 molecules will occupy the lattice sites of 2560 unit cells in the same area. The fraction of single vacancies occupying the pentacene lattice sites in the second molecular layer is thus 1.6%. Similarly, 36 molecules are absent from 2232 lattice sites giving 1.6% of single vacancies in the third molecular layer. In the fourth molecular layer, molecules occupy 6600 molecular sites in an area of 25 nm × 25 nm and 88 sites are vacant in the same area. The fraction of single vacancies in the fourth molecular layer is 1.3%. The mean fraction of single vacancies overall, considering all of the molecular layers, is 1.5%.

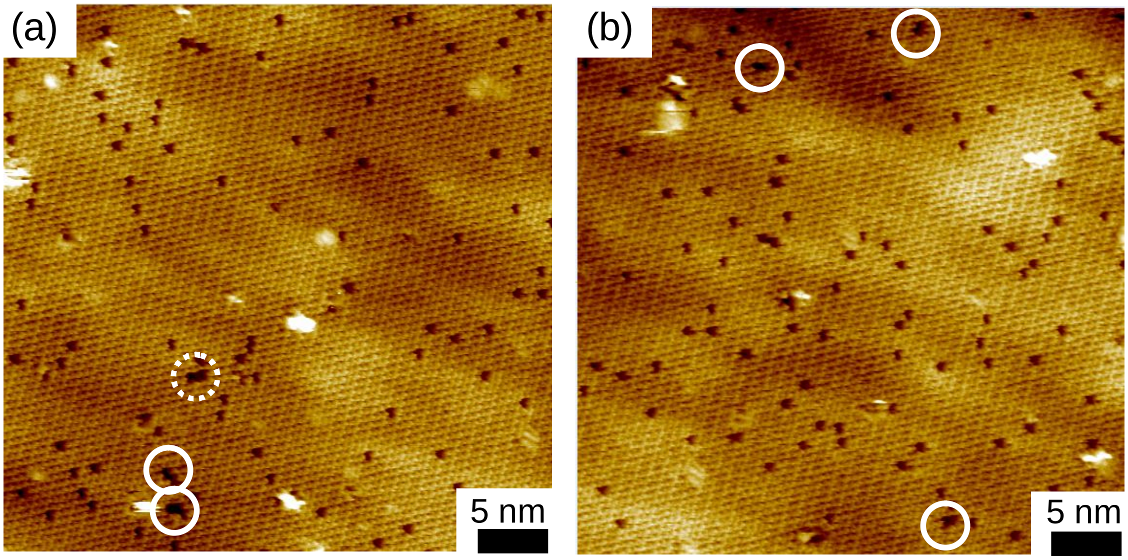

Figure 2. Two different areas in the second molecular layer of pentacene on styrene/Si (001) showing (a) 2 divacancies and a trivacancy and (c) 3 divacancies. Divacancies and a trivacancy are marked with solid circles and a dashed circle, respectively.

In addition to single vacancies, in which a single molecule is missing, divacancies and trivacancies are also found in pentacene thin films. Divacancies are created when two single vacancies are next to each other. Trivacancies are formed with three single vacancies clustered together as shown in Fig. 2(a). The probability of forming a trivacancy is so small that only one trivacancy was observed in a large scan size of 100 nm × 100 nm.

In Fig. 2(b), divacancies occupy 3 of 5120 lattice sites in an area of 40 nm × 40 nm. Since there are 85 single vacancies in the same area, the fraction of the number of divacancies to the number of single vacancies is 3.5%.

We used statistical arguments to estimate the probability of finding two single vacancies next to each other. Here $P_{vacancy}$ and $P_{divacancy}$ are defined as the probability of finding single vacant sites and the probability of finding two vacant sites adjacent to each other, respectively. The probability for finding two single vacancies next to each other is equal to the square of the probability of finding single vacant site.

$$P_{divacancy} = (P_{vacancy})^2 \tag{4}$$

$$P_{vacancy} = \frac{N_{vacancy}}{N_{sites}} = \frac{85}{5120} = 1.66 \times 10^{-2}, \tag{5}$$

$$(P_{vacancy})^2 = 2.76 \times 10^{-4}, \tag{6}$$

$$P_{divacancy} = \frac{N_{divacancy}}{N_{sites}} = \frac{3}{5120} = 5.86 \times 10^{-4}, \tag{7}$$

where $N_{vacancy}$ is the number of single vacancies, $N_{divacancy}$ is the number of divacancies and N_{sites} is the number of total sites. The difference between $P_{divacancy}$ and $(P_{vacancy})^2$ can be explained by counting statics associated with the small number of divacancies. The fractional uncertainty given by $N_{divacancy}^{-1/2}$ was 50%. The small fraction of divacancies measured in the STM image is reasonable within this uncertainty.

We can use the fraction of the sites occupied by single vacancies to calculate the concentration of vacancies in pentacene thin films. The bulk number density of pentacene molecules is 2.5 molecules/nm^3, giving a value of 2.5×10^{21} cm^{-3}. Since the mean fraction of the single vacancies in a pentacene film is 1.5%, the total concentration of vacancies in a pentacene film is approximately 10^{19} cm^{-3} under an assumption that the number of vacancies in each molecular layer is approximately the same. In comparison to the equilibrium concentration of vacancies of 10^{11} cm^{-3}, calculated for bulk pentacene, the concentration of vacancies in a pentacene thin film is much higher. In addition, the observed concentration of vacancies in pentacene is four to five magnitude of orders larger than the calculated equilibrium concentration of vacancies in naphthalene and anthracene, 10^{14} - 10^{15} cm^{-3} [7]. The concentrations of vacancies are summarized in Table 1.

Thermodynamic concentration of vacancies in bulk pentacene	**Kinetically controlled concentration of vacancies in bulk anthracene**	**Total concentration of vacancies in a pentacene thin film**
10^{-10}	10^{-3}	10^{-2}

Table 1. The calculated and measured concentration of vacancies

The total concentration of vacancies in a pentacene thin film is close to the kinetically controlled concentration of vacancies, 10^{-3}. Our results indicate that the concentration of vacancies in a pentacene thin film is not determined by thermodynamic equilibrium. Instead the concentration of vacancies is set by the growth process of a crystal. The concentration of vacancies in non-equilibrium can be controlled by changing the kinetic parameters in equation (3) such as temperature and the deposition rate which can influence the value of *D*. The vacancy concentration may provide an important and unknown mechanism for impacting the electronic properties of pentacene thin films.

4.4 Vacancies in two molecular basis sites

We performed a statistical study involving a large number of vacancies in order to determine whether vacancies are formed preferentially on either molecular site within the unit cell. The two molecular sites were treated equivalently in the predictions in section 4.3 for the concentration of vacancies in the kinetic model [10]. It is not yet known whether the energy *U* in equation (3) have different values for the two crystallographic basis sites.

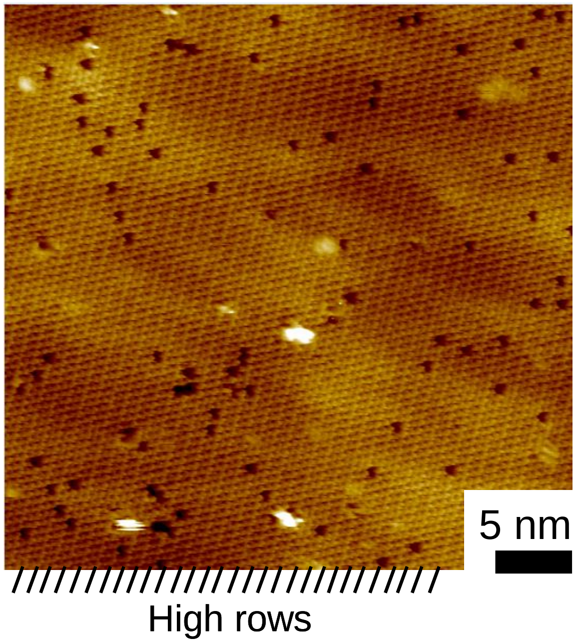

Figure 3. STM image of the second molecular layer of a pentacene thin film on styrene/Si (001). Rows of molecules in high molecular basis sites are schematically drawn in the bottom of the image.

If the values of U for the two inequivalent sites differed by energy on the order of k_BT or more, there would be a large difference in the vacancy populations. In order to test this idea, the number of single vacancies in high and low rows was counted in the STM images of pentacene on styrene/Si (001). The size of the STM images ranged from 25 nm × 25 nm to 50 nm × 50 nm. There are 36 vacancies in an area of 25 nm × 25 nm in which vacancies occupy 18 molecular sites in high rows. The same number of vacancies was found in low rows.

In a larger scan area of 36 nm × 40 nm as shown in Fig. 3, the number of vacancies in high molecular sites is 34 out of a total number of 76 vacancies. The largest STM image used here is 50 nm × 48 nm. This image size forms a practical upper limit because we found that high and low rows are not distinguishable in STM images bigger than 50 nm × 50 nm. In the image size of 50 nm × 48 nm, the distinction between high and low rows was made from the comparison between a larger view of the STM image and the sectional profile. Rows of molecules in high molecular basis sites are marked with solid lines in Fig. 3.

Image number	**STM image size**	**Total number of vacancies**	**Number of vacancies in high rows**	**Number of vacancies in low rows**	**Fraction of vacancies in high rows**
1	25 nm × 25 nm	36	18	18	0.50
2	25 nm × 25 nm	33	16	17	0.49
3	36 nm × 40 nm	76	34	42	0.45
4	37 nm × 40 nm	94	41	53	0.44
5	50 nm × 48 nm	143	74	67	0.52

Table 2. The number of vacancies found in high and low rows in STM images.

A summary of the number of vacancies in high and low molecular basis sites is shown in Table 2. The fraction of vacancies in high rows to the total number of vacancies ranges from 0.44 to 0.52 in the last column. The mean fractions of vacancies found in high and low rows are 0.48 and 0.52, respectively. The uncertainty from counting statistics is sufficient to account for the difference between the fractions in Table 2. The probability to find vacancies in high and low rows is equal within the uncertainty.

The results in Table 2 show that vacancies are not energetically driven to either of the two molecular basis sites and the defect formation energies for the two sites are equal within limits of the statistical measurement.

4.5 Structural distortion near vacancies in pentacene

The displacements of molecules near a vacancy can be measured using STM images and then compared with theoretical predictions. We used high-resolution STM images of pentacene thin films on styrene/Si (001) to measure the displacements of molecules from their ideal lattice sites near vacancies. We define the *apparent displacement* of a molecule as the distance between the position of the visible end of the molecules in an STM image and the lattice point that it would occupy in a perfect crystal. An STM image was used to obtain molecular positions and an ideal grid of lattice points in Fig. 4.

The coordinates for the positions of molecules obtained from the center of each molecule in the STM image. The x and y axes for the coordinates were defined as the same x and y axes of the STM image. The coordinates for the lattice sites are obtained using the intersections of two lines generated from the best fits of average molecular positions along the rows. The displacements of molecules were measured by taking the difference between the coordinates of

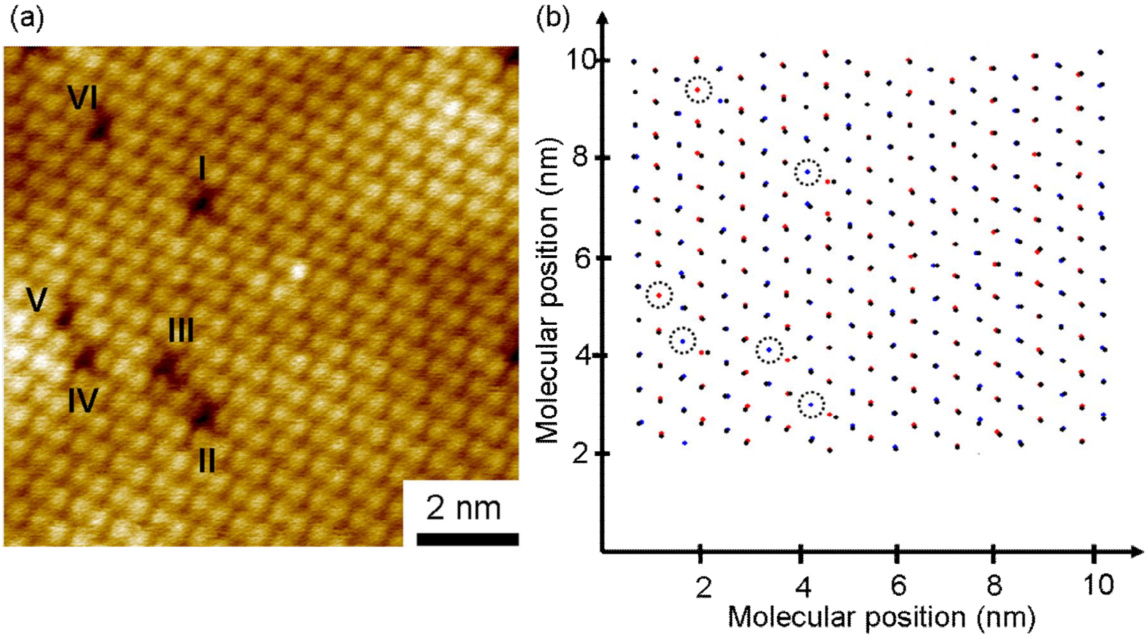

Figure 4. (a) STM image of pentacene on styrene/Si (001). The six vacancies are numbered from I to VI in the image. (b) Position of molecules and ideal lattice points generated from the STM image in (a). The six vacancies are marked with circles in (b).

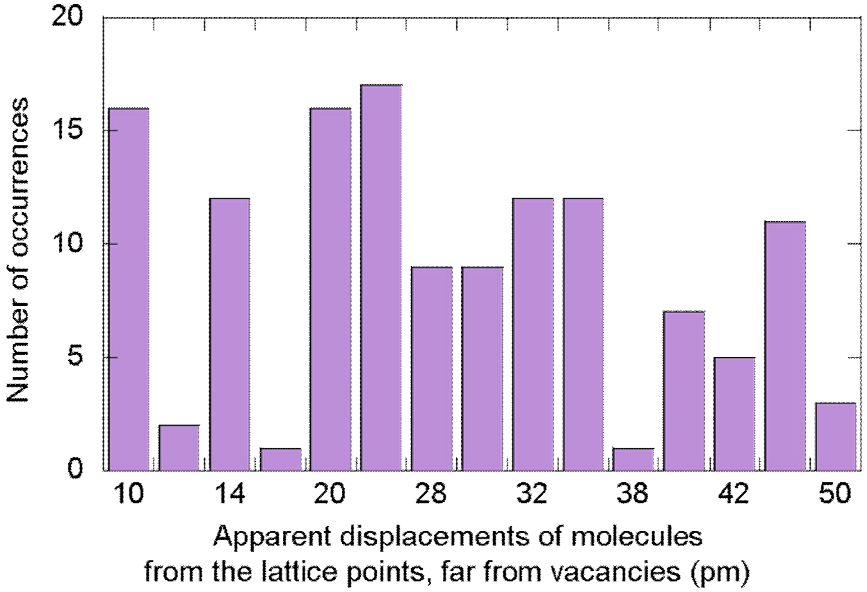

Figure 5. Histogram of the distance between observed molecular positions at sites far from vacancies and the grid of ideal lattice sites.

each molecule and the nearest lattice point. The distance between a molecule at (x_1, y_1) and a lattice point of a perfect grid at (x_2, y_2) is $[(x_1\text{-}x_2)^2 + (y_1\text{-}y_2)^2]^{1/2}$. Four vacancies labeled as I, II, III and IV in Fig. 4 are formed in low molecular basis sites and two vacancies labeled as V and VI are formed in high molecular basis sites. The distance between the molecular positions and the grid of ideal lattice sites far from vacancies had a root-mean-square value of 31 pm in Fig. 5. This value provides an estimate of the accuracy with which the lattice points were assigned. The

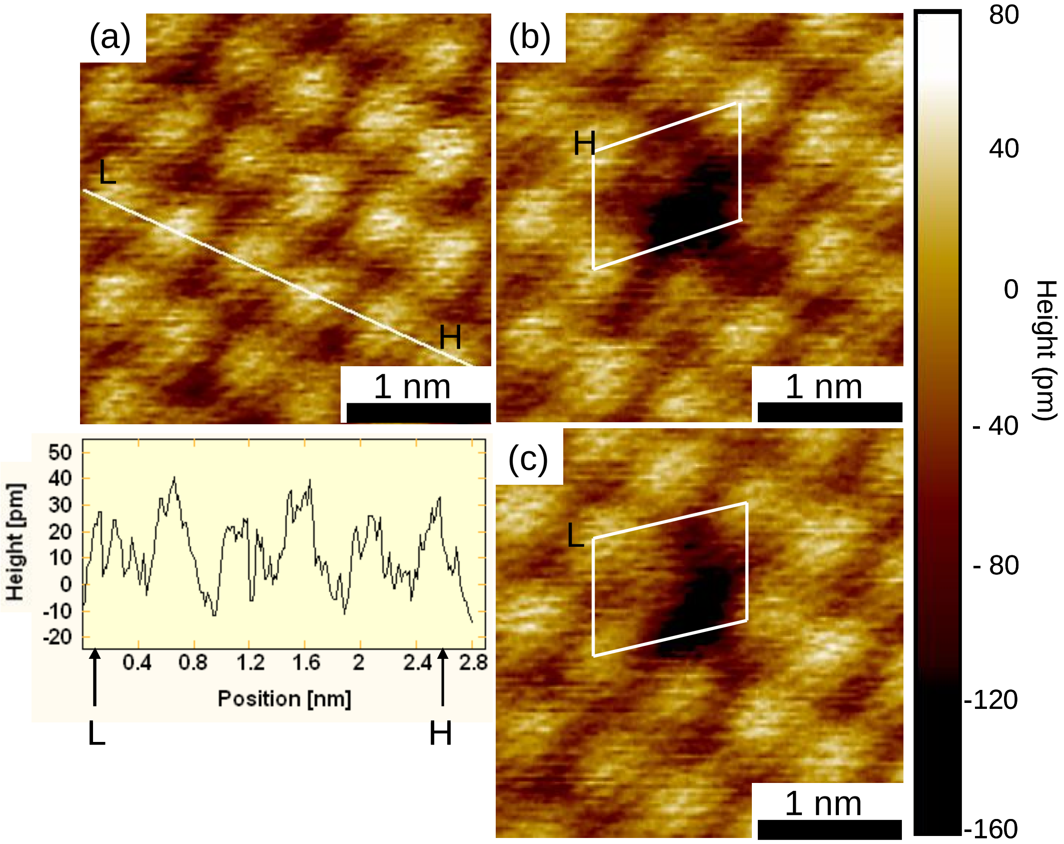

Figure 6. (a) STM image and the corresponding sectional profile of high and low molecules. STM images of a vacancy formed (b) in a low row and (c) in a high row. The pentacene unit cell is schematically drawn in (b) and (c). High and low molecules are labels as 'H' and 'L'.

apparent displacements of six neighboring molecules adjacent to each vacancy in high and low molecular basis sites were measured in the STM image. Fig. 6(b) and (c) are larger views of vacancy I and VI shown in Fig. 4 (a), respectively.

The pentacene unit cell is schematically drawn over molecules in the STM images. A vacancy formed in a low basis site is surrounded by high molecules in Fig. 6 (b). A vacancy formed in high basis site is shown in Fig. 6(c).

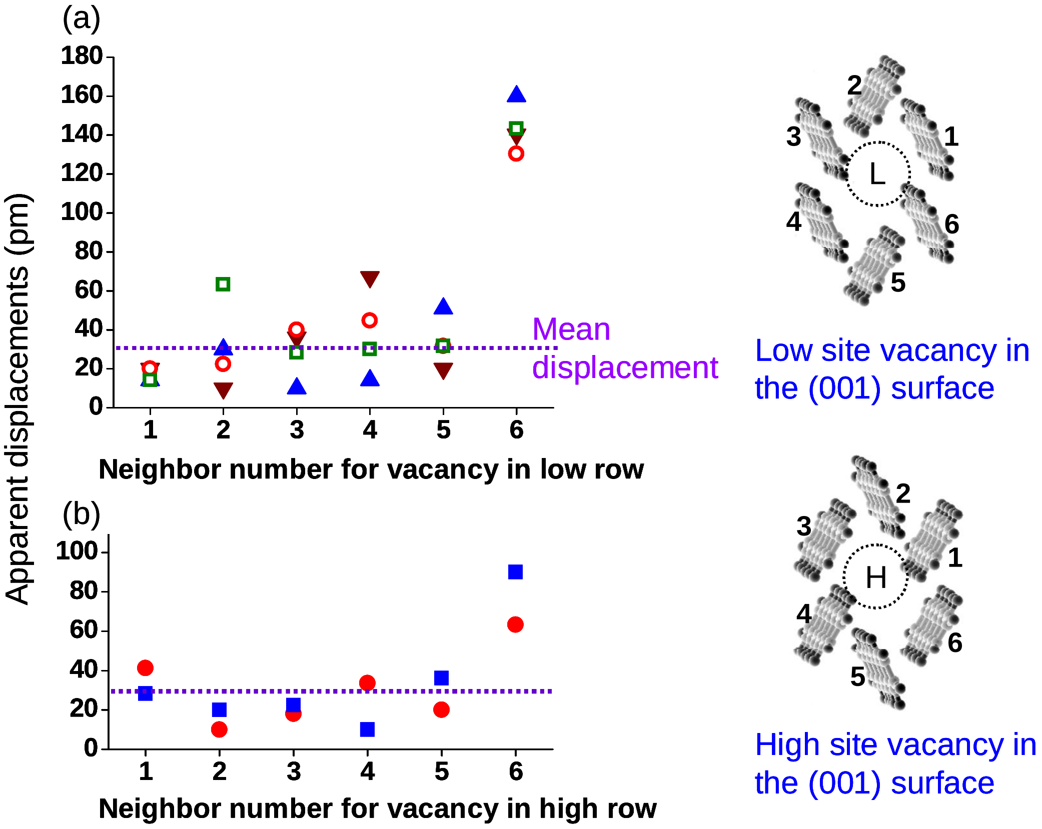

Figure 7. (a) The apparent displacements of the molecules near vacancies from their lattice sites in the (001) surface for (a) four vacancies in low rows and (b) two vacancies in high rows. The positions of the molecules numbered from one to six with respect to the vacancies are given in the bulk model of pentacene.

The apparent displacements of molecules from their lattice sites near vacancies are shown in Fig. 7. For molecules near vacancies both in high and low rows, only one of the six nearest neighbors to a vacancy is displaced far more than other molecules. For vacancies in low rows, the largest displacement occurs with the molecule #6. The apparent displacements of molecule #6 near vacancies I, II, III and IV are 160 pm, 145 pm, 140 pm and 130 pm. Similarly, molecule #6 adjacent to vacancies in the high rows are displaced by 60 pm and 90 pm in vacancies V and VI, respectively. Although the apparent displacements near vacancies in high rows are not as large as the apparent displacements of molecules next to vacancies in low rows, they are large enough to be distinguished from the remaining molecules. The mean displacement of the molecules far from vacancies is shown by the dashed line in Fig. 7.

The direction and the magnitude of the displacement of molecules relative to the lattice sites are plotted in Fig. 8. For a lattice point at (x_1, y_1) and a molecule at (x_2, y_2), the position of a molecule relative to a lattice site is (Δx, Δy) where $\Delta x = x_2 - x_1$ and $\Delta y = y_2 - y_1$. Figure 8 provides a map of what direction and how far molecules are displaced from the lattice sites. Molecule #6 next to each vacancy in high and lows are marked with the circles and the triangles. The apparent displacements of remaining molecules away from vacancies, indicated as dots, appear in random directions. The largest displacements of molecules around vacancies in high and low rows occur in one direction which coincides with the x axis of the STM image.

In order to examine whether molecules near vacancies are displaced as well as rotated or tilted with respect to their principal crystallographic axes, the height difference between the molecules with the largest displacements and their neighbors in low rows was measured. Changes in both center-of-mass and orientation of molecules could shift apparent lateral positions of molecules. Since the STM tip images the exposed end of molecules, the apparent displacements of molecules in an STM image do not necessarily mean that the molecules have been displaced.

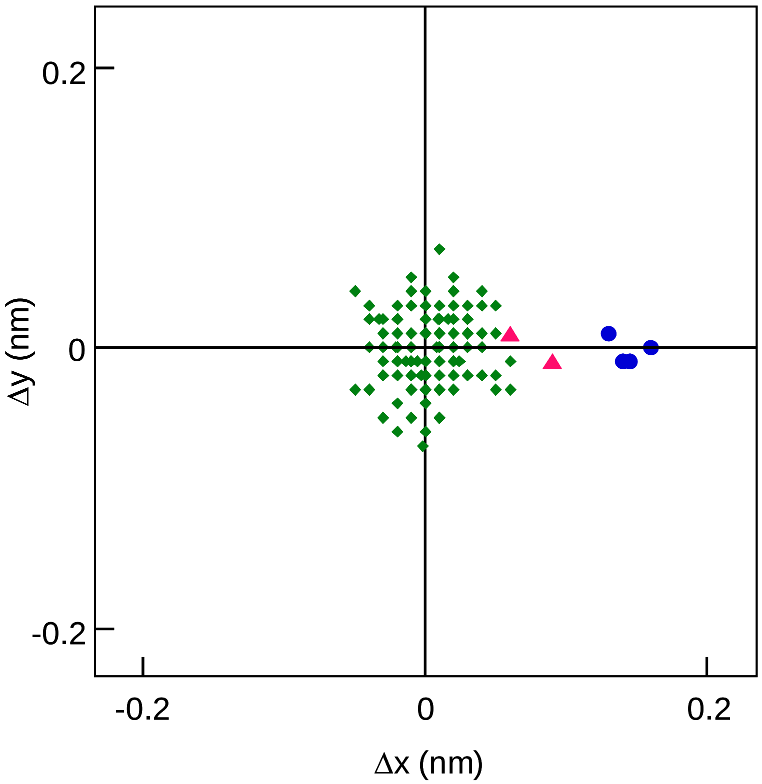

Figure 8. The direction and the magnitude of displacement of molecules near a vacancy. The circles and triangles indicate molecules with the largest displacements around a vacancy in the low and high molecular sites, respectively.

The height measurements in the STM image show that the molecules with the largest displacements near vacancies are lower than their neighbors by 25 pm. This difference is much lager than the 2.5 pm standard deviation in height measured for a set of random pairs of high and low molecules adjacent to each other.

The tilt angle needed to move the top of a molecule down by 25 pm was calculated based on the model depicted in Fig. 9. A molecule is tilted by additional angle θ with respect to the surface normal along the *z* axis, which leads to lowering the height of the molecule by 25 pm and moving the molecule laterally by α. The values of α and θ are calculated for two inequilvalent molecules in the unit cell. One of the two molecules is tilted with respect to the surface normal by 20.3° as shown in Fig. 9(a). To lower the exposed end of the molecule by 25 pm, an additional tilting angle θ required is calculated from equation (9).

$$0.8\ nm \times cos(20.3^\circ) - 0.025\ nm = 0.8\ nm \times cos(20.3^\circ + \theta) \tag{8}$$

By solving for θ, we obtain 4.6°. Similarly, the other molecule tilted by 22.2° with respect to the surface normal in the unit cell needs to tilt by additional 4.4° to lower its top end by 25 pm. The mean tilt angle is 4.5°.

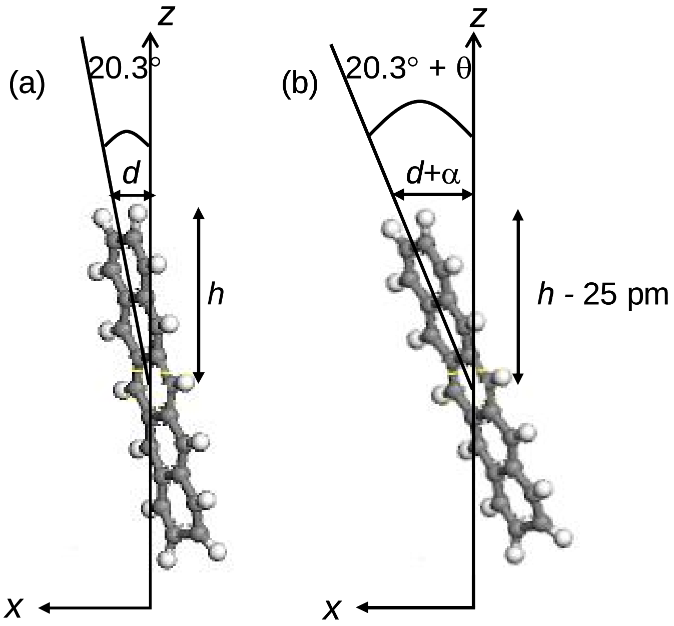

Figure 9. Model of a tilted molecule with respect to the surface normal describing the lateral shift and a change in height of the top of a molecule.

The lateral shift of a molecule, α, results from the increase in the molecular tilt angle is obtained by

$$0.8\ nm \times sin(20.3^\circ) = 0.8\ nm \times sin(20.3^\circ + 4.6^\circ) - \alpha \tag{9}$$

$$0.8\ nm \times sin(22.2^\circ) = 0.8\ nm \times sin(22.2^\circ + 4.4^\circ) - \alpha \tag{10}$$

The mean lateral shift from the values of for two molecules in the unit cell α in equations (10) and (11) is 55 pm. Therefore, the height difference comes from a change in tilting angle of 4.5°, which corresponds to shifting molecules laterally by 55 pm and downward by 25 pm. The lateral shift of 55 pm is only one third of the largest observed apparent displacement of 150 pm, leading to the conclusion that both a lateral shift and a rotation of molecules contribute to displacements of molecules observed in the STM images.

4.6 Conclusion

The large displacements of molecules near vacancies in pentacene thin films are inconsistent with the expectation of small displacements predicted in similar polyacene crystals. The apparent displacements of molecules we observed near vacancies may affect the predictions of the electronic states associated with defects as calculations have neglected the structural distortion of the crystalline lattice sites around a vacancy [4, 8].

4.7 References

[1] I. Eisenstein and R. W. Munn, Chem. Phys. Lett. **77**, 47 (1983).

[2] D. Tsiaousis and R. W. Munn, J. Chem. Phys. **117**, 1833 (2002).

[3] E. A. Silinsh, I. J. Muzikante, A. J. Rampans, and L. F. Taure, Chem. Phys. Lett. **105**, 617 (1984).

[4] D. P. Craig, B. R. Markey, and A. O. Griewank, Chem. Phys. Lett. **62**, 223 (1979).

[5] H. Baessler, G. Hermann, N. Riehl, and G. Vaubel, J. Phys. Chem. Sol. **30**, 1579 (1969).

[6] E. A. Silinsh, Phys. Status Soilidi **3**, 817 (1970).

[7] E. A. Silinsh, *Organic Molecular Crystals: Their Electronic States* (Springer, Berlin, 1980).

[8] I. Okada, M. Sugawara, and K. Kojima, J. Phys.:Condens. Matter **1**, 3555 (1989).

[9] L. F. Drummy, C. Kubel, and D. C. Martin, Philos. Mag. **84**, 1955 (2004).

[10] D. P. Craig, J. F. Ogilvie, and P. A. Reynolds, J. Chem. Soc. Faraday Trans. II **72**, 1603 (1976).

Chapter 5

Extended Defects in Pentacene Thin Films

* The content of this chapter has been published as *Journal of Applied Physics* ***106****, 103521 (2009).*

5.1 Introduction

Extended structural defects such as dislocations, grain boundaries and stacking faults are formed during the growth of polycrystalline organic thin films. Structural defects are intrinsic to film or crystal growth processes and affect the crystalline structure of semiconductor films or single crystals [1-3]. More importantly, structural defects influence the electrical characteristics of organic electronic devices [4-6]. The hole mobility observed in organic thin film transistors (OFETs), ranging approximately from 0.3 to 1.5 $cm^2V^{-1}s^{-1}$ [7-9], is far lower than the mobility in single crystal devices. Among OFETs, the highest mobility of 20 $cm^2\ V^{-1}\ s^{-1}$ is found in a device fabricated using a single crystal [10]. The lower mobility in devices fabricated using organic semiconductor thin films is often attributed to grain boundaries. Grain boundaries at the junctions of islands disrupt charge transport at the highest misorientation angle between grains [11]. High angle grain boundaries cause decrease in the magnitude of photocurrent in bicrystals [12]. Conducting probe atomic force microscopy studies found that the electrical resistance significantly increased across a single grain boundary in sexithiophene crystals [13].

The importance of the structure and the concentration of extended defects in organic thin films has lead to extensive structural characterization of organic crystals [14-16]. Extended defects can be probed using both microscopy and diffraction techniques. A broadening of Bragg reflections in x-ray scattering measurements has indirectly indicated the presence of dislocations in pentacene [2]. AFM images exhibited screw dislocations in pentacene thin films in which the concentration of dislocations was estimated by averaging over a large area [2].

The present understanding of the structure and electronic properties of extended defects in organic thin films lacks molecular-scale structural information. Attempts made to understand microscopic charge transport in organic materials have relied on theoretical models [17, 18]. The energy levels for a hole have been calculated on a microscopic scale for a variety of idealized pentacene grain boundary cases [17]. The grain boundary model for polymer thin-film transistors has shown that charge transport depends on the relative orientations of two grains forming a grain boundary [18]. Interpreting and testing these charge transport models require molecular resolution imaging because the structures described in the model models are based on the arrangement of molecules near the defects.

We have used STM to perform molecular-scale structural studies of extended defects in pentacene thin films. Real-space images of defects at molecular scale allow us to image individual defects and to determine the orientation of grains. Three types of extended defects were observed in pentacene thin films grown on Si (001) modified with styrene. Tapping mode AFM images of pentacene grown on oxidized Si (001) were also used to probe how the nucleation and the growth of pentacene islands leads to the formation of structural defects.

5.2 Tilt grain boundaries between islands

Tilt grain boundaries in pentacene thin film are formed at the interfaces between two grains that have previously been nucleated independently. The schematic in Fig. 1(a) shows an arbitrary example of a tilt grain boundary formed at the junctions between grains. The crystallographic axes of two grains are illustrated as [100] and [010]. The dashed line represents the location of a grain boundary. The crystallographic orientations of two grains are related by a rotation around the axis normal to the surface [19].

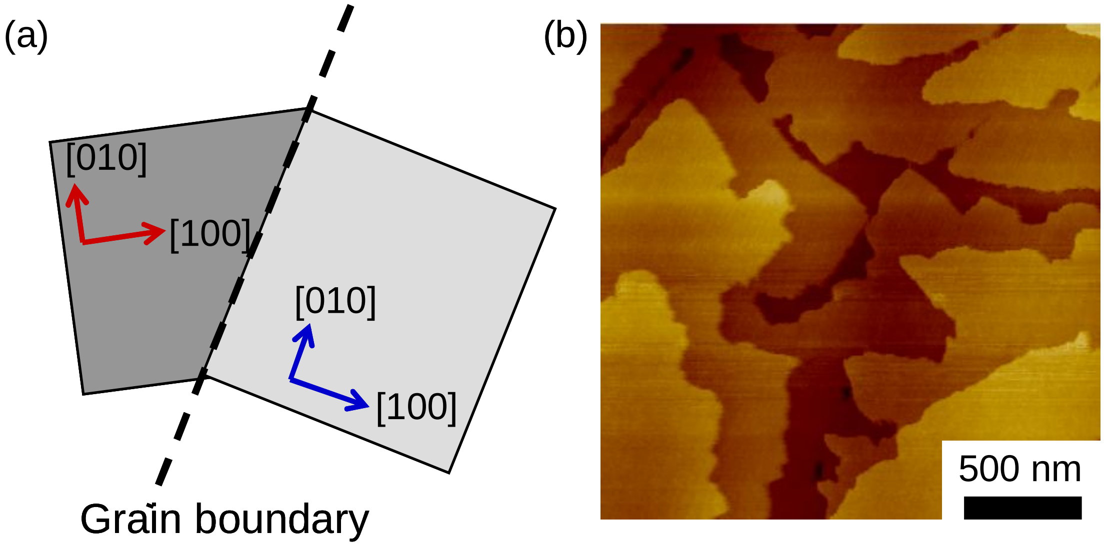

Figure 1. (a) Schematic of a tilt grain boundary between two islands. (b) STM image of a pentacene thin film on styrene-modified Si (001).

Grain boundaries formed between the first-layer islands have been previously studied on pentacene on SiO_2. Pentacene crystals nucleate during the growth of pentacene thin films with no preferred in-plane orientations in the first molecular layer [20]. Grain boundaries form as a result of coalescence of islands in the first layer as pentacene reaches the surface. Kalihari *et al.* found in the grain orientation maps using the transverse shear microscopy (TSM) that approximately 90% of grain boundaries within the first layer of a pentacene thin film on SiO_2 are high angle greater than 15° [20].

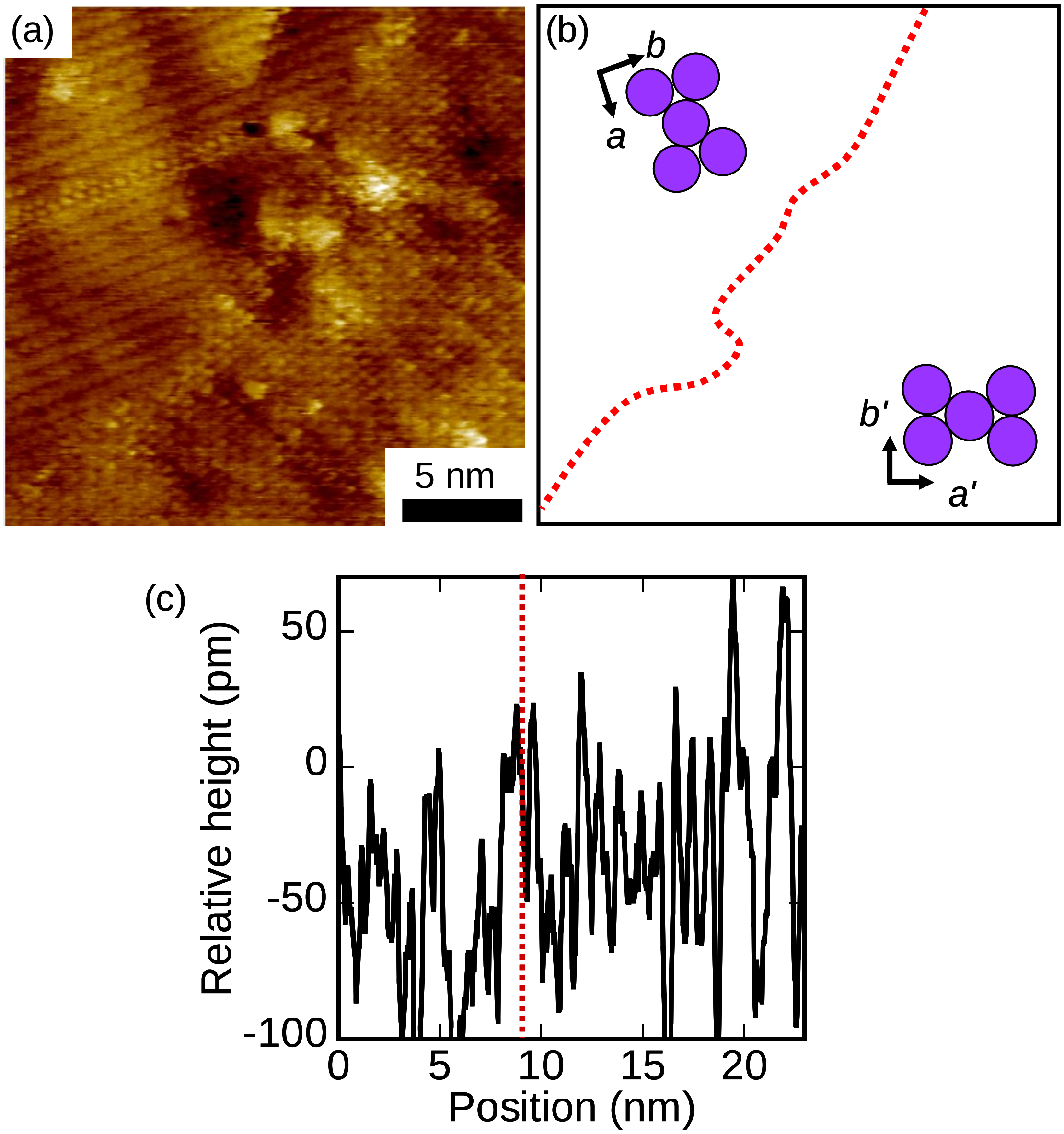

Figure 2. (a) STM image of a tilt grain boundary at the junction between two pentacene islands. (b) Schematic of the tilt grain boundary in the STM image. The basis vectors of the pentacene unit cell are represented as *a* and *b* for the left grain and *a′* and *b′* for the right grain. (c) Height as a function of position along a line across the grain boundary. The dashed line indicates the location of the grain boundary.

In order to study the structure of grain boundaries formed between two grains, STM was used to image the junction between pentacene islands on styrene/Si (001). A large-scale STM image of two islands in a five-molecular layer thick pentacene thin film is shown in Fig. 1(b). These islands were nucleated after the first layer is complete. Faceted islands of pentacene form steps along the $(1\bar{1}0)$ and (110) orientations, which have the lowest free energy per unit length [21].

An STM image of a tilt grain boundary was acquired near the lower part of Fig. 1(b). The difference in the direction of molecular rows in each grain in Fig. 2(a) indicates that the crystallographic orientations of two islands are different. The in-plane orientations of the pentacene unit cell in each grain were determined using the STM image. The two basis vectors for each grain, a and b or a' and b' in Fig. 2(b) form 90 ± 2°. The schematic shows the relationship between the crystallographic orientations of two islands. The misorientation angle between two islands measured from the STM image is 67 ± 2°, forming a high-angle grain boundary. The sectional profile in Fig. 2(c) shows that the grain boundary is formed between pentacene molecular layers at the same height above the substrate.

The grain boundary does not have a single crystallographic direction with respect to the pentacene lattice as illustrated in Fig. 2(b). Several segments of the grain boundary are planar facets with a (110)-type planar orientation with respect to the grain on the left side of the grain boundary. The calculations of energies of steps on the (001) surface of pentacene have predicted that the (110) oriented steps have low energies [21]. Segments of a tilt grain boundary are faceted along the low-energy crystallographic direction.

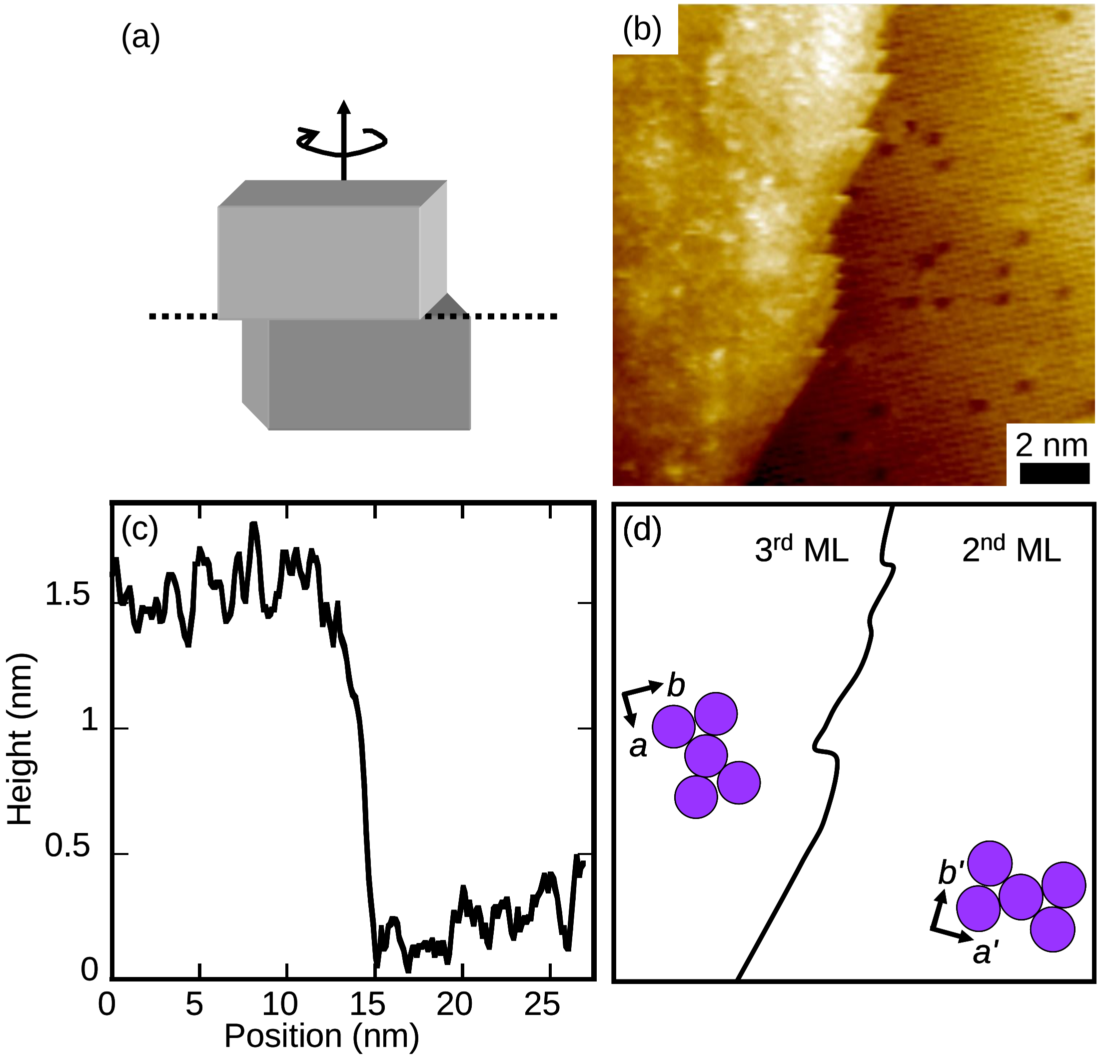

Figure 3. (a) Schematic of a twist grain boundary formed between molecular layers. (b) STM image of the second and the third molecular layers in one island of pentacene on styrene/Si (001). A twist grain boundary is located between the second and the third molecular layers. (c) Cross section of the STM image. (d) Schematic representation of the twist grain boundary in the STM image. The directions of the pentacene unit cell in each molecular layer are represented using the basis vectors *a*, *b*, *a'*, and *b'*.

The effect of grain boundaries on the electronic properties of pentacene thin films has been modeled using calculations for charge-quadrupole interaction energy [17]. The calculations associated with the electronic state distribution near a grain boundary have shown that grain boundaries formed on (110) planes act as trapping centers for holes in pentacene [17].

5.3 Twist grain boundaries between molecular layers

Twist grain boundaries are a second type of grain boundary formed between molecular layers of pentacene thin films. Twist grain boundaries occur along {001} planes. The molecular layers on either side of the grain boundary are rotated around an axis normal to the {001} planes, as shown in Fig. 3(a). A grain boundary formed by rotation of molecular layers around a vector normal to {001} planes is structurally favorable because the {001} planes have the lowest surface energy of all pentacene facets [21].

We used STM to find twist grain boundaries in pentacene thin films grown on styrene/Si (001). A series of STM images were acquired in molecular layers of a pentacene island exposing the (001) surface. Twist grain boundaries between molecular layers were identified by comparing the in-plane orientations of each molecular layer of a pentacene island. The in-plane orientation was determined from the direction of the pentacene crystal lattice in the STM image.

Figure 3(b) shows an STM image of the second and the third molecular layers of a pentacene thin film. The corresponding cross section in Fig. 3(c) shows that the two molecular layers in the image are separated by a thickness of one pentacene molecule. The schematic representation in Fig. 3(d) depicts the in-plane orientations of the pentacene unit cell in the second and the third molecular layers. The difference in in-plane orientations of the pentacene unit cell indicates that a twist grain boundary has formed between two molecular layers. The third molecular layer is rotated by 57 ± 2° around the surface normal with respect to the second molecular layer.

The in-plane orientations of the molecular layers on top of the third molecular layer were determined using the STM image. Figure 4 shows that the facets of the third, the fourth and the fifth islands are in the same plane. A close examination of the STM image of the second through the fifth molecular layers reveals that the in-plane orientations of the third, the fourth and the fifth molecular layers within this particular pentacene grain are the same.

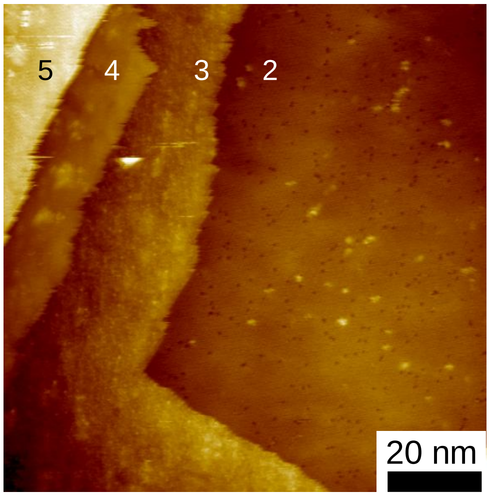

Figure 4. STM image of pentacene grown on styrene/Si (001). The numbers 2, 3, 4 and 5 represent the second, the third, the fourth and the fifth molecular layers in a pentacene island.

There are two mechanisms that could result in twist grain boundaries between molecular layers. One immediately apparent origin of twist grain boundaries is the difference in the sizes of pentacene islands in different molecular layers. Twist grain boundaries can be formed as a result of the overgrowth of small islands by larger islands in the subsequent layer.

A field of small first-layer islands bridged by larger second-layer islands in a pentacene thin film is shown in the AFM image in Fig. 5(a). The pentacene thin film was deposited on an SiO_2 substrate at room temperature, using a different vacuum chamber other than the UHV chamber used for STM studies. The pentacene source in this chamber was heated to 240 °C at a pressure of 10^{-6} Torr to grow the thin film at a deposition rate of 0.17 molecular layers per minute to a total thickness of 1.2 molecular layers. The size of the second-layer islands was up to 1.5 μm wide. The size of the first-layer islands ranges from 300 nm to 1 μm. The second-layer islands overgrow the first-layer islands (Fig. 5(b)).

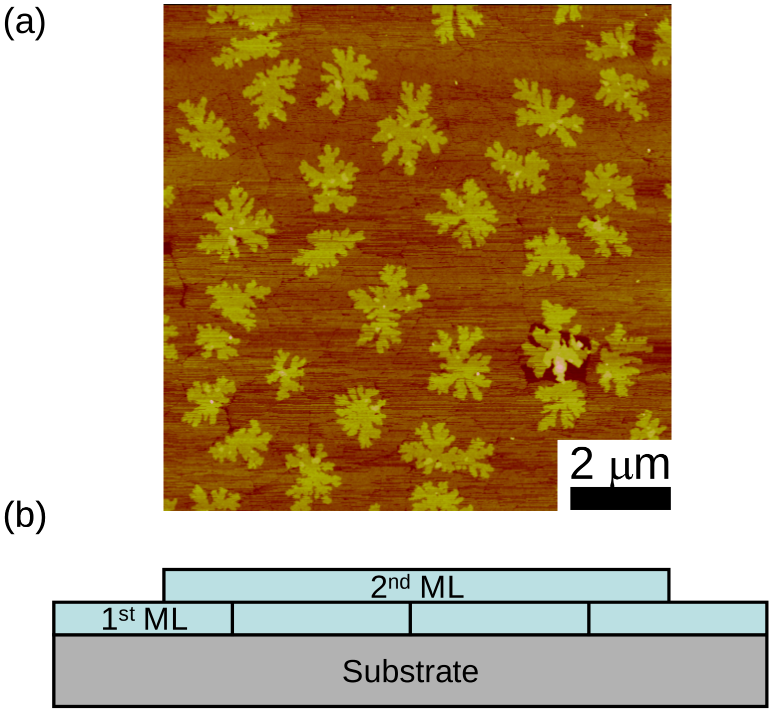

Figure 5. (a) Tapping mode AFM image of a 1.2-molecular layer pentacene thin film grown on oxidized Si (001) at room temperature at a base pressure of 10^{-6} Torr at a deposition rate of 0.17 molecular layers per minute. (b) Schematic of a large second-layer island of pentacene grown across four smaller first-layer islands.

Four islands in the first layer covered by a second-layer island are illustrated in Fig. 5 (b). The second-layer islands grow across the grain boundaries formed between the first-layer islands, which results in twist grain boundaries between the first and the second molecular layers.

A second origin of twist grain boundaries arises from the independent nucleation of molecular overlayers on the lower molecular layers. Local minimia of the energy associated with the formation of the overlayer occur at several rotation angles of the subsequent layer with respect to the layer beneath [22]. Nucleation of the upper layer in one of these minima can effectively rotate the overlayer. The magnitude of the energy depends on the ratio of coinciding to non-coinciding lattice points, which is a measure of the degree of the fit between two lattices. Several possible arrangements of an overlayer on the substrate have been predicted [22]. Kalihari *et al.* have shown in their TSM studies that the majority of third-layer islands grow with commensurate epitaxy and only a few exhibits an orientation of 76° between the second and the third molecular layers [23]. The rotation angle of 57° we measured is not among the predicted angles of 0° or 76° for pentacene. Therefore, the twist grain boundary we observed in the STM image resulted from the overgrowth of larger islands in the subsequent layer rather than independent nucleation of each molecular layer.

5.4 Stacking faults

Stacking faults occur when there is an interruption in the stacking sequence of planes of molecules. We have used STM to look for extended defects within a single island. Figure 6(a) shows an image of the stacking fault taken from a small part of Fig. 2(a). The repeating pattern of high and low rows of molecules is interrupted at the stacking fault. The schematic in Fig. 6(b) shows the strongly faceted stacking fault represented as a dashed line. The bars indicate the arrangements of high and low pentacene molecules near the stacking fault. One molecular sheet in the (100) plane is missing at the stacking fault. Since a low molecular row is deficient, two high rows of molecules are adjacent to each other at the stacking fault.

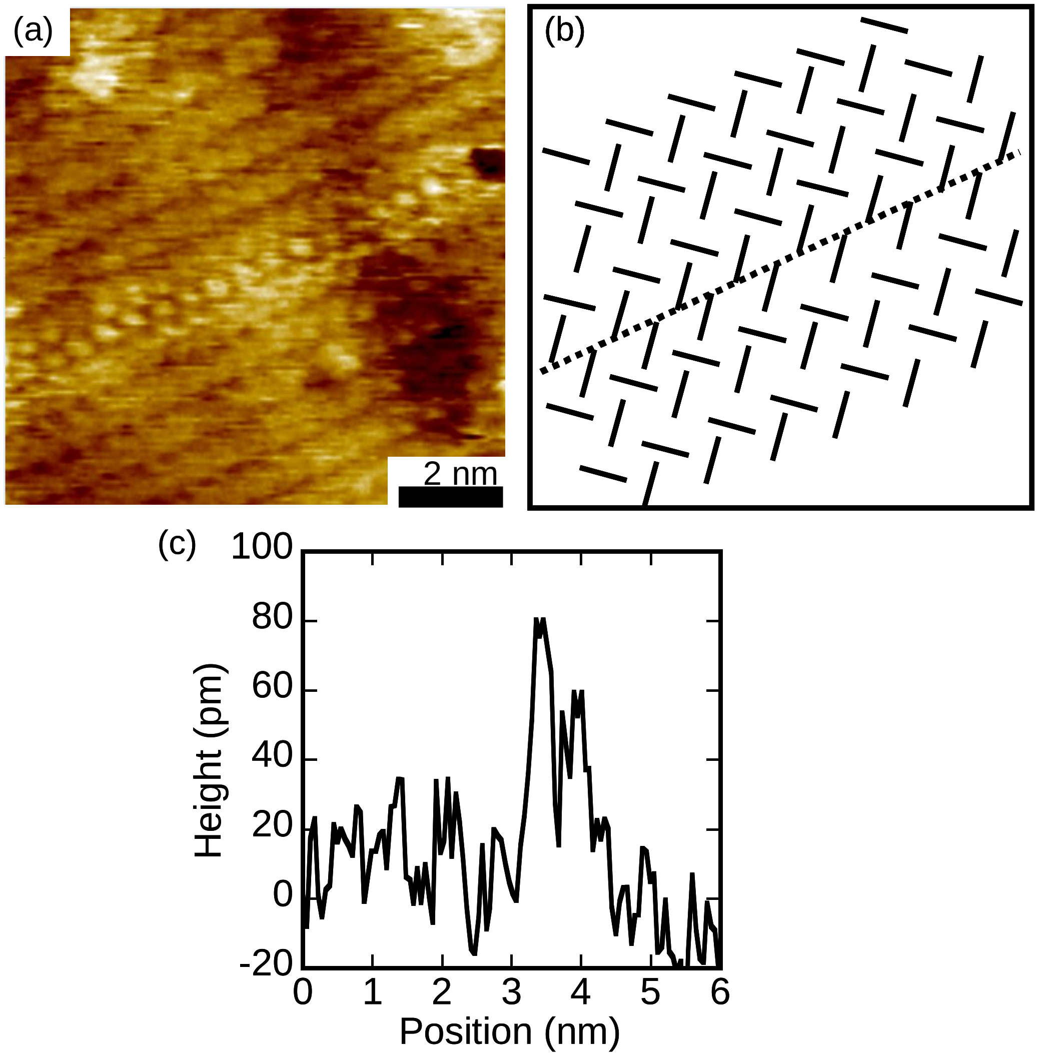

Figure 6. (a) STM image of the stacking fault taken from a part of Fig. 3 (a). (b) Schematic of the stacking fault represented with a dashed line. High and low molecules are indicated with bars. (c) Height of molecules as a function of position along the 6-nm section across the stacking fault.

One row on each side of the stacking fault appears higher than the molecules far from the stacking fault. The cross section in Fig. 6(c) was taken across the stacking fault within an area of 4 nm × 6 nm to measure the apparent height of the molecules near the stacking fault as a function of position. The apparent height difference between molecules next to the stacking fault and their neighbors is 60 pm. Previous studies using STM and calculations have reported that the height of pentacene molecules differing by 50 pm and higher lead to change in the bandwidth of energy level [24].

The effect of the height difference of molecules on the electronic structure of pentacene has been studied using a model of stacked molecules within a structural defect [24]. An increase in the displacement of molecules along the long molecular axis induces hole and electron levels in the energy gap between the highest occupied molecular orbitals (HOMOs) and the lowest unoccupied molecular orbitals (LUMOs), which leads to an increase in the band widths of HOMO and LUMO levels of pentacene [24, 25]. Stacking faults may therefore be associated with trap states in pentacene thin films.

5.5 Conclusion

Three types of extended defects were found in pentacene thin films grown on modified Si (001) surfaces. These extended defects have not been reported for pentacene thin films. A high-resolution study of defects using STM allows us to image and identify grain boundaries using the relative misorientation between crystal lattices. Understanding the molecular-scale structure of defects can be useful to make a link between the structure and the electronic properties of defects by comparing with charge transport models on a microscopic scale. A comparison between the

STM results and electronic states calculations reveals that tilt grain boundaries and stacking faults can contribute to inducing trap states in pentacene thin films [17, 24].

5.6 References

[1] K. Puntambekar, J. Dong, G. Haugstad, and C. D. Frisbie, Adv. Funct. Mater. **16**, 879 (2006).

[2] B. Nickel, R. Barabash, R. Ruiz, N. Koch, A. Kahn, L. C. Feldman, R. F. Haglund, and G. Scoles, Phys. Rev. B **70**, 125401 (2004).

[3] R. Ruiz, D. Choudhary, B. Nickel, T. Toccoli, K.-C. Chang, A. C. Mayer, P. Clancy, J. M. Blakely, R. L. Headrick, S. Iannotta, and G. G. Malliaras, Chem. Mater. **16**, 4497 (2004).

[4] A. Bolognesi, M. Berliocchi, M. Manenti, A. Di Carlo, P. Lugli, K. Lmimouni, and C. Dufour, IEEE Trans. Electron Devices **51**, 1997 (2004).

[5] Y. Y. Lin, D. J. Gundlach, S. F. Nelson, and T. N. Jackson, IEEE Trans. Electron Devices **44**, 1325 (1997).

[6] C. D. Dimitrakopoulos, I. Kymissis, S. Purushothaman, D. A. Neumayer, P. R. Duncombe, and R. B. Laibowitz, Adv. Mater. **11**, 1372 (1999).

[7] S. F. Nelson, Y.-Y. Lin, D. J. Gundlach, and T. N. Jackson, Appl. Phys. Lett. **72**, 1854 (1998).

[8] H. Klauk, D. J. Gundlach, J. A. Nichols, and T. N. Jackson, IEEE Trans. Electron Devices **46**, 1258 (1999).

[9] O. D. Jurchescu, J. Baas, and T. T. M. Palstra, Appl. Phys. Lett. **84**, 3061 (2004).

[10] V. Podzorov, E. Menard, A. Borissov, V. Kiryukhin, J. A. Rogers, and M. E. Gershenson, Phys. Rev. Lett. **93**, 086602 (2004).

[11] A. B. Chwang and C. D. Frisbie, J. Appl. Phys. **90**, 1342 (2001).

[12] J. Liao and D. C. Martin, Macromolecules **29**, 568 (1996).

[13] T. W. Kelley, E. L. Granstrom, and C. D. Frisbie, Adv. Mater. **11**, 262 (1999).

[14] T. Maeda, T. Kobayashi, T. Nemoto, and S. Isoda, Philos. Mag. **81**, 1659 (2001).

[15] L. F. Drummy, P. K. Miska, and D. C. Martin, Mat. Res. Soc. Symp. Proc. **734**, A2.2.1 (2003).

[16] L. F. Drummy, C. Kubel, D. Lee, A. White, and D. C. Martin, Adv. Mater. **14**, 54 (2002).

[17] S. Verlaak and P. Heremans, Phys. Rev. B **75**, 115127 (2007).

[18] R. A. Street, J. E. Northrup, and A. Salleo, Phys. Rev. B **71**, 165202 (2005).

[19] P. E. J. Flewitt and R. K. Wild, *Grain Boundaries: Their Microstructure and Chemistry* (Wiley, New York, 2001).

[20] V. Kalihari, E. B. Tadmor, G. Haugstad, and C. D. Frisbie, Adv. Mater. **20**, 4033 (2008).

[21] J. E. Northrup, M. L. Tiago, and S. G. Louie, Phys. Rev. B **66**, 121404 (R) (2002).

[22] D. E. Hooks, T. Fritz, and M. D. Ward, Adv. Mater. **13**, 227 (2001).

[23] V. Kalihari, D. J. Ellison, G. Haugstad, and C. D. Frisbie, Adv. Mater. **21**, 3092 (2009).

[24] J. H. Kang, D. da Silva Filho, J. L. Bredas, and X.-Y. Zhu, Appl. Phys. Lett. **86**, 152115 (2005).

[25] J. L. Bredas, J. P. Calbert, D. da Silva Filho, and J. Cornil, Proc. Nat. Acad. Sci. **99**, 5804 (2002).

Chapter 6

Scanning Tunneling Spectroscopy of Monolayer-scale Pentacene Thin Films on Modified Si

6.1 Introduction

We have found that the molecular layers discussed in previous chapters have important electronic effects on pentacene thin films, including the development of negative differential resistance (NDR). NDR often arises from resonant tunneling, which leads to a range of effects in the current-voltage characteristics of devices and in the tunnel junction between the STM tip and the sample. Devices based on this effect, such as Esaki diodes, have applications in oscillators, switches, and logic devices [1, 2]. NDR is apparent as a decrease in the current of tunneling electrons with an increase in the applied voltage. This is exactly the opposite of a typical resistor described by Ohm's law in which small changes dI in current are proportional to small changes in voltage dV for all voltages, with $dI=(1/R)dV$. The NDR causes the resistance R to become effectively negative in a narrow range of bias voltages.

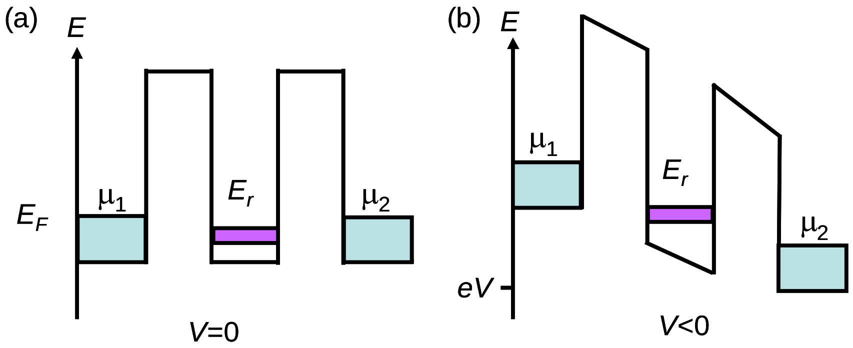

Figure 1. One-dimensional double barrier potential model (a) at no bias and (b) under bias.

One example of a structure exhibiting NDR is a one-dimensional system consisting of two potential barriers in series. Fig. 1 shows a double-barrier potential model for the conduction band of a resonant tunneling diode structure [3]. In equilibrium, as in Fig. 1(a), the electrochemical potentials of two semiconductors, μ_1 and μ_2, outside the potential well are the same as the Fermi energy, E_F. The potential well has one allowed energy E_r. This structure allows only electrons with energy E_r to transmit. An applied bias V in Fig. 1(b) lowers the energy E_r with respect to the energy of incident electrons. When the energy E_r falls below the conduction band edge, there is a sharp drop in the current. The current-voltage characteristics thus produce an NDR.

The structure shown in Fig. 1 can be created by using the tunneling gap of the STM as one of the two barriers. The second barrier can be created by a surface structure that is electronically isolated from the substrate by a potential barrier. With this approach, NDR has been reported in a wide range of previous STM studies, for example, in systems consisting of gold surfaces modified with a thiol-based molecular monolayer, in Si (111) surfaces with isolated boron atoms, and in Si (001) surfaces modified with isolated styrene molecules [4-8]. The second barrier can arise from features as small as isolated surface atoms, as for boron on Si (111) [6]. In this case, NDR occurs as a result of tunneling through localized states at atomic scale, indicating that desirable device characteristics can be obtained on the atomic scale [6]. In NDR on Si (001) surfaces modified with styrene molecules, the barrier arises from individual molecules on the Si substrate [9].

This chapter describes the NDR characteristics of pentacene thin films on modified silicon substrates. Tunneling spectra measurements were performed on the first molecular layer of pentacene on Si (001) modified with nitrobenzene and styrene using scanning tunneling spectroscopy (STS). NDR is exhibited in all of these structures as a result of the barrier formed between the pentacene thin film and the Si (001) substrate.

6.2 Setup for STS measurements

The experimental arrangement for STS measurements is shown in Fig. 2. A bias voltage, *V*, is applied between the tip and the sample. Under the bias voltage conditions appropriate for imaging, the applied voltage creates electric field located mostly between the STM tip and the molecule because the resistance of the vacuum gap between the tip and pentacene is much larger than the resistance of the pentacene film. We empirically know that this is the case because the STM can form excellent images of pentacene on nitrobenzene or styrene layers, as shown in the previous chapters. Here, the effective resistance of the vacuum gap is on the order of 1 GΩ. We show below, however, the barrier between pentacene and the substrate must also be considered under some bias voltages. Depending on the sign of the bias, electrons tunnel either from or into the tip during STS measurements.

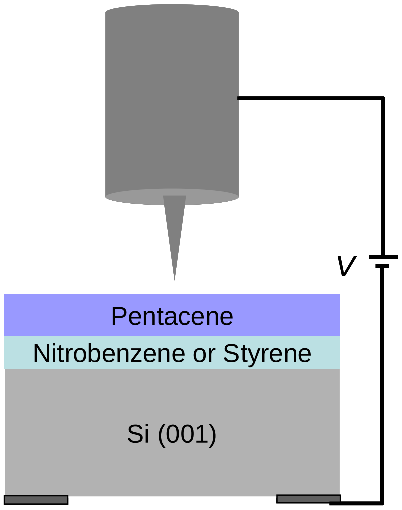

Figure 2. Schematic of STM and STS measurements performed on pentacene grown on nitrobenzene/Si (001) or on styrene/Si (001).

The spectra acquired during STS measurements are plotted as the ratio of the differential conductance, *dI/dV* to the total conductance *I/V*. Two practical concerns are critically important in acquiring STS data. The first arises from the inherent noisiness and unreliability of numerical differentiation. It is thus experimentally more accurate to obtain *dI/dV* directly using a lock-in amplifier rather than by differentiating the *I-V* measurements. A second important concern results from the difficulty in assigning the zero value of voltage accurately. This effect leads to a condition in which the current is not precisely zero at the point where the applied voltage is thought to be zero. Dividing the current by the voltage to obtain *I/V* at this zero-voltage point then leads to a divergence of *I/V* and (*dI*/*dV*)/(*I*/*V*) near zero bias. To eliminate this divergence, *I/V* was replaced by $\sqrt{(I/V)^2 + c^2}$, where *c* is a small scalar constant with a value of 0.02 nA/V [10]. In our experiment, the voltages in all the plots are expressed in terms of the sample bias.

Our procedure for acquiring STS measurements was designed to minimize the effects arising from possible drift and instability of the tunneling microscope. Acquiring tunneling spectra involves disabling the tip-height feedback loop, thus raising the risk that the tip-sample distance could change significantly during the measurement. If the tip-sample distance were to change, drift and instability would distort the spectrum. We have acquired spectra with sufficiently low noise by averaging multiple spectra. Each spectrum was acquired with a short period of time in which the feedback is disabled. An example of this approach is shown in Fig. 3, which shows a series of 20 *I-V*, *dI*/*dV*, and their ratio (*dI*/*dV*)/(*I*/*V*). The tunneling spectra in Fig. 3 exhibit only the conventional response, in which the differential resistance is positive at all bias voltages. In other spectra, those exhibiting NDR, the negative slope in the *I-V* curve produces a minimum below zero in the plot of (*dI/dV*)/(*I/V*) as a function of *V*.

We found that tunneling spectra were reproducibly obtained under conditions in which individual pentacene molecules could be resolved in STM images. STM measurements were thus carried out on all samples before all of the STS measurements. We limited the voltage range over which the spectra were acquired in order to keep the magnitude of the current below the values at which there was irreversible damage to the pentacene layer. The practical limit for the tunneling current was 1.5 nA.

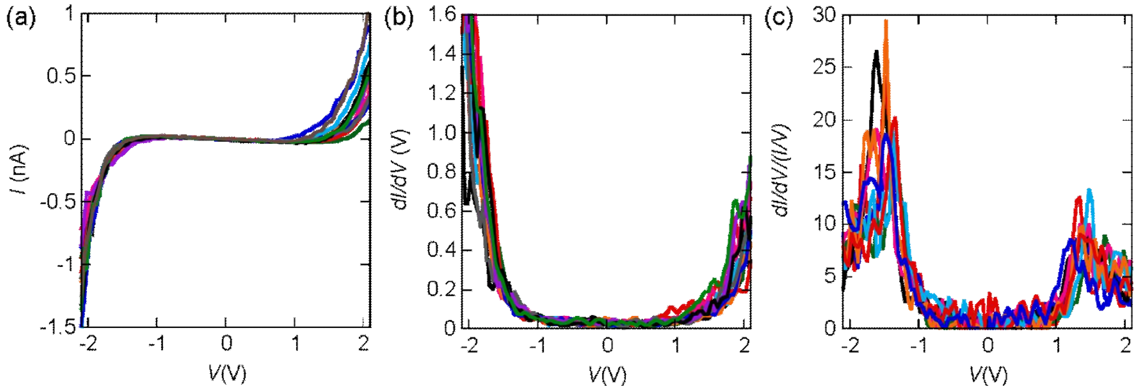

Figure 3. Repeated spectra of (a) current as a function of voltage, (b) differential conductance, *dI/dV*, as a function of voltage, and (c) tunneling spectra given by (*dI/dV*)/(*I/V*) as a function of voltage. The sample consisted of a nitrobenzene-modified Si (001) surface.

6.3 Molecular interlayers as interface linkages

We used nitrobenzene and styrene molecules to isolate the pentacene molecules from the Si (001) substrate. The two molecules have similar structures consisting of one aromatic ring. Both attach to Si (001) by covalent bonding as described in Chapter 3. We collaborated with Dr. Guowen Peng in the research group of Professor Manos Mavrikakis to study the electronic structure of interfaces incorporating these molecules using density functional theory (DFT) calculations. Our STS measurements were performed on nitrobenzene/Si (001) and styrene/Si (001) to examine the similarities and differences between two structures, including their NDR properties.

6.3.1 Dipole moment of organic layers

An important consideration with respect to the formation of the substrate-pentacene tunnel junction and the energy levels of the pentacene molecule is whether the interface between pentacene and Si (001) incorporates a large dipole moment. We suspected that the difference between nitrobenzene and styrene would be important in this case because the gas-phase dipole moment of nitrobenzene is much larger than the dipole moment of styrene. We hypothesized that the dipole moment of nitrobenzene/Si (001) would thus be different from that of styrene/Si (001). Dr. Guowen Peng used DFT to determine the dipole moments of nitrobenzene and styrene in the gas phase and in the configuration in which they were attached to a Si (001) dimer. As described in detail below, we found surprisingly little difference between the dipole moments of the molecules on Si (001), suggesting that their roles in establishing the pentacene-silicon tunneling barrier would be similar.

6.3.1.1 Dipole moment of nitrobenzene on Si (001)

In the gas phase, nitrobenzene has a large dipole moment arising from the asymmetry induced by the NO_2 group. The dipole moment of gas-phase nitrobenzene is 4.5 D, where 1 D=1 Debye=3.34×10^{-28} C·cm. It was previously thought that this large dipole moment was also found in the configuration in which nitrobenzene is attached to the silicon surfaces. Calculations of the structure of nitrobenzene on Si (111), for example, have found a dipole moment of 4.5 Debye per unit cell [11].

The results of the DFT calculations of the structure and the dipole moment of nitrobenzene on Si (001) are shown in Figure 4. The structures of three different bonding geometries are shown because our previous structural study of nitrobenzene on Si (001) showed that there was not one unique local configuration. The direction and the magnitude of the dipole moment for each bonding configuration are also indicated in the figure. In Fig. 4(b), oxygen atoms in the nitro group of the nitrobenzene molecule bond to Si atoms of the dimer. In Fig. 4(c), one of the oxygen atoms moves to the backbond of the Si (001) dimer to form a Si-O-Si structure, reducing the energy. The configuration in Fig. 4(d) is similar, with the exception that two oxygen atoms move to the backbonds of the Si (001) dimer.

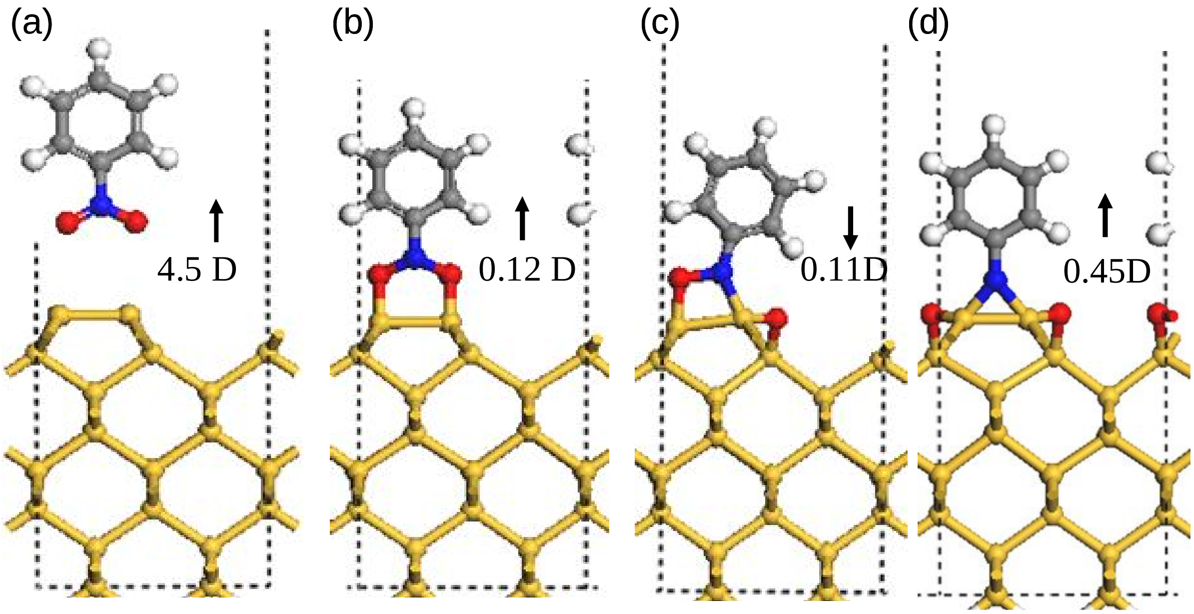

Figure 4. (a) Isolated nitrobenzene molecule, drawn above a Si (001) surface with a 2×1 reconstruction. (b), (c), and (d) Nitrobenzene attached to Si (001) dimers in three different bonding geometries. The arrows indicate the direction of the dipole moment.

The surprising result of the calculations shown in Fig. 4 is that the dipole moments are quite small in all of the configurations in which nitrobenzene bonds to the Si (001) surface. The total dipole moments for the three configurations shown in Fig. 4 range from 0.11 to 0.45 D, far lower than the gas-phase value of 4.5 D. The lowest energy structure in Fig. 4(d) has the largest of these dipole moments, 0.45 D, but this is still much smaller than the gas-phase dipole moment.

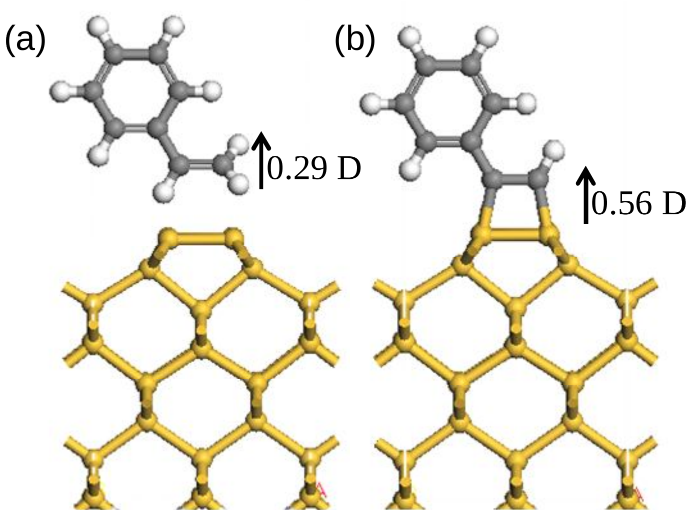

Figure 5. (a) Isolated styrene molecule. (b) Styrene attached to a Si (001) dimer. The arrows indicate the direction of the dipole moment.

6.3.1.2. Dipole moment of styrene on Si (001)

The results of the DFT calculations for styrene are shown in Fig. 5. An isolated styrene molecule has a dipole moment of 0.29 D, pointing towards the benzene ring from the vinyl group. This dipole moment is a factor of approximately 15 smaller than the dipole moment of the gas-phase nitrobenzene molecule. The surprising result of the DFT calculation is that the dipole moment of styrene attached to a Si (001) dimer is higher than the isolated molecule, 0.56 D. The styrene dipole moment is actually thus slightly higher than the dipole moment of nitrobenzene on Si (001). In absolute terms, as we show below, the dipole moments are highly similar and will produce small shifts in the tunneling spectra.

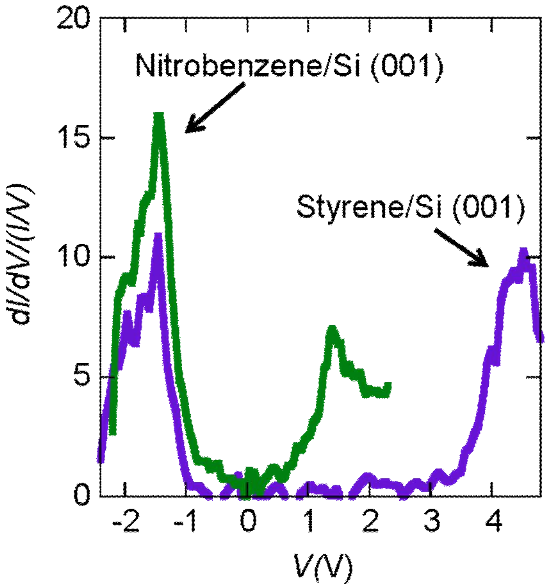

Figure 6. Tunneling spectra of nitrobenzene on Si (001) and styrene on Si (001).

6.3.2. Tunneling spectra of nitrobenzene and styrene

In order to establish the usefulness of nitrobenzene and styrene in producing a barrier between pentacene and Si, we used STS to examine Si (001) surfaces modified with these molecules. We expected that the tunneling spectra of both molecules would reveal an energy gap corresponding to the gap between the energies associated with the filled and empty states of the pentacene molecular orbitals. The results of the STS measurements on nitrobenzene and styrene-terminated surfaces are shown in Fig. 6. As we expected, the tunneling spectra reveal two pronounced peaks for both surfaces. The samples were stabilized under very similar tunneling conditions prior to acquiring the spectra. The current and the voltage before the feedback was disabled were -1.8 V and 300 pA for nitrobenzene on Si (001) and -1.9 V and 300 pA for styrene on Si (001).

The nitrobenzene/Si (001) tunneling spectrum exhibits strong maxima centered at -1.4 V and 1.4 V. These peaks correspond to conduction to the HOMO level for negative bias and to the LUMO level of nitrobenzene for positive bias. The magnitude of the normalized differential conductance under negative bias is larger than that of positive bias, which indicates that the filled states have better overlap with the electronic levels of the tip.

The tunneling spectra of styrene on Si (001) show the HOMO and LUMO peaks at -1.4 V and 4.5 V, respectively. Styrene on Si (001) exhibits a tunneling gap of 5.9 V. This gap is far larger than 2.8 V observed for nitrobenzene on Si (001). The relative magnitude of the two peaks of the styrene/Si (001) spectrum is similar. The tunneling gap observed in the STS measurements with styrene on Si (001) is wider than the gap reported in the literature for styrene on n^+-Si (001), 2.5 V [7].

6.4 Negative differential resistance through pentacene on modified Si

Adding the pentacene layer to the modified silicon surface produces a dramatic change in the tunneling spectra. We show in this section that pentacene layers on both surfaces have qualitatively similar tunneling spectra, in both cases producing NDR. The differences between the spectra can be explained in terms of the molecular barriers between pentacene and Si (001). In the first series of experiments, we used STS to acquire tunneling spectra for a one-molecular-layer thick pentacene film on nitrobenzene-modified Si (001). An STM image of pentacene islands in this layer at a very large lateral scale is shown in Fig. 7(a).

STS measurements for pentacene on nitrobenzene-modified Si (001) were carried out in a small part of the STM image in Fig. 7(a). *I-V* and (*dI/dV*)/(*I/V*) as a function of voltage are shown in Fig. 7(b) and 7(c), respectively. The tunneling conditions before the STS measurements were -3.0 V and 300 pA. A series of tunneling spectra were acquired at -2.5 V and 300 pA in the same area.

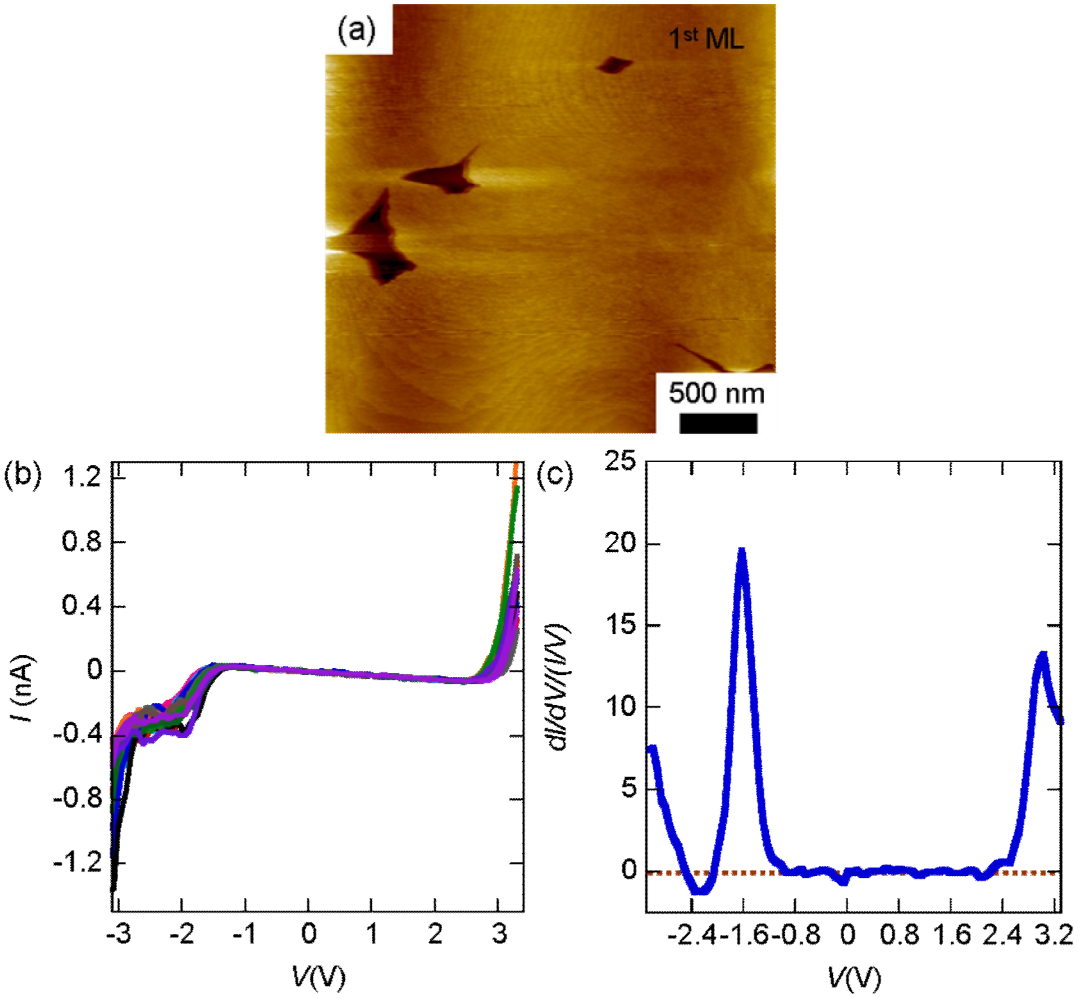

Figure 7. (a) STM image of pentacene on nitrobenzene on Si (001). (b) *I* as a function of *V* and (c) *dI/dV/(I/V)* as a function of *V* for pentacene on nitrobenzene/Si (001).

The two distinct peaks that reflect the HOMO and LUMO levels of pentacene in Fig. 7(c) are centered at -1.6 V and 3.0 V. The tunneling spectrum exhibits a sharp HOMO peak, which is narrower than that of nitrobenzene on Si (001). The presence of a sharp peak indicates that the tunneling spectra of pentacene on nitrobenzene/Si (001) and nitrobenzene on Si (001) are distinguished from each other.

The tunneling gap of 4.6 V apparent in Fig. 7(c) is different from the HOMO-LUMO gap of pentacene reported in the literature. The gap of 4.6 V is much wider than 1.9 V derived from x-ray photoelectron spectroscopy (XPS) and ultraviolet photoemission spectroscopy (UPS) measurements for pentacene on GaN and 2.4 V determined using STM for pentacene on Cu (119) [12, 13]. Pentacene deposited on Ag or Au surfaces exhibits a tunneling gap of 2.2 V, which coincides with the HOMO-LUMO gap of pentacene molecules [14, 15]. In order to explain the tunneling spectrum observed in Fig. 7, one must consider the overall structure of the system, including the second tunneling barrier at the pentacene-silicon interface.

The wide apparent tunneling gap in the STS spectrum for pentacene on nitrobenzene/Si (001) arises from the barrier between pentacene and Si induced by the nitrobenzene layer. The situation is similar to electron transport experiments in molecular solid, where the experimental tunneling gap is different from the HOMO-LUMO gap of the neutral molecule [16]. A more quantitative description is given in section 6.5.

A second set of spectroscopic measurements was conducted to obtain tunneling spectra for pentacene on styrene-modified Si (001). For this experiment, a pentacene thin film was grown on styrene-modified Si to a total thickness of 1.57 molecular layers at the deposition rate of 0.16 molecular layers per minute. Under these conditions, islands in the second molecular layer formed and covered a large fraction of the surface, as shown in the STM image in Fig. 8(a).

In order to compare the spectra from pentacene on styrene-modified Si with those from pentacene on nitrobenzene-modified Si, we performed the STS measurements using only the first molecular layer of pentacene.

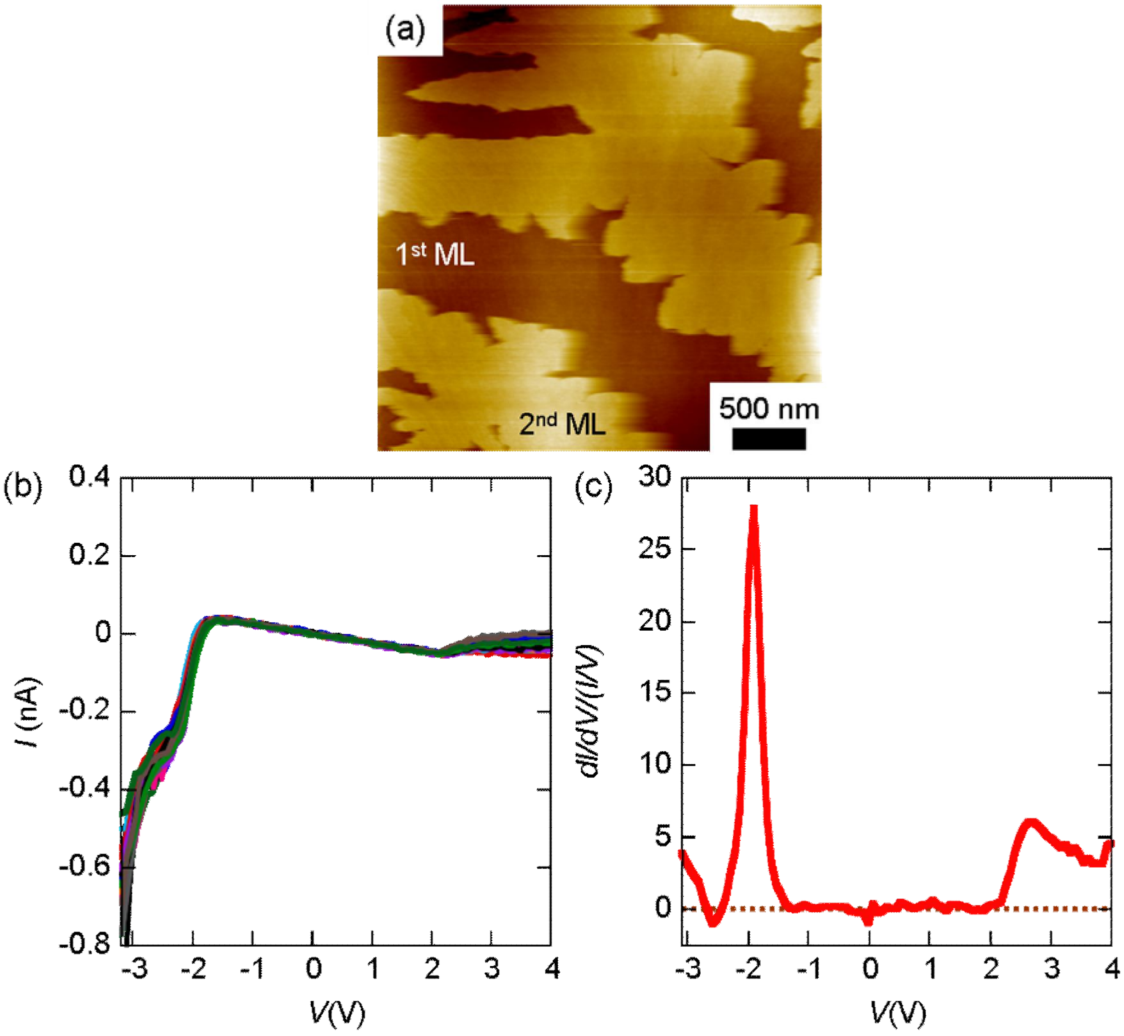

Figure 8. (a) STM image of pentacene on styrene-modified Si (001). (b) *I-V* curves and (c) tunneling spectrum of pentacene acquired from the first molecular layer of pentacene molecules.

Tunneling spectra acquired from pentacene on styrene-modified Si (001) are shown in Fig. 8(b) and Fig. 8(c). The tunneling conditions before the feedback was disabled to acquire the

STM image were -3.0 V and 300 pA. The tunneling spectra were acquired at -1.8 V and 350 pA. The peak in the spectrum at positive bias has a smaller magnitude than the peak at negative bias. The negative-bias HOMO peak exhibits a sharp narrow feature similar to that of pentacene on nitrobenzene/Si (001). The LUMO peak, observed at positive bias, however, is broader in comparison to that of pentacene on nitrobenzene-modified Si (001), indicating a wide distribution of density of states.

Comparing the results from the two experimental configurations provides some insight into the effects arising from the molecular layer at the interface. First, the apparent tunneling gap is the same for both pentacene on nitrobenzene-modified Si (001) and pentacene on styrene-modified Si (001). The bias voltages at which the maxima associated with the HOMO and LUMO are, however, different by 0.3 V. In effect, the two tunneling spectra for pentacene on nitrobenzene/Si (001) and on styrene/Si (001) are shifted in voltage with respect to each other.

The spectra for pentacene on both molecular layers exhibit negative differential resistance (NDR). Pentacene layers both on nitrobenzene/Si (001) and on styrene/Si (001) show the normalized differential conductance minimum below zero in the tunneling spectra at negative bias.

6.5 Tunneling conditions for negative differential resistance

The tunneling conditions leading to NDR can be explained using the model developed by Datta *et al.*, shown in Fig. 9 [17]. The electrostatic potential profile describes how the electrochemical potential is assumed to vary in the gap between the tip and the sample. The electrochemical potentials of the Si substrate and the STM tip are represented as μ_1 and μ_2, respectively. The substrate and the tip are electron reservoirs under applied bias. The bias voltage is equivalent to the difference between the electrochemical potentials of the substrate and the tip:

$$eV = \mu_1 - \mu_2 . \tag{1}$$

The electrochemical potential difference of two metal electrodes in terms of the electrostatic potential and the chemical potential under applied bias is given by

$$eV = e\Delta\mu = e\Delta\varphi + \Delta\overline{\mu} . \tag{2}$$

where $\Delta\mu$, $\Delta\varphi$, and $\Delta\overline{\mu}$ are the difference between the electrochemical potentials, the electrostatic potentials and the chemical potentials of two electrodes, respectively [18].

The change in the electrostatic potential depends on the number of charges introduced to the system by applying an external voltage. The electrostatic potential $\varphi(r)$, which spatially varies as a function of a distance r, is determined by the Poisson equation:

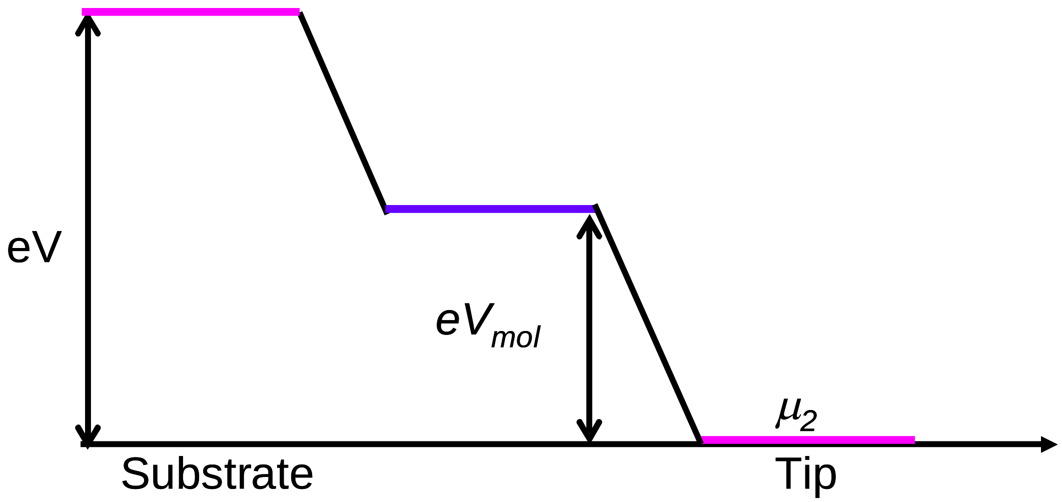

Figure 9. Electrostatic potential profile from the Si substrate to the STM tip under positive sample bias.

$$\vec{\nabla} \cdot (\varepsilon \vec{\nabla} \delta\varphi) = \delta\rho , \tag{3}$$

where $\delta\rho$ is the change in the charge density and ε is the dielectric constant [17]. The boundary condition for the Poisson equation is that the difference in the electrostatic potential of the substrate and the tip follows the change in the electrochemical potential.

The values of μ_1 and μ_2 in the model can be calculated using

$$\mu_1 = -\eta eV , \tag{4}$$

$$\mu_2 = (1-\eta)eV , \tag{5}$$

where the factor η describes how the electrostatic potential difference is divided between the substrate and the tip [17]. In the electrostatic potential profile in Fig. 9, η is given by

$$\eta = V_{mol} / V , \tag{6}$$

where V_{mol} is the average electrostatic potential in a molecule and V is the applied bias voltage. $\mathrm{V_{mol}}$ is half the applied voltage for η of 0.5. Neither μ_1 nor μ_2 remains fixed with respect to the molecule. The threshold for conduction for negative sample bias is given by

$$-eV = \frac{-E_H}{1-\eta} . \tag{7}$$

where E_H represents the energy for the HOMO level of the molecule.

The *I*-*V* plots of pentacene on nitrobenzene/Si (001) and on styrene/Si (001) show asymmetric characteristics in which the magnitudes of the tunneling current for the positive and the negative bias voltages are different. Therefore, the value of η in these systems is different from 0.5.

In order to describe the NDR effect, we will have an important simplifying assumption. Although the experiments have two organic layers (e.g. pentacene and nitrobenzene) between the

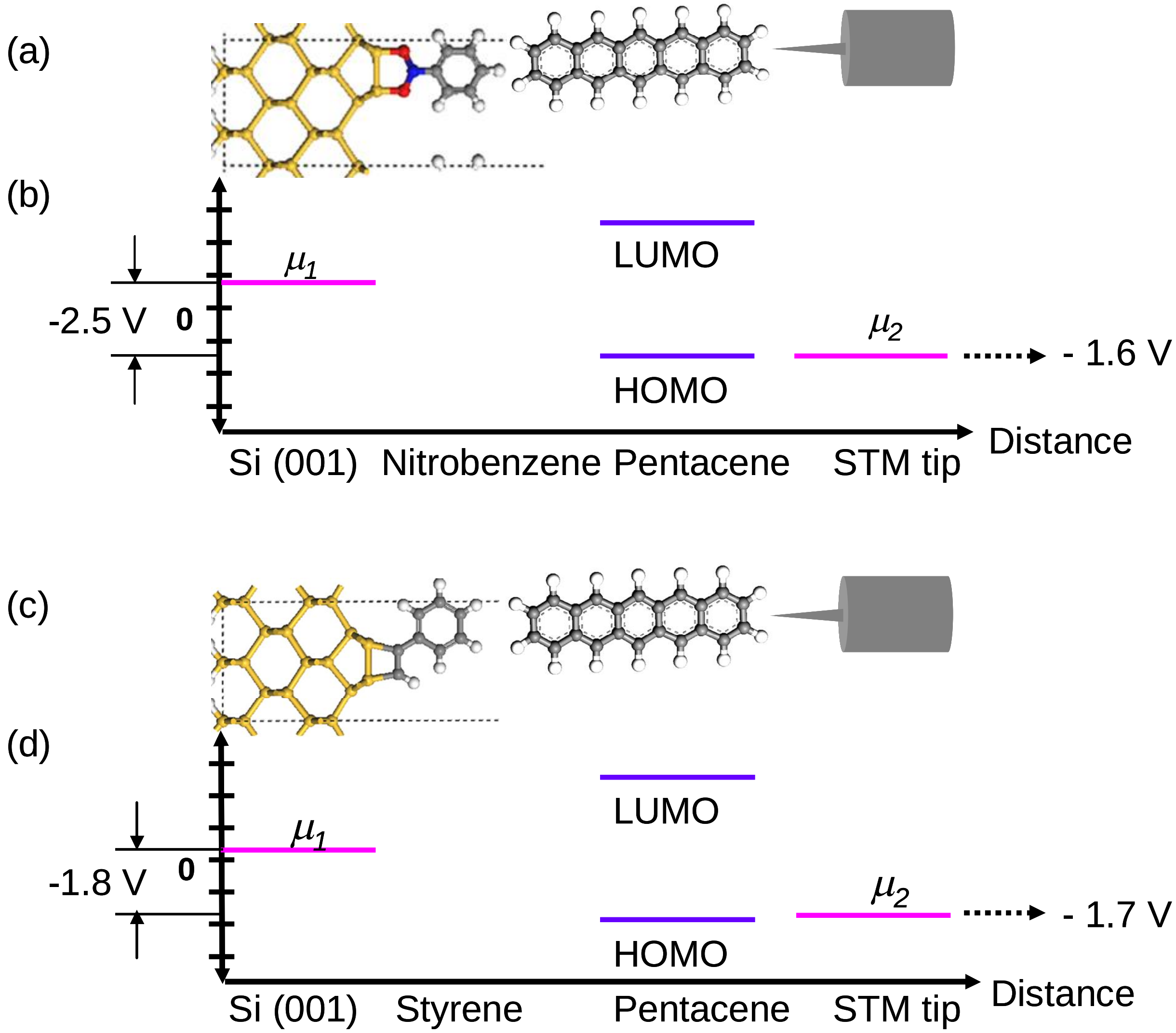

Figure 10. (a) Schematic of Si/nitrobenzene/pentacene interface. (b) Electrostatic potential profile from the Si substrate to the STM tip for pentacene on nitrobenzene/Si (001). (c) Schematic of Si/styrene/pentacene interface. (d) Electrostatic potential profile from the Si substrate to the STM tip for pentacene on styrene/Si (001) under negative bias.

tip and the Si substrate, we will consider states arising from the pentacene layer only. This appears to be a valid assumption because information on the energy levels of nitrobenzene on Si (001) cannot be obtained after the deposition of pentacene.

For pentacene on nitrobenzene-modified Si (001), the HOMO and LUMO peaks are centered at the voltages of -1.6 V and 3.0 V, respectively, for the bias voltage of -2.5 V. The value of η calculated using Eq. (7) is 0.36. Plugging the value of η into Eq. (4) and Eq. (5), we obtain

$$\mu_1 = -0.36 \times (-2.5\ \mathrm{V}) = 0.9\ \mathrm{V} \tag{8}$$

$$\mu_2 = (1-0.36) \times (-2.5\ \mathrm{V}) = -1.6\ \mathrm{V}. \tag{9}$$

At a negative sample bias of -2.5 V, the electrochemical potential for the tip μ_2 aligns with the HOMO level in the tunneling spectrum of pentacene on nitrobenzene/Si (001) as illustrated in Fig. 10(b). The alignment of the HOMO level with the electrochemical potential of the tip is an important condition for resonant tunneling that leads to NDR. At a sample bias slightly higher than -2.5 V, for example at -3.0 V, NDR was not observed because applying -3 V lowered the tip potential μ_2 below the HOMO level.

The value of η calculated for pentacene on styrene/Si (001) is 0.06, smaller than that of pentacene on nitrobenzene-modified Si (001). With this value, we get:

$$\mu_1 = -0.06 \times (-1.8\ \mathrm{V}) \approx 0.2\ \mathrm{V}, \tag{10}$$

$$\mu_2 = (1-0.06) \times (-1.8\ \mathrm{V}) \approx -1.7\ \mathrm{V}. \tag{11}$$

In this case, μ_2 is slightly off the HOMO level of pentacene by 0.2 V as depicted in Fig. 10(d). Although the HOMO level is not exactly aligned with the electrochemical potential of the tip, NDR is still observed. The electrochemical potential of the tip μ_2 is, however, close to being off resonance and thus the magnitude of the normalized differential conductance below zero in the tunneling spectra of pentacene on styrene/Si (001) is smaller that of pentacene on nitrobenzene/Si (001).

6.6 Conclusion

Negative differential resistance appears in the tunneling spectra of both pentacene on nitrobenzene/Si (001) and on styrene/Si (001) for negative sample bias. NDR was not observed for positive sample bias because of the presence of the broad LUMO peaks in the tunneling spectra for pentacene on nitrobenzene/Si (001) and on styrene/Si (001). Previous studies have reported that NDR develops when tunneling occurs through sufficiently narrow features of the density of states of the sample [8]. Our results show that NDR can be produced by using the tunneling gap of STM and the molecular tunnel barrier between pentacene and the Si (001) substrate.

6.7 References

[1] L. Esaki, Phys. Rev. **109**, 603 (1958).

[2] R. H. Mathews, J. P. Sage, S. D. Calawa, C.-L. Chenar, L. J. Mahoney, P. A. Maki, and K. M. Molvar, Proc. IEEE **87**, 596 (1999).

[3] S. Datta, *Electronic Transport in Mesoscopic Systems* (Cambridge University Press, Cambridge, 1995).

[4] Y. Xue, S. Datta, S. Hong, R. Reifenberger, J. I. Henderson, and C. P. Kubiak, Phys. Rev. B **59**, R7852 (1999).

[5] I.-W. Lyo and Ph. Avouris, Science **245**, 1369 (1989).

[6] P. Bedrossian, D. M. Chen, K. Mortensen, and J. A. Golovchenko, Nature **342**, 258 (1989).

[7] N. P. Guisinger, M. E. Greene, R. Basu, A. S. Baluch, and M. C. Hersam, Nano Lett. **4**, 55 (2004).

[8] Ph. Avouris, I.-W. Lyo, F. Bozso, and E. Kaxiras, J. Vac. Sci. Technol. A **8**, 3405 (1990).

[9] N. P. Guisinger, R. Basu, M. E. Greene, A. S. Baluch, and M. C. Hersam, Nanotechnology **15**, S452 (2004).

[10] M. Prietsch, A. Samsavar, and R. Ludeke, Phys. Rev. B **43**, 11850 (1991).

[11] A. Natan, Y. Zidon, Y. Shapira, and L. Kronik, Phys. Rev. B **73**, 193310 (2006).

[12] C. Baldacchini, C. Mariani, M. G. Betti, L. Gavioli, M. Fanetti, and M. Sancrotti, Appl. Phys. Lett. **89**, 152119 (2006).

[13] J. Uhlrich, M. Garcia, S. Wolter, A. S. Brown, and T. F. Kuech, J. Cryst. Growth **300**, 204 (2007).

[14] V. Arima, F. D. Sala, F. Matino, R. I. Blyth, G. Barbarella, M. Melucci, R. Cingola, and R. Rinaldi, Phys. Rev. B **72**, 085425 (2005).

[15] Ph. Guaino, A. A. Cafolla, O. McDonald, D. Carty, G. Sheerin, and G. Hughes, J. Phys.: Condens. Matter **15**, S2693 (2003).

[16] M. Pope and C. E. Swenberg, *Electronic Processes in Organic Crystals and Polymers* (Oxford University Press, Oxford, 1999).

[17] S. Datta, W. Tian, S. Hong, R. Reifenberger, J. I. Henderson, and C. P. Kubiak, Phys. Rev. Lett. **79**, 2530 (1997).

[18] M. Di Ventra, *Electrical Transport in Nanoscale Systems* (Cambridge University Press, Cambridge, 2008).